

ISSP

**ACTIVITY
REPORT
OF
SYNCHROTRON
RADIATION
LABORATORY**

2020

© 2020 *The Institute for Solid State Physics, The University of Tokyo*

Activity Report 2020

TABLE OF CONTENTS

<i>pp</i>		
5		Preface : Yoshihisa Harada
6	1	Status of Beamline BL07LSU at the SPring-8
9	2	Status of spin-and angle-resolved photoelectron spectroscopy with laser light at LASOR
11	3	Workshop & Meetings
12	4	Seminar
	5	Activities

Synchrotron Radiation Experiments (SPring-8)

13	1)	ANALYSIS OF ELECTRONIC STATES IN WATER MOLECULES CONFINED IN BIOCOMPATIBLE POLYMER BRUSH DERIVATIVES USING SOFT X-RAY EMISSION SPECTROSCOPY Keishi Akada, Shin-nosuke Nishimura, Kosuke Yamazoe, Daiki Murakami, Jun Miyawaki, Masaru Tanaka, Yoshihisa Harada
15	2)	RESONANT SOFT X-RAY EMISSION SPECTROSCOPY OF A HIGH-VOLTAGE CATHODE MATERIAL Daisuke Asakura, Eiji Hosono, Akihiro Ohira, Takaaki Sakai, Kosuke Yamazoe, Naoya Kurahashi, Ralph J. Ugalino, Yoshihisa Harada
17	3)	ELECTRONIC STATE OF BULK SINGLE CRYSTAL Co₂FeSi HEUSLER ALLOY PROBED BY RESONANT INELASTIC SOFT X-RAY SCATTERING (SX-RIXS) IN MAGNETIC FIELD Rie Y. Umetsu, Hidenori Fujiwara, Jun Miyawaki, Kohei Nishimoto, Rika Kasahara, Yuto Arinaga, Akira Sekiyama, Yoshihisa Harada, Shigemasa Suga
19	4)	NONPOLARIZING OXYGEN-REDOX CAPACITY WITHOUT O-O DIMERIZATION IN Na₂Mn₃O₇ Akihisa Tsuchimoto, Masashi Okubo
21	5)	OPERADO ANALYSIS OF ELECTRONIC STRUCTURE OF CATALYTIC ACTIVE SITES IN REDOX FLOW BATTERIES Akihiro Ohiraa, Eiji Hosonoa, Daisuke Asakuraa, Takaaki Sakaia, Kosuke Yamazoe, Naoya Kurahashi, Yoshihisa Harada
23	6)	SOFT X-RAY CORE-LEVEL SPECTROSCOPY ON SURFACES IN MIXED CONDUCTIVE OXIDES DURING OXYGEN PERMEATION Isao Kagomiya, Tomohiro Hirano, Yutaro Yagi, Susumu Yamamoto, Iwao Matsuda
25	7)	AMBIENT PRESSURE X-RAY PHOTOELECTRON SPECTROSCOPY ON SURFACES IN MIXED CONDUCTIVE OXIDES AT ELEVATED TEMPERATURES Isao Kagomiya, Tomohiro Hirano, Takayuki Kato, Susumu Yamamoto, Iwao Matsuda
27	8)	ANALYSIS OF INTERACTIONS BETWEEN POLYAMIDE AND WATER MOLECULES IN REVERSE OSMOSIS MEMBRANES BY XAS, XES AND RIXS Jumpei Yahiro, Koichi Ozaki, Masaru Nakada, Masahiro Kunisu, Harutoki Shimura, Shinya Mitsui, Naoya Kurahashi, Kosuke Yamazoe, Yoshihisa Harada
29	9)	STUDY ON HYDROGEN BOND STRUCTURE OF WATER MOLECULES IN POLYMER ELECTROLYTE

- 31 10) **METHANE CONVERSION REACTION ON PT AND PD MODEL CATALYSTS STUDIED BY OPERANDO AMBIENT-PRESSURE XPS**
Takanori Koitaya
- 33 11) **DIRECT OBSERVATION OF METHANE OXIDATIVE COUPLING REACTION ON PALLADIUM BASED ALLOYS BY AMBIENT-PRESSURE XPS**
Takanori Koitaya
- 35 12) **BROAD SPECTRAL FEATURE DUE TO P-D HYBRIDIZATION IN P-TYPE FERROMAGNETIC SEMICONDUCTOR (IN,MN) AS**
Masaki Kobayashi¹, Kohsei Araki, Takahito Takeda, Le Duc Anh, Atsushi Fujimori³, Jun Miyawaki, Yoshihisa Harada, Shinobu Ohya, Masaaki Tanaka
- 37 13) **LI INSERTION MECHANISM OF OCTAHEDRAL LI₄TI₅O₁₂ SINGLE CRYSTALLINE PARTICLE BY MAPPING MEASUREMENT OF 3DNANOESCA**
Wenxiong Zhang, Eiji Hosono, Daisuke Asakura, Naoka Nagamura, Masaharu Oshima, Yoshihisa Harada
- 39 14) **AMBIENT-PRESSURE X-RAY PHOTOELECTRON SPECTROSCOPY STUDIES OF CO₂ HYDROGENATION ON PD-BASED ALLOY**
Jiayi Tang
- 41 15) **INVESTIGATION OF LPSO-STRUCTURE FORMATION MECHANISM BY SMALL ANGLE INELASTIC X-RAY SCATTERING**
Kakeru Ninomiya, Yoshihisa Harada, Maiko Nishibori
- 43 16) **EVALUATION OF INTERFACIAL WATER ON ARTIFICIAL POLYMERS BY SOFT X-RAY EMISSION SPECTROSCOPY**
Shin-nosuke Nishimura, Daiki Murakami, Kosuke Yamazoe, Naoya Kurahashi, Tomoya Ueda, Yoshihisa Harada, Masaru Tanaka
- 45 17) **MAPPING ANALYSIS OF ACTIVE MATERIALS FOR LITHIUM ION BATTERIES BY 3D NANOESCA**
Eiji Hosono, Wenxiong Zhang, Daisuke Asakura, Naoka Nagamura, Masaharu Oshima, Yoshihisa Harada
- 47 18) **STRUCTURE-SELECTIVE ELECTRONIC STRUCTURE ANALYSIS BY RESONANT INELASTIC SOFT X-RAY DIFFRACTION**
Jun Miyawaki, Takehiro Yachi, Sachiko Maki, Kiyoshi Kanie, Yoshihisa Harada
- 49 19) **OBSERVATION OF DEHYDRATION PROCESS OF THERMOSENSITIVE POLYMERS BY SOFT X-RAY ABSORPTION AND EMISSION SPECTROSCOPY**
Kosuke Yamazoe, Ralph John Ugalino, Jun Miyawaki, Yoshihisa Harada
- 51 20) **UPGRAD OF AMBIENT PRESSURE X-RAY PHOTOELECTRON SPECTROSCOPY SYSTEM AT SPRING-8 BL07LSU**
Susumu Yamamoto, Takanori Koitaya, Iwao Matsuda, Jun Yoshinobu

Experiments at E-Labo

- 53 1) **ELECTRONIC STRUCTURE OF VAN DER WAALS MAGNETIC SEMIMETAL GDGAL**
Kohei Yamagami, Ryotaro Okuma, Yoshinari Okada

54	2)	ENHANCEMENT OF RASHBA SPLITTING IN SNPC/AU(111) Kaname Kanai
56	3)	SARPES STUDY OF A NEW WEYL SEMIMETAL OF THE CDW COMPOUNDS Chun Lin, Kenta Kuroda, Ryo Noguchi, Kaishu Kawaguchi, Ayumi Harasawa, Shik Shin, Masanobu Miyata, Koyano Mikio, Takeshi Kondo
58	4)	OBSERVATION AND CONTROL OF THE WEAK TOPOLOGICAL INSULATOR STATE IN ZRTE5 Peng Zhang, Ryo Noguchi, Kenta Kuroda, Chun Lin, Kaishu Kawaguchi, Koichiro Yaji, Ayumi Harasawa, Mikko Lippmaa, Simin Nie, Hongming Weng, V. Kandyba, A. Giampietri, A. Barinov, Qiang Li, G. D. Gu, Shik Shin, Takeshi Kondo
60	5)	ANGLE-RESOLVED PHOTOEMISSION SPECTROSCOPY OF GALLIUM SINGLE CRYSTAL SURFACE Koichiro Yaji, Kenta Kuroda, Fumio Komori
61	6)	STUDY ON THE SPIN TEXTURE OF THE TOPOLOGICAL STATES IN QUASI-ONE-DIMENSIONAL MATERIAL Deyang Wang, Mao Ye, Kenta Kuroda, Koichiro Yaji, Ayumi Harasawa, Takeshi Kondo
63	6	Staff
64	7	Publication List

Preface

The Synchrotron Radiation Laboratory (SRL) of the Institute for Solid State Physics (ISSP) has been cooperating with the Synchrotron Radiation Research Organization of the University of Tokyo to operate the BL07LSU soft X-ray beamline and its experimental end stations at SPring-8 since 2006. The beamline has a 27-m-long polarization-controlled undulator and monochromator covering the photon energy range from 250 eV to 2 keV with an average photon flux of 10^{12} photons/sec. In 2009, SRL opened the beamline to the public as one of the core facilities for the development of unique spectroscopy and advanced materials science in the soft X-ray region. Since then, the SRL staff members have been playing an essential role in promoting joint research by domestic and international users. The three end stations, i.e. ambient pressure X-ray photoemission spectroscopy, three dimensional nanoESCA, and the high-resolution soft X-ray emission spectroscopy stations, have excellent high pressure (~ 20 mbar), spatial resolution (~ 70 nm), and energy resolution ($E/\Delta E \approx 10,000$), respectively. In FY2020, the COVID-19 problem significantly restricted the user access, which to some extent affected our research activities. Nevertheless, we continued our activities and developments without major delays by conducting analyses that contribute to the social community, e.g. development of medical devices that can be used to save coronavirus infectants.

The Japanese government has decided to construct a next-generation synchrotron radiation facility dedicated to the soft X-ray and tender X-ray regions in Sendai in 2018. SRL has decided to make a significant commitment to the new facility. SRL will terminate the ISSP joint research program at SPring-8 in the first half of 2022, and transfer many of the instrumentations to the new facility. In addition, SRL is planning to develop novel high-performance focusing mirrors to enhance imaging technology that can most effectively make use of the new facility.

In addition to the cutting-edge activities using synchrotron radiation, SRL joined the Laser and Synchrotron Research (LASOR) Center as a member in 2012. Since then, SRL has promoted the scientific use of laser-based high-harmonic generation in the vacuum ultraviolet and soft X-ray regions at the Kashiwa campus. Since 2015, SRL has opened the joint use of the high-resolution laser spin- and angle-resolved photoelectron spectroscopy (SARPES) system that is designed to provide high-energy (1.7 meV) and -angular resolutions with high-efficiency spin detectors for various types of solids, such as spin-orbit coupled materials and ferromagnetic materials.

Our goal is to provide users with a platform that uses both synchrotron radiation and high-harmonic generation by lasers by strong collaboration with other LASOR group members.

June 30, 2020

Yoshihisa Harada

Director of SRL-ISSP

1. Status of Beamline BL07LSU at SPring-8

The University-of-Tokyo high-brilliance synchrotron soft X-ray outstation beamline BL07LSU at SPring-8 has been maintained by the permanent staff members with adjuncts for user operations. The scientific aim of the beamline is to promote advanced spectroscopy for solid state and soft (including bio-) materials. There are four regular endstations for time-resolved soft X-ray spectroscopy (TR-SX spectroscopy), ambient pressure X-ray photoelectron spectroscopy, 3D-scanning photoelectron microscope (3D nano-ESCA) and high-resolution soft X-ray emission spectroscopy (HORNET) that are open for users. There is also a free port station for users who bring their own experimental apparatus.

The beamline BL07LSU is equipped with a segmented cross-type undulator. Circularly and linearly polarized soft X-rays can be used in user experiments at full energy range (250 – 2000 eV). By using phase shifters between the neighboring undulator segments, polarization of the soft X-ray beam is regulated continuously and the switching frequency can be tuned up to 13 Hz. At the end-stations, various scientific experiments were carried out by both the laboratory staffs and users with applications of G-type (general), S-type (special), and P-type (priority). A user group of the S-type spends the long-term beamtime to pursue the challenging issues in synchrotron radiation research. A user team of the P-type proceeds an experiment by utilizing the advanced light source, especially high-speed polarization switching, of BL07LSU and by developing beamline and endstation technologies for the next generation light source.

It should be mentioned that the beginning of the year 2020, there has been a serious coronavirus (COVID-19) pandemic over the world and care has been urgently needed for those affected. In living, we have had to stop the spread of the virus by avoiding three Cs: closed spaces, crowded places, and close contact. No exception has been applied for experiments in any facilities or laboratories, including our beamline, SPring-8 BL07LSU. A number of the allocated beamtimes were split, canceled or postponed. However, the users were patient and worked their bests to proceed their research at each end-station, as briefly described below.

(1) Time-Resolved soft X-ray spectroscopy station (TR-SX spectroscopy)

The station is to perform time-resolved photoemission spectroscopy experiments by synchronizing the high-brilliant soft X-ray and the ultra-short laser pulses. A two-dimensional angle-resolved time-of-flight (ARTOF) analyzer is equipped for the efficient time-resolved measurements and the sample temperature can be controlled from 15 K to 1150K. The station adopts two different pumping laser systems synchronized with the

soft X-ray beam; low repetition rate and high pulse energy (1 kHz, mJ) and high repetition rate and low pulse energy (208 kHz, μJ).

In 2020, the experimental chamber and the ARTOF analyzer was transferred to a beamline of the vacuum ultraviolet/soft X-ray lasers (high-harmonic generation lasers) at Kashiwa campus in the University of Tokyo. This is because to improve temporal resolution of the system from picoseconds to femtoseconds for tracking the ultrafast dynamics that have not been observed at synchrotron radiation facilities yet. The last users were members of the Kagomiya group and they have succeeded in tracing dynamics of oxygen atoms during the current flow through the oxygen permeable membrane (*operando* experiment).

(2) Ambient-pressure X-ray photoelectron spectroscopy (AP-XPS)

AP-XPS station allows *operando* observation of catalysts under reaction conditions. The AP-XPS station was constructed in 2014 by an external funding (JST ACT-C project), and it became opened to external users since 2018. The AP-XPS system is equipped with a differentially pumped electron analyzer (SPECS, PHOIBOS 150 NAP) and an ambient-pressure gas cell. XPS measurements can be performed both under ultrahigh vacuum and in near-ambient gas pressure up to 20 mbar. Catalytic activity is monitored by mass spectrometer, and simultaneous evaluation of adsorbate and catalyst electronic states is performed. In addition to the experiments using synchrotron soft X-ray, off-line experiments can be performed by using a twin-anode X-ray source.

In 2020, a variety of research projects have been conducted at the AP-XPS station, for example, redox reaction on nanoparticles of transition metal, coupling reaction on model catalysts of metal/metal-oxides, and development of time-resolved AP-XPS.

(3) 3D-scanning photoelectron microscope (3D-nanoESCA)

3D-nanoESCA can be used for sub-100 nm range microscopic 2D mapping and depth profile of the chemical structure of functional materials and devices. In 2020, in collaboration with Drs. Asakura and Hosono at AIST group, chemical state mapping for Li and Ti was conducted on the $\text{Li}_4\text{Ti}_5\text{O}_{12}$ cathode of Li-ion battery (LIB) to elucidate two Li phases by local Li insertion/extraction reactions. Operando observation of Li domain wall migration in LIB was also carried out. Observation of solid electrolytes in all-solid-state batteries is also a challenge, and cooling trap mechanism is being developed to prevent adsorption of volatiles from X-ray irradiated samples.

(4) Ultra high-resolution soft X-ray emission spectroscopy (HORNET)

The station is dedicated for soft X-ray emission (or resonant inelastic X-ray scattering: RIXS) spectroscopy measurements with high-resolution ($E/\Delta E > 10,000$) and under various environmental conditions (gas, liquid, and solid).

In 2020, 13 proposals were accepted, and 4 proposals (Resonant inelastic soft X-ray diffraction of nanoparticles, elucidation of mechanism of induced structural change in thermo-responsive polymers, and observation of water alignment in polyelectrolyte membranes) were carried out by internal staff. The other nine projects were mostly carried out in the latter half of 2020 due to cancellation of user operation by the coronavirus pandemic. As one of the anti-coronavirus activities, RIXS was used to evaluate the function of biocompatibility on the surface of the inner tube of extracorporeal membrane artificial lung (ECMO) coated by poly(2-methoxyethyl acrylate) (PMEA) to inhibit thrombus formation. The result was used to synthesize more excellent biocompatible polymers, which was introduced in Nikkei newspaper and the paper has been submitted to Nature Communications.

Feasibility studies of five major companies were carried out using part of the beamline adjustment time for the next-generation synchrotron radiation.

(5) Soft X-ray imaging (Free-port station)

We have started to develop a microscopic imaging system using Wolter mirrors in the latter half of 2020 for use in the next-generation synchrotron radiation facilities. In collaboration with a company, we have already developed and evaluated a 200-mm-long large Wolter mirror. By introducing a mirror with a much larger aperture than conventional ones, we aim to develop a system that enables imaging with a minimum resolution of 50 nm. The main targets of the system are scanning X-ray microscopy and typography using a focusing profile without small chromatic aberrations. We also plan to use the long working distance of the soft X-ray mirror to perform tomography and operando measurements.

2. Status of spin- and angle-resolved photoelectron spectroscopy with laser light at Laser and Synchrotron Research Laboratory

Spin-and angle-resolved photoelectron spectroscopy (SARPES) is known as a powerful technique for studying spin-dependent electronic states in solids. Up to the 1990s, utilization of this technique was strongly limited into mainly ferromagnetic materials; the main target was their large exchange splitting (\sim several hundred meV) because the efficiency of spin detections was so low that one needs to sacrifice both energy and angular resolutions. However, the recent progress of the spin detector improves the efficiency and enables us to precisely investigate small spin-structures in non-magnetic spin-orbit coupled materials and even its unique texture in momentum space, such as Rashba spin-split systems and topological insulators. Recently, we have developed the SARPES apparatus using vacuum-ultraviolet ($h\nu=6.994\text{eV}$) lasers at Laser and Synchrotron Research Center (LASOR) in the Institute for Solid State Physics (ISSP) [1]. Our SARPES machine is currently utilized to obtain precise information on spin-dependent electronic structures near the Fermi level in solids (\sim several meV). We have started a project to construct the laser-SARPES machine from FY 2014 and joint researches at this station have started from FY2015.

Our laser-SARPES apparatus consists of an analysis chamber, a carousel sample-bank chamber connected to a load-lock chamber, and a molecular beam epitaxy (MBE) chamber. All of these chambers are connected via UHV gate valves. Figure 1 represents the hemispherical electron analyzer, which is custom-made ScientaOmicron DA30-L, modified to attach the very-low-energy-electron-diffraction (VLEED) type spin detectors. The electrons are currently excited by 6.994-eV photons, yielded by 6th harmonic of a high-power Nd:YVO₄ quasi-continuous wave laser. A helium discharge lamp (VG Scienta, VUV5000) is also available as a photon source. At the MBE chamber, samples can be heated by a direct current heating or electron bombardment. The surface evaluating and preparing

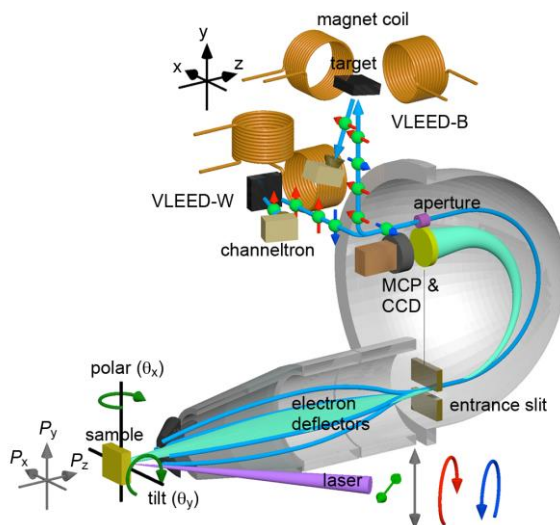


Figure 1: The laser-SARPES machine at LASOR at ISSP [1]. The double VLEED spin detectors are attached to a hemispherical analyzer (DA30-L, ScientaOmicron). Currently, 7-eV laser for high energy resolution measurement and 10.7eV pulsed laser for pump-probe measurement are available.

instruments, such as evaporators, low energy electron diffraction, sputter-gun and quartz microbalance, can be installed. At the carousel chamber, 16 samples can be stocked in the UHV environment. In FY2019, eleven research proposals from outside of the institute were accepted and conducted. Spin-polarized states were investigated in both bulk and surface of various topological materials including magnetic and superconducting ones, atomic layers, and ferromagnetic compounds.

Since FY2018, we have started to upgrade our laser-SAPRES apparatus to combine with a pump-probe laser technique. The laser system utilized for this project is a pulsed 10.7eV laser system, developed by Kobayashi group in LASOR at ISSP [2, 3]. This laser system is based on the Yb-doped fiber with the high repetition rate (1 MHz) with a pulse length of 270 fs. The light polarizations of 10.7eV can be selectively controlled by MgF₂ half-wave plate. In addition to a great capability of the time-resolution, our 10.7eV laser gives more wide momentum information in contrast to the low photon energy source such as 7eV, which is demonstrated in Figure 2. Thus, this state-of-the-art pump-probe SARPES apparatus can be widely used for studying unoccupied electronic states in spintronics materials and their ultrafast carrier/spin dynamics.

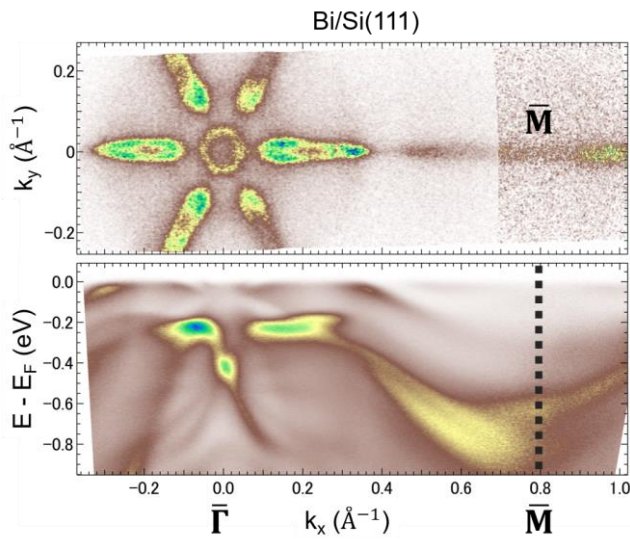


Figure 2: The Fermi surface mapping and band structure mapping for Bi thin films grown on Si(111) substrate, observed by 10.7eV laser [2, 3]. Such a photon energy can cover wide momentum information even around the Brillouin zone corner.

References:

- [1] K. Yaji, A. Harasawa, K. Kuroda, S. Toyohisa, M. Nakayama, Y. Ishida, A. Fukushima, S. Watanabe, C.-T. Chen, F. Komori and S. Shin, *Rev. Sci. Instrum.* 87, 053111 (2016).
- [2] Z. Zhao and Y. Kobayashi, *Opt. Exp.* 25, 13517 (2017).
- [3] Z. Zhao, K. Kuroda, A. Harasawa, T. Kondo, S. Shin and Y. Kobayashi, *Chin. Opt. Lett.* 17, 051406 (2019).

3. Workshops & Meetings

ISSP workshop: *Core technology toward the frontier soft X-ray science*

Date: 2021/3/4 (Thu.)

Place: On Zoom

Program:

10:00- **Opening Address**

Hatsumi Mori (ISSP, The University of Tokyo)

10:05- **Catalytic Surface Science Opened by Synchrotron Radiation X-ray Operando Measurements:
From SPring-8 BL07LSU to the Next-Generation Synchrotron Radiation Facility**

Susumu Yamamoto (International Center for Synchrotron Radiation Innovation Smart, Tohoku University)

10:35- **Frontier soft X-ray science in a spintronics device**

Shinji Miwa (ISSP, The University of Tokyo)

11:05- **Magnetic imaging with soft X-ray nanobeam formed by an ellipsoidal mirror**

Akihiro Suzuki (Research Institute for Electronic Science, Hokkaido University)

11:35- **Optics design for public beamlines of a new 3-GeV synchrotron radiation facility in Japan**

Takashi Imazono (National Institutes for Quantum and Radiological Science and Technology)

12:05- **lunch**

13:30- **Development of Soft X-ray Image Sensor sxCMS**

Shigetoshi Sugawa (New Industry Creation Hatchery Center, Tohoku University)

14:00- **Towards Visualization of Time Evolution by Coherent X-ray Diffraction Imaging**

Yukio Takahashi (International Center for Synchrotron Radiation Innovation Smart, Tohoku University)

14:30- **High-resolution X-ray microscope based on X-ray imaging mirrors**

Satoshi Matsuyama (Department of Materials Physics, Nagoya University)

15:00- **Development of novel soft X-ray imaging technique at BL07LSU**

Takashi Kimura (ISSP, The University of Tokyo)

15:30- **Coffee Break**

15:45- **Discussion on the next projects**

16:45- **Closing Address**

Yoshihisa Harada (ISSP, The University of Tokyo)

4. Seminar

Date: November 25, 2020

Title: Development of novel nanoimaging techniques using advanced x-ray light sources

Speaker: Dr. Takashi Kimura (ISSP, The University of Tokyo
PRESTO, Japan Science and Technology Agency)

ANALYSIS OF ELECTRONIC STATES IN WATER MOLECULES CONFINED IN BIOCOMPATIBLE POLYMER BRUSH DERIVATIVES USING SOFT X-RAY EMISSION SPECTROSCOPY

Keishi Akada¹, Shin-nosuke Nishimura², Kosuke Yamazoe¹, Daiki Murakami^{2,3}, Jun Miyawaki¹, Masaru Tanaka^{2,3}, Yoshihisa Harada¹

¹ *The Institute for Solid State Physics, The University of Tokyo,*

² *Institute of Materials Chemistry and Engineering, Kyushu University,*

³ *Graduate School of Engineering, Kyushu University,*

A characteristic water (Intermediate water) appearing at the liquid-polymer interface is considered as an origin of anti-fouling property of biocompatible materials such as poly (methoxyethyl acrylate) (PMEA) [1]. Control of intermediate water is possibly essential for the development of excellent biocompatible materials, but a mechanism of the biocompatibility is not fully understood. The intermediate water is considered to have a specific water structure [2], and an evaluation technique focusing on water is effective for understanding the physical properties. In this study, for investigating the structure of intermediate water, we conducted measurements using synchrotron soft X-ray emission spectroscopy (XES) which has an advantage in the measurement of hydrogen bond in water. An effect of polymer shape on biocompatibility was investigated by comparing the state of water on PMEAs, where the one polymer end is free in water, and in cyclic PMEAs (cPMEA) brush, where both of ends are fixed on substrate (Fig. 1). The difference of absorbed water may contribute to the improvement of biocompatibility, and will serve as a guideline for a development of biocompatible material.

As shown in Fig. 2, PMEAs and cPMEAs brushes were fixed onto an Au-coated 150 nm-thick SiC membrane for vacuum isolation in a solution cell. A humidifier (HUM-1, Rigaku Corp.) was used to flow a steam-nitrogen gas mixture over the SiC/Si substrate, enabling precise control of the humidity environment. This system enable us to detect changes of the electronic state of an absorbed water, from the first layer of water attached on the material surface to the multilayered state similar to bulk water. The O 1s XES measurement was performed using the SPring-8 BL07LSU ultra-high resolution soft X-ray emission spectrometer HORNET[3]

Fig. 3 shows a comparison of XES spectra of the PMEAs and cPMEAs brushes. The shapes of these peaks were almost the same up to 90%RH. This result indicates that there is no difference in the hydrogen-bonded

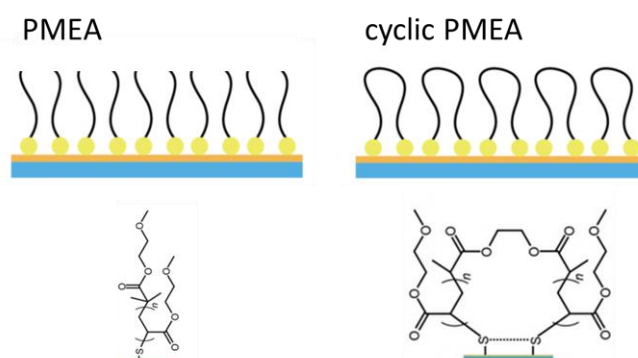


Fig. 1 Schematics and molecular structure of PMEAs and cyclic PMEAs brushes

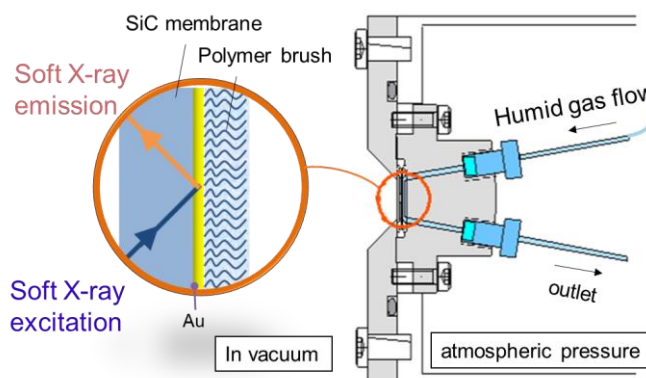


Fig. 2 Schematics of liquid cell for soft X-ray emission spectroscopy

network of water adsorbed on both samples at low humidity, and this result is reasonable because both polymers are composed of the same monomer. However, above 95%RH, a difference appeared between these samples. In PMEAs, the amount of the adsorbed water rapidly increased at 98%RH, and peak shape was drastically changed to the shape of bulk water. On the other hand, the spectrum of cPMEA gradually increased, and the bulk shape was not obtained even at RH98%. This indicates that cPMEA can contain large amount of water in its looped structure. Finally, the shape similar to the bulk was obtained at RH 99%, but the $1b_1''$ peak derived from the distorted hydrogen bond was still smaller than the bulk shape.

The detected water at low humidity was considered to be water molecules adsorbed on the functional groups of methoxyethyl acrylate (MEA), which is commonly exist in both polymers, because the spectral profiles were very similar between the two samples. On the other hand, water molecules adsorbed at high humidity (>95%RH) reflect the difference between the two samples, that was the absence/presence of the loop structure of the polymer. To discuss the properties of water adsorbed on cPMEA at each humidity, difference spectra between the neighboring humidities were extracted as shown in Fig. 4. Unexpectedly small increase in humidity caused a large change in the difference spectra, implying the presence of various stages of the water uptake in cPMEA. The difference spectrum to 96%RH has dominant $1b_1''$ component while that to 98%RH has dominant $1b_1'$ component, which would suggest the presence of water with highly distorted and ordered hydrogen bond depending on the humidity-controlled configuration of the trapped site in the looped PMEAs chain.

In conclusion, O 1s XES spectra of water in between the PMEAs and cPMEAs brushes showed significant difference at high (>95%RH) humidity: the cPMEA brush contained larger amount of water than the PMEAs brush, possibly due to water uptake in the looped chain. The observed change in the water structure unique to the looped chain may open a novel approach to control biocompatibility by designing materials surface to optimize the amount and hydrogen bonded structure of water.

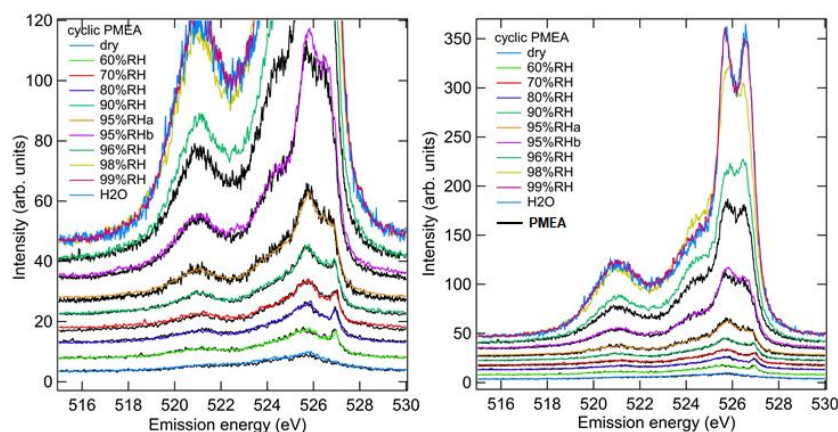


Fig. 3 Comparison of XES spectra from cPMEAs (colored) and PMEAs (black). The left panel is an enlarged plot of the right panel.

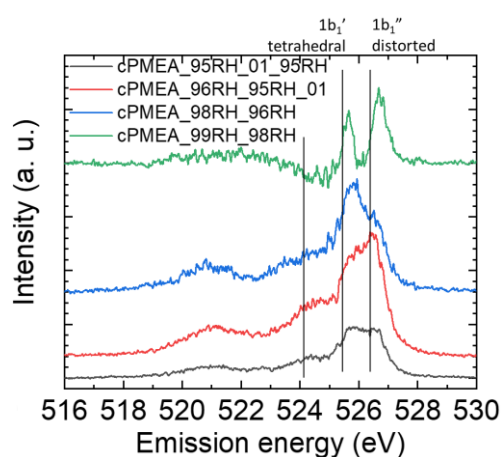


Fig. 4 Difference XES spectra from cPMEAs

REFERENCES

1. Tanaka, M. & Mochizuki, A. *J. Biomater. Sci. Polym. Ed.* **21**, 1849–1863 (2010).
2. Morita, S., Tanaka, M. & Ozaki, Y. *Langmuir* **23**, 3750–3761 (2007).
3. Harada, Y. *et al. Rev. Sci. Instrum.* **83**, 013116 (2012).

RESONANT SOFT X-RAY EMISSION SPECTROSCOPY OF A HIGH-VOLTAGE CATHODE MATERIAL

Daisuke Asakura^{1,2}, Eiji Hosono^{2,3}, Akihiro Ohira¹, Takaaki Sakai³, Kosuke Yamazoe⁴, Naoya Kurahashi⁴, Ralph J. Ugalino⁴, and Yoshihisa Harada^{2,4}

¹Research Institute for Energy Conservation, National Institute of Advanced Industrial Science and Technology (AIST)

²AIST-UTokyo Advanced Operando-Measurement Technology Open Innovation Laboratory, AIST

³Global Zero Emission Research Center, AIST

⁴Synchrotron Radiation Laboratory, The Institute for Solid State Physics, The University of Tokyo

All-solid-state Li-ion battery (LIB) is attracting much interest due to the safe operation of the solid-state electrolytes, while further enhancement of the energy density and power density is expected as with conventional LIBs which use organic-solvent electrolyte. $\text{LiNi}_{0.5}\text{Mn}_{1.5}\text{O}_4$ (LNMO) is one of the 5-V-class high-voltage cathode materials which contribute to enhance the power density and energy density of all-solid-state LIBs. LNMO has a high redox potential near 5 V vs. Li/Li^+ which is relatively higher than those of typical cathode materials such as LiCoO_2 (~3.9 V vs. Li/Li^+), LiMn_2O_4 (~4.0 V vs. Li/Li^+) and LiFePO_4 (~3.5 V vs. Li/Li^+). The electrochemical, chemical and physical properties of LNMO have been intensively investigated using general organic-solvent electrolyte. In parallel, studies for the application of LNMO to all-solid-state LIBs have been reported.¹

Previous studies including X-ray spectroscopic techniques have pointed out that the high voltage of LNMO is realized through a redox reaction of $\text{Ni}^{2+} \leftrightarrow \text{Ni}^{4+}$.² On the other hand, the property of the high oxidation state of Ni^{4+} for the charged LNMO is still under debate. Nanba *et al.* clarified a strong charge-transfer effect ($\text{O } 2p \rightarrow \text{Ni } 3d$ orbital) for the Ni^{4+} state of Ni-oxide cathode materials using Ni *L*-edge X-ray absorption spectroscopy (XAS) with multiplet calculation.³ Here, we demonstrate Ni *L*-edge XAS and resonant X-ray emission spectroscopy (RXES) for LNMO to further understand the Ni *3d* electronic structure.

A powdered LNMO sample was pasted with acetylene black and PTFE. The pasted LNMO electrode was assembled as coin-type cell with Li-metal counter electrode, an organic electrolyte solution and a separator. We prepared two cells to make charged-state samples with different modes; one is constant-current (CC) and the other is constant-voltage (CV) modes. The charged cells were disassembled in an Ar-filled glovebox. The LNMO samples were transferred from the glovebox to a transfer vessel without exposure to air. *Ex situ* Ni *L*-edge XAS and RXES measurements for the pristine and the two charged samples were carried out by HORNET spectrometer at BL07LSU, SPring-8. For XAS, bulk-sensitive partial-fluorescence-yield detection mode was employed. The energy resolution for the RXES measurement was set to 440 meV at 855 eV.

Figure 1 shows the Ni $L_{3,2}$ -edge XAS spectra. The pristine sample showed Ni^{2+} multiplet structure.³ For the charged sample with the CC mode, the XAS line shape can be roughly explained by the Ni^{3+} state while small amount of Ni^{2+} component should coexist.³ For the charged sample with the CV mode, the Ni L_3 and Ni L_2 XAS main peaks further shifted to higher energy, indicating further oxidized state.

The RXES results with an excitation energy of 854.2 eV (the dotted line in Fig. 1) are shown in Fig. 2. The RXES line shape for the charged sample with the CC mode is mostly different from that for the pristine sample, suggesting oxidation reaction to Ni^{3+} , while some

peaks from 1.6 to 3.4 eV remain unchanged. For the charged sample with the CV mode, the line shape is considerably different from that for the pristine sample.

The XAS and RXES results indicate that the charged sample with the CV mode was further oxidized. For more interpretations the XAS and RXES spectra will be analyzed with multiplet calculations. Also, we will try *operando* XAS/RXES measurement using an all-solid-state type cell in the near future.

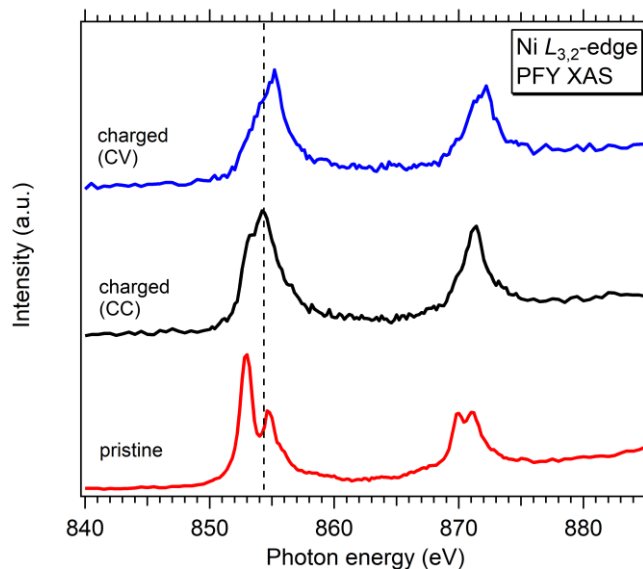


Fig. 1. Ni $L_{3,2}$ -edge XAS for the LNMO samples.

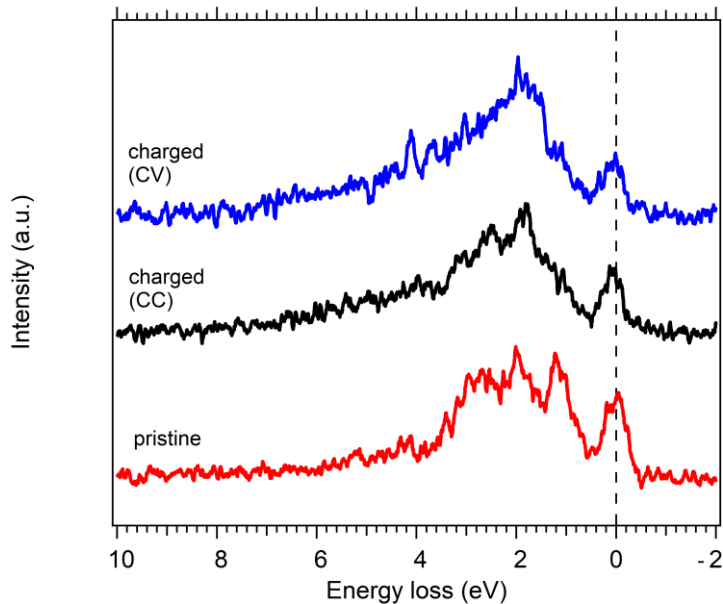


Fig. 2. Ni L_3 -edge XES for the LNMO samples (excitation energy: 854.2 eV).

REFERENCES

- [1] For example, H. Kawasoko *et al.*, ACS Appl. Mater. Interfaces **13**, 5861 (2021).
- [2] For example, C. A. Kim *et al.*, Electrochim. Acta **184**, 134 (2015) and S. Mukerjee *et al.*, Electrochim. Acta **49**, 3373 (2004).
- [3] Y. Nanba *et al.*, Chem. Mater. **28**, 1058 (2016).

ELECTRONIC STATE OF BULK SINGLE CRYSTAL Co_2FeSi HEUSLER ALLOY PROBED BY RESONANT INELASTIC SOFT X-RAY SCATTERING (SX-RIXS) IN MAGNETIC FIELD

Rie Y. Umetsu¹, Hidenori Fujiwara², Jun Miyawaki³, Kohei Nishimoto², Rika Kasahara², Yuto Arinaga², Akira Sekiyama², Yoshihisa Harada^{4,5} and Shigemasa Suga⁶

¹*Institute for Materials Research (IMR), Tohoku University, Miyagi, Japan*

²*Graduate School of Engineering Science, Osaka University, Osaka, Japan*

³*National Institutes for Quantum and Radiological Science and Technology (QST), Hyogo, Japan*

⁴*The Institute for Solid State Physics (ISSP), The University of Tokyo, Tokyo, Japan*

⁵*Synchrotron Radiation Research Organization, The University of Tokyo, Hyogo, Japan*

⁶*Institute of Scientific & Industrial Research, Osaka University, Osaka, Japan*

Introduction

Some of Mn- and Co-based Heusler alloys have been predicted to be half-metallic ferro- or ferri-magnets with the spin polarization of $\sim 100\%$ around the Fermi level (E_F) from theoretical calculations [1,2]. If the electrons are completely polarized around E_F , it is very efficient as a magnetic electrode in various spin dependent devices in the field of spintronics.

In the aspect of the fundamental investigations for half-metallic materials, it has been considered how to show the real evidence of the band gap character in their electronic state. Attempts have been made worldwide to observe the detailed electronic structure of Heusler alloys by photoelectron spectroscopy. The photoelectron orbit is greatly affected by the magnetic field, although a magnetic field must be applied in order to make a sample into a single domain state. In our previous work, we have studied the detailed electronic structure of single crystals of Mn_2VAl and Co_2MnSi alloys by soft x-ray resonant inelastic x-ray scattering (SX-RIXS) measurements in magnetic field [3,4]. The RIXS is a bulk sensitive photon-in and photon-out spectroscopy, and very powerful to investigate such as $d-d$ excitations for open shell $3d$ orbitals and magnetic excitations for spin systems as well as $2p-3d$ transitions in element- and symmetry-specific ways. In this study, we performed the RIXS experiments for single crystal of bulk Co_2FeSi Heusler alloy, which has been controversial being as the half-metallic ferromagnet, because the given spin polarization is different depending on the theoretical calculation method [5].

Experiments

a) Sample preparation

A single crystal of bulk Co_2FeSi was prepared by Bridgman method after preparing a master alloy by induction melting in Ar gas atmosphere, and annealed at 1423 K. The sample composition identified by scanning electron microscope-energy dispersive x-ray spectrometry is Co: 49.3, Fe: 25.4, Si: 25.3 at.%. Crystal orientation was checked by the Laue method and the specimens were cut out in the stripe form with the length of 5 mm along the $\langle 100 \rangle$ with about $1 \times 1 \text{ mm}^2$ cross section. Magnetic properties were investigated with SQUID magnetometer and the spontaneous magnetization at 5 K was 157.6 emu/g ($= 5.7 \mu_B/\text{f.u.}$), being comparable to the literature [6].

b) RIXS experiment

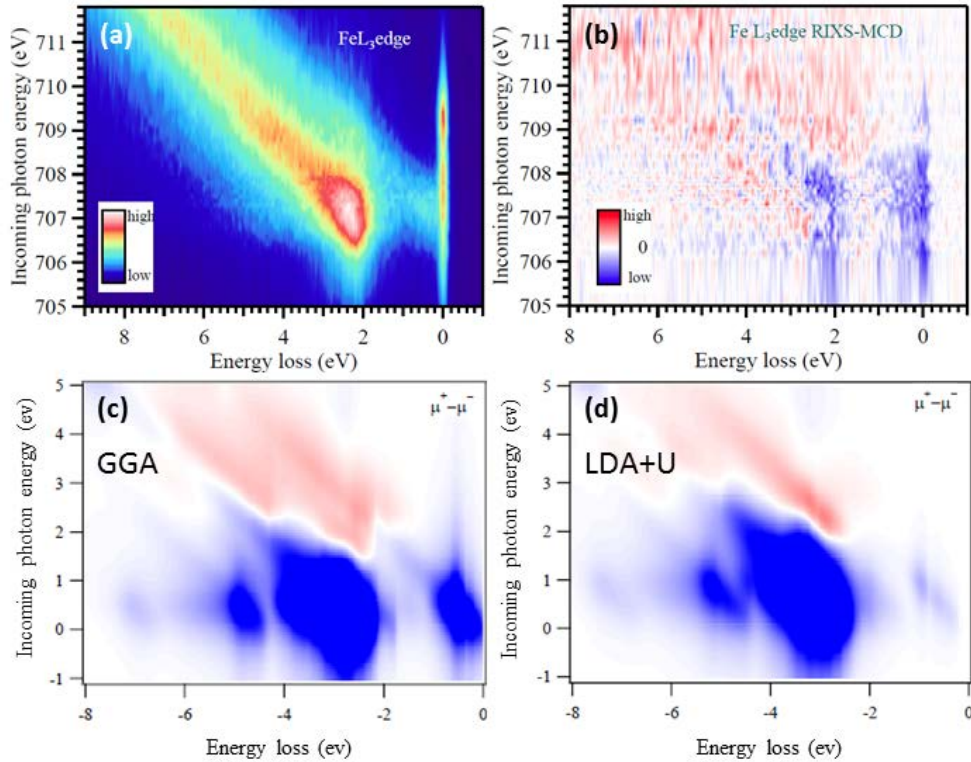
RIXS experiments were performed using a high-resolution soft x-ray emission spectrometer installed at the end of the BL07LSU of SPring-8. The specimen was fractured in a chamber. The RIXS spectra for Fe $2p$ core excitation were measured with use of the right and left helicity circularly polarized light at room temperature. A permanent magnet with the field of 0.25 T was installed in the chamber and arranged as the x-ray incidence direction and the magnetic field direction become parallel.

Results

Figure (a) indicates averaged RIXS spectra obtained in parallel (μ^+) and antiparallel (μ^-) configurations between the photon helicity and the magnetic field at incoming photon energy, for Fe- $2p_{3/2}$ edge. Strong scatterings without any energy loss are the elastic component, and the other scatterings in the larger energy loss region are the so-called fluorescence component. Clear fluorescence component is observed and their circular polarization dependence (MCD = $\mu^+ - \mu^-$) is also confirmed as shown in the Fig. (b). Between the elastic component and strong fluorescence component, a weak structure is observed at the incoming photon energy regions from 706 to 708 eV. Figs. (c) and (d) indicate simulated MCD spectra calculated based on the generalized gradient approximation (GGA) and local density approximation with considering the electron-electron correlation (LDA+U), respectively. The weak structure is well reproduced by the calculated spectra by GGA, suggesting the existence of the density of states of Fe-3d around E_F , that is, the spin polarization of the Co₂FeSi alloy would not be perfect.

REFERENCES

- [1] J.J. Kübler, A.R. Williams, C.B. Sommers, Phys. Rev. B 28 (1983) 1745-1755.
- [2] S. Ishida, S. Akazawa, Y. Kubo, J. Ishida, J. Phys. F 12 (1982) 1111-1122.
- [3] R.Y. Umetsu, H. Fujiwara, *et al.*, Phys. Rev. B 99 (2019) 134414.
- [4] H. Fujiwara, R.Y. Umetsu *et al.*, Preprint, DOI: 10.21203/rs.3.rs-637357/v1.
- [5] S. Wurmehl, G.H. Fecher, H.C. Kandpal, V. Ksenofontov, C. Felser, H.J. Lin, J. Morais, Phys. Rev. B 72 (2005) 184434.
- [6] P.J. Brown, R. Kainuma, T. Kanomata, K.-U. Neumann, A. Okubo, R.Y. Umetsu, K.R.A. Ziebeck, J. Phys.: Condens. Matter 25 (2013) 206002.



Figs. Averaged RIXS spectra recorded for parallel (μ^+) and antiparallel (μ^-) configurations of the photon helicity at Fe- $2p_{3/2}$ (a), and the MCD ($=\mu^+ - \mu^-$) spectra (b). (c) and (d) are calculated MCD spectra obtained by GGA and LDA + U, respectively.

NONPOLARIZING OXYGEN-REDOX CAPACITY WITHOUT O-O DIMERIZATION IN $\text{Na}_2\text{Mn}_3\text{O}_7$

Akihisa Tsuchimoto, Masashi Okubo

Department of Chemical System Engineering, School of Engineering, The University of Tokyo

There is an increasing demand for developing electrochemical energy storage with larger energy density, which can achieve electric vehicles with longer cruising range or large-scale applications for power grids. Lithium-ion battery is presently the most widely used energy storage device in commercial applications because of its high energy density, but its energy density has reached a plateau owing mainly to the small capacity of cathodes.

The capacity of conventional transition-metal layered oxides cathode materials like LiMO_2 (M : transition metals) is solely based on transition-metal redox, leading to a limited capacity. The recent discovery of $\text{Li}_{1+x}\text{M}_{1-x}\text{O}_2$ Li-rich transition-metal layered oxides with anionic redox chemistry are promising alternatives to traditional cathodes materials. In LiMO_2 conventional cathode materials, all oxygen $2p$ orbitals have σ -type bonds with transition metals and their energy level is lower than $M e_g$ orbitals, hence oxygen $2p$ orbitals have no contribution to redox capacity. On the other hand, $\text{Li}_{1+x}\text{M}_{1-x}\text{O}_2$ cathode materials have localized oxygen $2p$ orbitals along the Li-O-Li axis without σ -type bonds, which enables additional oxygen redox capacity and nearly doubled energy density.

However, most oxygen redox cathode materials suffer from large voltage hysteresis between charge and discharge, which means energy loss, and the mechanism for this energy loss have not been fully understood yet. Although kinetic hysteresis arising from the structural instability such as cation migration and surface densification considered to be a part of cause of energy loss, a large voltage hysteresis is still observed in sodium counterpart $\text{Na}_x\text{M}_y\text{O}_2$ where cation migration are suppressed by the larger difference of ionic size. As high energy efficiency is requisite to commercial applications, the voltage hysteresis of oxygen redox cathodes needs to be improved.

Although it is generally accepted that oxygen $2p$ states without M-O σ -type bonds are localized and then contribute to redox capacity, the chemical state of oxidized oxygen is still under debate. The large voltage hysteresis indicates that it includes thermal hysteresis from the transformation of oxygen atoms. Oxidized oxygen atoms $\text{O}^{\cdot-}$ are considered to form stable peroxide-like O_2^{2-} dimers upon charge, and these O_2^{2-} dimers may be initially reduced to O_2^{4-} and then decomposed to O^{2-} upon subsequent discharge¹.

We have recently found a “non-polarizing” oxygen-redox capacity of $\text{Na}_2\text{Mn}_3\text{O}_7$ that possesses inherent Mn vacancies in a layered structure². Unlike most oxygen redox cathode materials, oxygen redox in $\text{Na}_2\text{Mn}_3\text{O}_7$ is expected to be based on the reversible redox couple of $\text{O}^{2-}/\text{O}^{\cdot-}$. However, although preliminary theoretical calculations

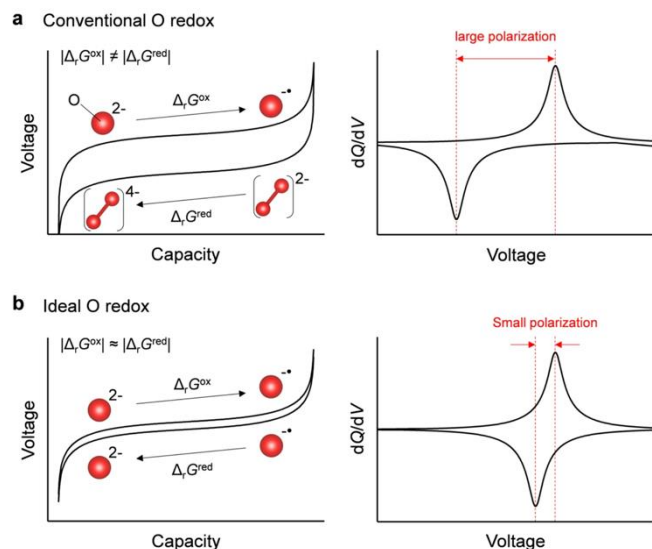


Figure 1. Schematic illustration of charge/discharge curves and dQ/dV plots (Q : specific capacity, V : reaction voltage) for **a** conventional oxygen redox with large polarization ($\text{O}^{2-}/\text{O}_2^{2-}$), and **b** ideal oxygen redox with small polarization ($\text{O}^{2-}/\text{O}^{\cdot-}$). The red sphere denotes oxygen atom.

suggested that the nonbonding $2p$ orbitals of oxide ions neighboring the Mn vacancies contribute to the oxygen-redox capacity, the origin for the non-polarizing oxygen-redox capacity of $\text{Na}_2\text{Mn}_3\text{O}_7$ is yet to be fully understood. In this work, using resonant inelastic X-ray scattering (RIXS) spectroscopy for O K -edge and magnetic susceptibility measurements, we attempt to probe the electronic structural change and the chemical state of the oxidized oxygen species.

$\text{Na}_2\text{Mn}_3\text{O}_7$ was synthesized from a solid-state reaction following a reported procedure². Galvanostatic charge/discharge measurements are performed using coin-type Na half cells with synthesized $\text{Na}_2\text{Mn}_3\text{O}_7$ as the cathode active material. $\text{Na}_{2-x}\text{Mn}_3\text{O}_7$ delivers a reversible capacity of approximately 70 mAh/g at C/20 rate between 3.0 and 4.7 V vs. Na/Na⁺, which is consistent with a previous report². Figure 2a shows the dQ/dV plot for $\text{Na}_{2-x}\text{Mn}_3\text{O}_7$ during the second charge/discharge cycle. As the valence state of Mn in $\text{Na}_{2-x}\text{Mn}_3\text{O}_7$ is 4+ which is maximum of Mn in octahedral sites, this redox capacity is attributed to oxygen redox. Importantly, the voltage hysteresis in the charge/discharge of $\text{Na}_{2-x}\text{Mn}_3\text{O}_7$ (0.03-0.04 V) is significantly smaller than that of other oxygen redox cathodes (~ 1.00 V), indicating reversible redox couple of O^{2-}/O^- .

O K -edge X-ray absorption spectroscopy (XAS) and RIXS data are collected in BL07LSU in SPring-8 to probe the electronic structural change of oxygen. In the O K -edge XAS spectra on the second cycle (Figure 2b inset), a new emerged absorption peak at 531.5 eV is observed, which correspond to the excitation of O $1s$ to O $2p$ hole. To probe the electronic structure of occupied state in addition to unoccupied state probed by XAS, RIXS spectra were measured using 531.5 eV incident X-ray. The emergence of a new emission peak at 523.0 eV is observed and this behavior is typical for other oxygen redox materials. This new inelastic scattering can be explained by both cases, O^- formation and peroxide-like O_2^{2-} formation, therefore, further experimental evidence is needed to identify the chemical states of oxygen.

Considering the spin state of oxidized oxygen, oxygen species should be distinguished by magnetic susceptibility measurements. While the spin state for O^- is $S=1$, the spin state for O_2^{2-} is $S=0$. The change in Curie constants before/after the second cycle is deduced from χ^{-1} vs. T plot (χ : magnetic susceptibility) based on the Curie-Weiss law, and the experimental values ($5.77 \text{ cm}^3 \text{ K mol}^{-1} \rightleftharpoons 4.22 \text{ cm}^3 \text{ K mol}^{-1}$) are more plausible when assuming O^- as an oxidized species ($5.63 \text{ cm}^3 \text{ K mol}^{-1} \rightleftharpoons 4.75 \text{ cm}^3 \text{ K mol}^{-1}$) than O_2^{2-} ($5.63 \text{ cm}^3 \text{ K mol}^{-1} \rightleftharpoons 5.63 \text{ cm}^3 \text{ K mol}^{-1}$)³. Overall, the existence of stable O^- was identified in $\text{Na}_2\text{Mn}_3\text{O}_7$.

REFERENCES

1. Sathiya, M. et al., *Nat. Mater.* 12, 827–835 (2013).
2. Mortemard de Boisse, B. et al., *Adv. Energy Mater.* 8, 1800409 (2018).
3. Tsuchimoto, A. et al., *Nat Commun* 12, 631 (2021).

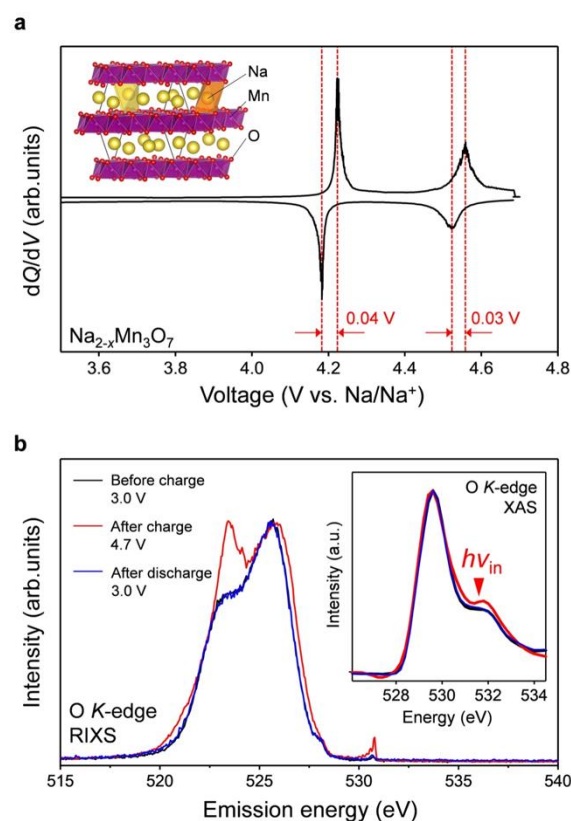


Figure 2. a dQ/dV plot (Q : specific capacity, V : reaction voltage) of $\text{Na}_{2-x}\text{Mn}_3\text{O}_7$ at C/20 during the second charge/discharge cycle between 3.0–4.7 V vs. Na/Na⁺. Inset shows the crystal structure of $\text{Na}_2\text{Mn}_3\text{O}_7$. b O K -edge resonant inelastic X-ray scattering (RIXS) spectra for $\text{Na}_{2-x}\text{Mn}_3\text{O}_7$ before the second charge (3.0 V, black line), after the second charge (4.7 V, red line), and after the second discharge (3.0 V, blue line) with excitation energy of 531.5 eV. Inset shows corresponding O K -edge X-ray absorption spectra (XAS).

Operando analysis of electronic structure of catalytic active sites in redox flow batteries

Akihiro Ohira^{a,b}, Eiji Hosono^{a,b,c}, Daisuke Asakura^{a,b,c}, Takaaki Sakai^{a,b}, Kosuke Yamazoe^c, Naoya Kurahashi^e, Yoshihisa Harada^{c,d,e}

^a National Institute of Advanced Industrial Science and Technology (AIST), Research Institute for Energy Conservation, 1-1-1 Umezono, Tsukuba, Ibaraki 305-8568, Japan

^b National Institute of Advanced Industrial Science and Technology (AIST), Global Zero Emission Research Center, 1-1-1 Umezono, Tsukuba, Ibaraki 305-8568, Japan

^c AIST-UTokyo Advanced Operando-Measurement Technology Open Innovation Laboratory, 5-1-5 Kashiwanoha, Kashiwa, Chiba 277-8565, Japan

^d Institute for Solid State Physics (ISSP), The University of Tokyo, 5-1-5 Kashiwanoha, Kashiwa, Chiba 277-8581, Japan

^e Synchrotron Radiation Research Organization, The University of Tokyo, 7-3-1 Hongo, Bunkyo-ku, Tokyo, 113-8656, Japan

We are exploring materials to improve the performance for redox flow batteries (RFBs), one of the energy storage technologies that will facilitate the mass adoption of renewable energies.^{1,2} RFBs mainly consist of an electrolyte containing the active materials responsible for redox reactions, an electrolyte membrane that divides the positive and negative electrodes, and electrodes that carry out the redox reactions of the active materials. RFB typically involves a redox reaction between vanadium's $V^{4+} \rightleftharpoons V^{5+}$ (cathode) and $V^{3+} \rightleftharpoons V^{2+}$ (anode) at both electrodes, and the electromotive force is obtained from the difference in their respective reaction potentials, resulting in a battery capacity that depends on the vanadium concentration.³

High performance in RFBs mean improvement of energy density and power density, and to realize the improvement of energy density and power density, it is important to understand the redox reaction at the interface between the active material and the electrode. Specifically, it is necessary to clarify the solvation and de-solvation behavior of the active material due to the redox reaction in solution, and the active sites that contact and react with the active material at the electrode interface. In particular, it is important to analyze the electronic state of the electrode material, because the electronic state is different between the catalytic state along with the electrochemical reaction and the non-reacted powder state. Considering the electronic state of an electrochemical catalyst in an oxidation reaction, the occupied/unoccupied orbitals examined in absorption and emission spectroscopy are very different because the Fermi level is shifted by about 1 V in the oxidation state of +1 V electrochemically (vs. SHE) from the unreacted state. Therefore, it is necessary to analyze the electronic state during operation as a device in order to better understand the electrode reaction and discuss the correlation between the high-performance material and the electronic state. Therefore, in this project, we will attempt to analyze the above solvation and de-solvation behaviors and the reaction active sites on the electrode surface by detailed electronic analysis using techniques such as soft x-ray absorption spectroscopy (XAS) and soft x-ray emission spectroscopy (XES). In this study, XAS and XES measurements of vanadium solid and solution with different valence were carried out as a preliminary investigation of the change in electronic state of the active material, which is an important factor in the analysis of catalytic reactions.

Solutions of V^{5+} , V^{4+} , V^{3+} , and V^{2+} were prepared by charging and discharging 3M H_2SO_4 dissolved with 1M $VOSO_4$ (V^{4+}) at a current density of 70 mA/cm² and discharge voltage of 1.6V to 1.0V using a small RFB cell. The UV spectra confirmed that the respective

electrolytes were prepared.

About 10 μl of these vanadium solutions were dropped onto a 5 mm² Si₃N₄ substrate, and the solid samples of V⁵⁺, V⁴⁺, V³⁺, and V²⁺ were prepared by heating and vacuum drying. In addition, oxygen *K*-edge absorption and emission measurements were carried out by XAS and XES experiments using an *operando* cell with SiC window/Ti/Au electrodes developed by AIST and the University of Tokyo using BL07LSU.

The powder sample on Si₃N₄ substrate was mounted on a sample holder to perform XAS and XES measurements (Fig 1). For the solution samples, 3M H₂SO₄ was used as a reference. In the XAS measurement at the oxygen *K*-edge, different spectra were obtained depending on the valence of the solution: V⁵⁺, V⁴⁺, V³⁺, and V²⁺. In the XES spectra with excitation energy of 550 eV, 1b', an indicator of hydrogen bond formation, and 1b'', an indicator of hydrogen bond breaking, were also different. The trend of change was different between the cathode side (V⁴⁺ and V⁵⁺) and the anode side (V²⁺ and V³⁺).

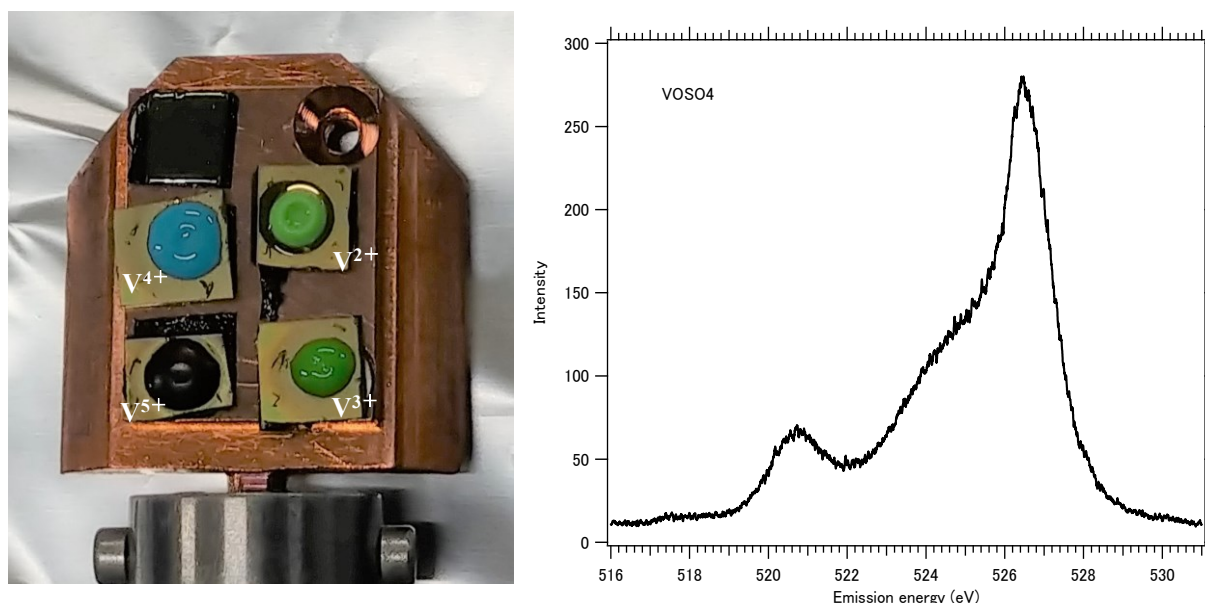


Figure 1. Vanadium solid samples and oxygen *K*-edge XES spectrum of VOSO₄ powder.

REFERENCES

- [1] B. Zakeri, S. Syri, *Renewable and Sustainable Energy Reviews*, 42, 569 (2015).
- [2] F. Shi, *Reactor and Process Design in Sustainable Energy Technology*, Elsevier Amsterdam (2016).
- [3] M. S. Kazacos, M. Rychcik, R. G. Robin, A. G. Fane, *J. Electrochem. Soc.*, 133, 1057 (1986).

SOFT X-RAY CORE-LEVEL SPECTROSCOPY ON SURFACES IN MIXED CONDUCTIVE OXIDES DURING OXYGEN PERMEATION

Isao Kagomiya^a, Tomohiro Hirano^a, Yutaro Yagi^a, Susumu Yamamoto^b, Iwao Matsuda^c

^aLife Science and Applied Chemistry, Nagoya Institute of Technology,

^bInstitute of Multidisciplinary Research for Advanced Materials, Tohoku University

^cSynchrotron Radiation Laboratory, The Institute for Solid State Physics, The University of Tokyo

Oxygen permeability of mixed ionic-electronic conductive oxide (MIEC) is an important compound for developing applications, such as cathodes employed in solid oxide fuel cells (SOFCs) and oxygen separation membranes used for supplying oxygen from the air. For the applications, we need higher oxygen permeability at lower temperatures than 800 °C. To improve oxygen permeability, promoting surface exchange reaction during the oxygen permeation is a significant strategy. However, the detailed factor dominating surface exchange reaction is still unclear. This study tried to make clear the factor by investigating soft X-ray core-level spectroscopy (XPS) on the MIEC surface during permeating oxygen.

This study focuses on $\text{La}_{0.65}\text{Ca}_{0.35}\text{FeO}_{3-\delta}$ (LCF) perovskite as a MIEC, which shows higher oxygen permeability, compared to the $\text{La}_{0.6}\text{Sr}_{0.4}\text{Co}_{0.2}\text{Fe}_{0.8}\text{O}_{3-\delta}$ of a typical MIEC [2, 3]. The LCF films were prepared on the one side of dense yttria-stabilized zirconia (YSZ) pellets by using a spin-coating technique. After spin-coating, the LCF film on the YSZ pellet was fired at 600 °C for 5 min. The thickness of the prepared LCF film was approximately 1.2 μm . The Pt paste including the 10wt% carbon was printed on the opposite side of the YSZ pellet and then fired at 1200 °C.

XPS spectra of the prepared LCF film on YSZ were collected at the soft x-ray beamline BL07LSU at SPring-8. Energy of the incident beam was set at 700 eV. The sample was heated from ambient temperature up to approximately 600 °C. The current was applied in the range of -0.5 to 0.5 mA to let the LCF film permeate oxygen at 600 °C as illustrated in Fig. 1. The binding energy was calibrated by using Au 4f. Each intensity and position of peak top in XPS spectra with applying current was normalized by those with no applying current.

Figure 2 shows XPS spectra of O1s core level at 600 °C under different applying current conditions of 0.42, 0 and -0.34 mA. The O1s XPS spectra is composed of three components, corresponding to lattice oxygen (~529 eV), surface-lattice termination layer (~530 eV) and surface secondary phases of hydroxides or carbonated oxides (~531 eV). Figure 2 shows that

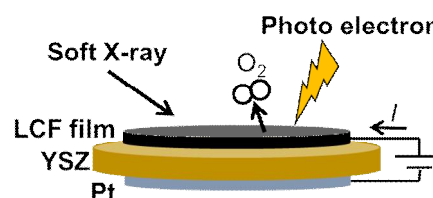


Fig. 1: Setup for XPS measurement during oxygen permeation

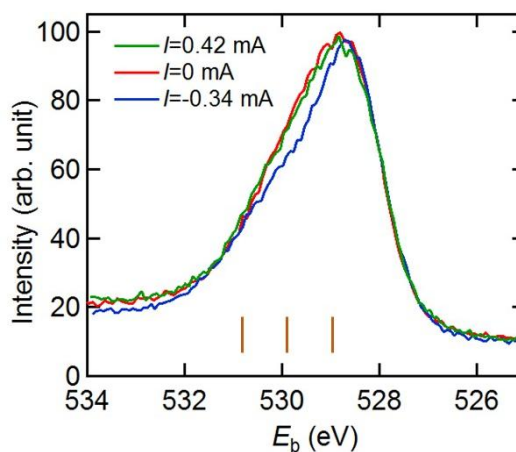


Fig. 2: XPS spectra of O1s core level at 600 °C under different applying current condition

amount of the oxygen on surface-lattice termination layer decreases with applying negative current. When the negative current is applied, the surface oxygen is incorporated into LCF film. We consider that oxygen on the termination layer disappears during incorporating oxygen. Based on the consideration, the oxygen on the termination layer corresponds to desorbing or adsorbing oxygen during permeating oxygen. The component of ~530 eV in Fig. 2 depended on no applied positive current, suggesting that amount of surface oxygen relating to desorption kept constant during the oxygen permeation. The other components (lattice oxygen and surface secondary phases) depended on no applying current.

This study concludes that oxygen on surface-lattice termination layer take an important role of the surface exchange reaction during the oxygen permeation.

REFERENCES

- [1] E.J. Crumlin, E. Mutoro, Z. Liu, M.E. Grass, M.D. Biegalski, Y-L. Lee, D. Morgan, H.M. Christen, H. Bluhm, Y. Shao-Horn, *Energy Environ. Sci.*, **5**, 6081 (2012)
- [2] I. Kagomiya, T. Murayama, K. Tsunekawa, K. Kakimoto, Y. Ogura, *J. Eur. Ceram. Soc.*, **39**, 1082 (2019).
- [3] I. Kagomiya, T. Takahashi, K. Kakimoto, *Chem. Mat.*, **31**, 10135 (2019).

AMBIENT PRESSURE X-RAY PHOTOELECTRON SPECTROSCOPY ON SURFACES IN MIXED CONDUCTIVE OXIDES AT ELEVATED TEMPERATURES

Isao Kagomiya^a, Tomohiro Hirano^a, Takayuki Kato^a, Susumu Yamamoto^b, Iwao Matsuda^c

^a*Life Science and Applied Chemistry, Nagoya Institute of Technology*

^b*Institute of Multidisciplinary Research for Advanced Materials, Tohoku University*

^c*Synchrotron Radiation Laboratory, The Institute for Solid State Physics, The University of Tokyo*

Mixed ionic-electronic conductive oxides (MIEC) show oxygen permeability, which properties are applicable to cathodes employed in solid oxide fuel cells (SOFCs) and oxygen separation membranes used for supplying oxygen from the ambient air. The higher oxygen permeability of mixed conductive oxides reduces activation polarization resistances when they are used as cathodes in SOFCs and allows the generation of pure oxygen gas at higher rates. Thus we need MIEC with higher oxygen permeability. Particularly, the application requires high oxygen permeability at lower temperatures than 1073 K for decreasing the operation temperatures. The slower surface exchange reaction at lower temperatures is a main reason for limiting oxygen permeability at lower temperatures.

The previous our study found that oxygens on the surface take an important role of the surface exchange reaction. The state of the surface would strongly depend on the circumambient atmosphere, particularly oxygen partial pressure (P_{O_2}) near the MIEC sample surface. With the point of view, this study investigated near-ambient pressure X-ray photoelectron spectroscopy (XPS) of the MIEC surface under different P_{O_2} conditions.

The precursor ceramic powders of a mixed conductive $La_{0.65}Ca_{0.35}FeO_{3-\delta}$ (LCF) [1, 2] were prepared by a citrate-based liquid mixing technique [3]. The prepared ceramic powders were calcined at 1173 K for 5 h. The calcined powders were molded into a pellet and then pressed with 300 MPa pressure by using a cold isostatic pressing machine (CIP). Finally, the pressed pellets were sintered at 1573 K for 10 h under ambient air. The XPS spectra of the prepared LCF ceramic samples were collected by using the ambient pressure XPS instrument installed at BL07LSU at SPring-8. Energy of the incident beam was set at 700 eV. To investigate the influence of temperature on the XPS spectra, the LCF sample was heated from ambient temperature up to 660 K. The binding energy was calibrated by using Au film located on the LCF sample surface.

Figure 1 shows XPS spectra of O1s core level at 660 K under the different P_{O_2} conditions of 1 and 0.1 mbar. The component corresponding to surface secondary phases of hydroxides or carbonated oxides (~531 eV) increased with increases in P_{O_2} . The other components corresponding to lattice oxygen (~529 eV) and surface-lattice termination layer (~530 eV) showed no remarkable changes. The result suggests that the increase in P_{O_2} adsorbs more hydroxides or carbonated oxides on the LCF film surface. The secondary phases on the surface would prevent permeating oxygens. More detailed P_{O_2} dependence of surface state during the oxygen permeation is needed to make clear effects of P_{O_2} on the surface exchange reaction.

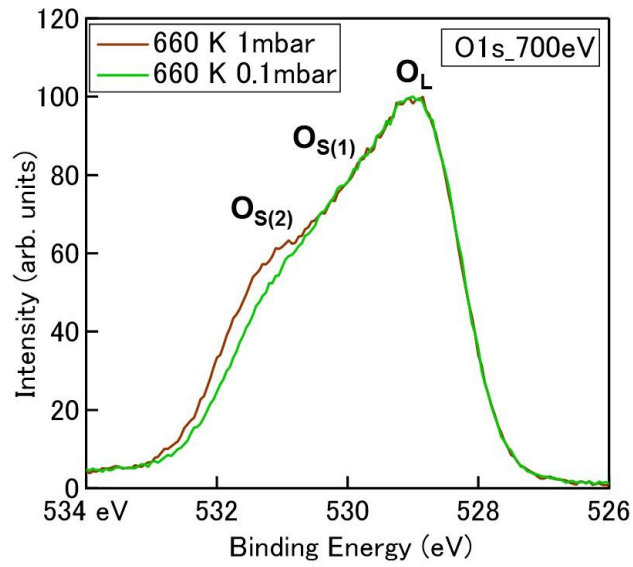


Fig. 1: XPS spectra of $O1s$ core level at $600\text{ }^{\circ}\text{C}$ under different P_{O_2} condition. O_L : lattice oxygen; $O_{S(1)}$: surface-lattice termination layer; $O_{S(2)}$: surface secondary phases.

REFERENCES

- [1] I. Kagomiya, T. Murayama, K. Tsunekawa, K. Kakimoto, Y. Ogura, *J. Eur. Ceram. Soc.*, **39**, 1082 (2019).
- [2] I. Kagomiya, T. Takahashi, K. Kakimoto, *Chem. Mat.*, **31**, 10135 (2019).
- [3] M.P. Pechini, U.S. Patent #3330697 (1967).

ANALYSIS OF INTERACTIONS BETWEEN POLYAMIDE AND WATER MOLECULES IN REVERSE OSMOSIS MEMBRANES BY XAS, XES AND RIXS

Jumpei Yahiro¹, Koichi Ozaki¹, Masaru Nakada¹, Masahiro Kunisu¹, Harutoki Shimura², Shinya Mitsui², Naoya Kurahashi³, Kosuke Yamazoe³, and Yoshihisa Harada³

¹*Toray Research Center, Inc.,*

²*Toray Industries, Inc.*

³*The Institute for Solid State Physics, The University of Tokyo*

Introduction

The demand for seawater desalination has been increasing in the background of the water shortage with the global economic development and the environmental pollution. In particular, reverse osmosis (RO) desalination has been especially focused on from the viewpoint of energy saving [1]. A typical RO membrane consists of three layers: a separation functional layer, a supporting layer, and a substrate. The separation functional layer has sub-nanometer scale pore structure inside it. This pore structure selectively separates water molecules and other substance, e.g., ions and organic compounds. In our previous study, the pore structure in the RO membrane contained at least two kinds of water molecules: the water which confined by hydrogen bonding with polyamide chains (bound water), and the water which existed at a distance from polyamide chains (free water) [2]. Additionally, it is suggested that the strength of the amide-amide hydrogen bonds in polyamide interacts the growth of water channels which are composed with free water [3]. The water channels make rapid diffusion of water molecules. Therefore, the control of both bound and free water in the water channel structure is important to improve both the permeability and the selectivity in the RO membrane. Furthermore, the method to analyze the state of the bound and the free water is necessary. In this study, we examine the electronic states of the water in water channel structure using X-ray absorption spectroscopy (XAS), X-ray emission spectroscopy (XES) and resonant inelastic X-ray scattering (RIXS).

Experimental

The RO membranes were prepared as below procedures. The dried RO membrane was prepared to dehydration under a vacuum condition at room temperature for 12 h. The water content RO membranes at different concentrations were prepared in a condition of 90% relative humidity. O *K*-edge XAS, XES and RIXS measurements were performed at the BL07LSU HORNET station in SPring-8. The dried RO membrane was measured in a high vacuum condition by mounted on a Cu sample plate. The water content RO membranes were measured using a liquid flow cell which could place RO membranes under flowing liquid or gas [4]. The low water content RO membrane was measured by fastened in a liquid flow cell in a condition of 90% relative humidity. The high water content RO membrane was measured by fastened in the liquid flow cell under flowing dried nitrogen gas after flooded.

Results and Discussion

Figure 1 shows the O *K*-edge XES spectra of pure water, the water content RO membranes, and the dried RO membrane at the excitation energy of 550 eV (non-resonant). The XES spectra were normalized by integral intensity in the region 510 eV and 540 eV. In the XES spectrum of pure water, the characteristic peaks ($1b_1'$, $1b_1''$, $3a_1$) were observed. The O *K*-edge XES spectra of the water content RO membranes contain X-ray emission signals from oxygens both of water molecules and polyamide chains. Subtracting the spectrum of the dried RO membrane from that of the water content RO membrane, we could extract the spectrum of the water molecules in the pore. Figure 2 shows the extracted spectra of water contribution in RO membranes. The $1b_1'$ peak intensity was lower than $1b_1''$ peak in the low water content RO membrane clearly. Furthermore, the $3a_1$ peak intensity increased with decreasing water

content. The XES spectrum of gas phase water has the dominant $1b_1'$ and $3a_1$ peaks [5], which features are similar to the low water content RO membranes. Therefore, it is indicated that the water molecules exist in isolation in the pore. Figure 3 shows the O K -edge RIXS spectra of the low water content RO membrane and dried RO membrane at the excitation energy of 531.3 eV. The RIXS spectra were normalized by integral intensity in the region 510 eV and 530 eV. In the XAS spectra, the absorption peak of the carbonyl bond oxygen appeared at 531.3 eV (data not shown). Therefore, the RIXS spectra at the excitation energy of 531.3 eV are attributed to the electronic states around the carbonyl bond oxygen in polyamide. The peak intensity around 523.5 eV in the low water content RO membrane was higher than that in dried RO membrane. The peak dominantly appeared in the low water content RO membrane, indicating to attribute to the change of electronic states by interaction between the carbonyl bond oxygens and water molecules. In conclusion, we observed the electronic states of water molecules in the pore and the interactions between water molecules and polyamide chains. As a next step, we aim to observe the water contents dependence of the water molecules behavior in the pore and to assign the peaks in RIXS spectra at the excitation energy of 531.3 eV related the interactions of polyamide chains.

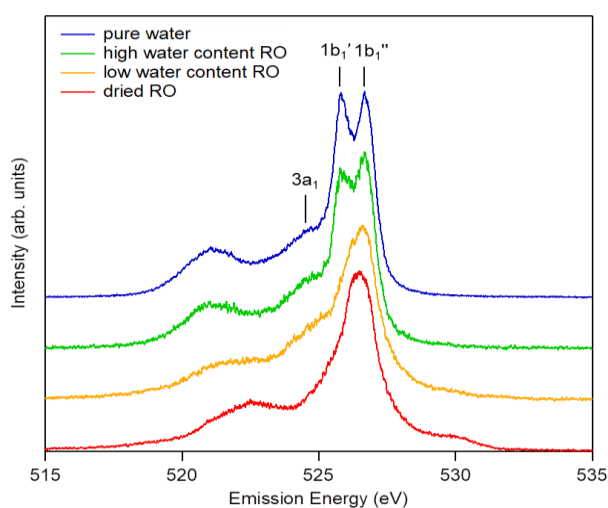


Figure 1. O K -edge XES spectra of pure water, water content RO membranes and dried RO membrane at the excitation energy of 550 eV.

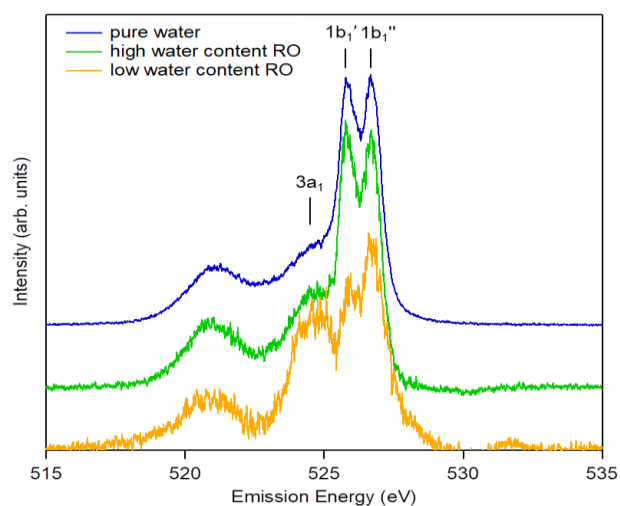


Figure 2. O K -edge XES spectra of water content RO membranes subtracted the spectrum of the dried RO membrane from the raw spectrum.

References

- [1] S.S. Shenvi, et al., *Desalination* **368**, 10 (2015).
- [2] T. Kawakami, et al., *Polym. J.*, **50**, 327 (2018).
- [3] D. Surblys, et al., *J. Membr. Sci.*, **596**, 117705 (2020).
- [4] K. Yamazoe et al., *Langmuir* **33** 3954 (2017).
- [5] T. Tokushima et al., *Chem. Phys. Lett.* **460** 387 (2008).

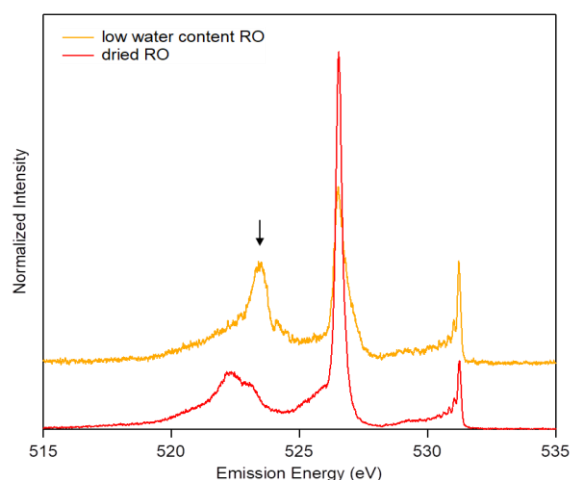


Figure 3. O K -edge RIXS spectra of water content RO membrane and dried RO membrane at the excitation energy of 531.3 eV.

STUDY ON HYDROGEN BOND STRUCTURE OF WATER MOLECULES IN POLYMER ELECTROLYTE

Naoya Kurahashi¹, Kosuke Yamazoe², Ugalino Ralph John³, Jun Miyawaki⁴, Keishi Akada¹ and Yoshihisa Harada¹

¹*Synchrotron Radiation Laboratory, The Institute for Solid State Physics, The University of Tokyo*

²*Japan Synchrotron Radiation Research Institute*

³*Graduate School of Frontier Sciences, The University of Tokyo*

⁴*National Institutes for Quantum and Radiological Science and Technology*

A fuel cell is a power generation device that directly converts chemical energy such as hydrogen into electrical energy. Fuel cells are highly energy efficient and do not generate carbon dioxide during power generation, so they are expected to contribute to the reduction of greenhouse gas emissions. In Japan, stationary fuel cells for home use were put on the market in 2009, and fuel cell vehicles were put on the market in 2014. Polymer electrolyte fuel cells (PEFCs) are being installed in automobiles because they are small and can generate electricity at low temperatures. However, further spread and expansion are required.

In PEFCs, when hydrogen gas is supplied to the anode, hydrogen ions (protons = H^+) are generated on the electrodes. The generated protons pass through the polymer electrolyte membrane (PEM) and move to the cathode, where the protons react with oxygen gas to generate energy and water molecules. Therefore, the PEM must have high gas barrier properties, water resistance, and mechanical strength, while allowing only protons to permeate with high efficiency. Most of the polymers used in PEMs have a structure in which a strong acid group such as a sulfo group is introduced at the end of a hydrophobic skeleton. When these macromolecules aggregate, they take an inverted micelle structure and form nanometer-order channel structures.¹ When the PEM is humidified, water is taken into the channel and protons are released from the superacid group, which is thought to be a conduction path for protons.² Therefore, it is necessary to evaluate the network structure of water molecules in the PEM in order to understand the proton permeability. However, experimental research was lacking because it was difficult to directly observe the water molecules incorporated inside the membrane. One of the authors have previously attempted to evaluate the mobility of water molecules incorporated into the Nafion membrane using nuclear magnetic resonance spectroscopy. As a result, it was clarified that the mobility of water molecules changes significantly across a temperature of around 15 °C. The authors predicted that the change in the mobility was induced by the change in the size of the proton channel, but could not reach a conclusion only by the NMR measurement. Therefore, in this work, we explored more detail of the hydrogen bond network of water through the electronic states of water molecules in the proton channel by soft X-ray emission spectroscopy. The sample was prepared by casting a commercially available Nafion suspension onto a SiC plate and volatilizing the solvent. By controlling both the

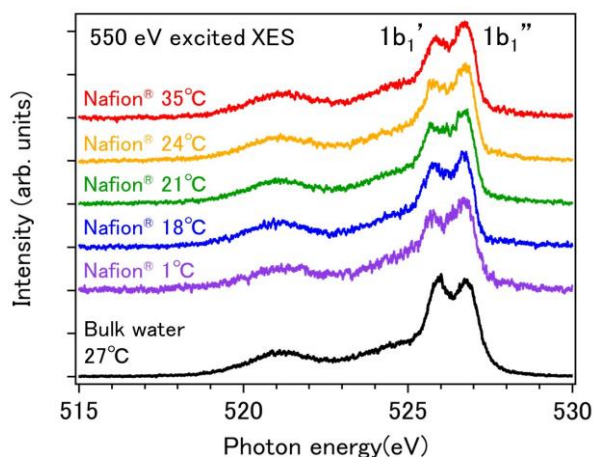


Fig. 1 Soft X-ray emission spectrum of bulk water and water molecules in Nafion at 80% relative

temperature and humidity using an atmosphere control cell, the temperature dependence of the electronic state was measured.

We evaluated the irradiation damage to Nafion because it was reported that soft X-rays would damage fluorinated materials.³ In the emission spectroscopy, the sample is moved at regular intervals to prevent damage to the SiC window and the sample, so that the same place is not continuously irradiated with synchrotron X-rays. From our systematic test by changing the X-ray irradiation time per point, it was concluded that damage to Nafion can be avoided if the X-ray irradiation time is 5 seconds per point or less. Within the damage-free scan, soft X-ray emission spectra of Nafion in two conditions, circulating nitrogen gas in a dry and 80 % relative humidity conditions were measured, and the difference spectra between the two were obtained for different temperatures, which extract the emission signal derived from water molecules incorporated into the Nafion membrane.

The soft X-ray emission spectra measured with photon energy of 550 eV and energy resolution of 150 meV are shown in Fig. 1. The XES profile of the water incorporated into the Nafion suggests that the water molecules form clusters with highly distorted or broken hydrogen bonds. To analyse the temperature dependence of the XES profile, each spectrum was fitted with four gaussians, and the intensity ratios of the $1b_1'$ and $1b_1''$ derived peaks (Fig. 2 red circle) as well as the separation energy of the $1b_1'$ and $1b_1''$ peaks (Fig. 2 blue square) were evaluated. In bulk water, the $1b_1''/1b_1'$ intensity ratio increases with temperature because the hydrogen bonds in water are distorted by thermal fluctuations. The energy separation of the $1b_1'$ and $1b_1''$ peaks also increases with temperature because the $1b_1''$ peak shifts to higher energy with temperature to accommodate entropy gain while the $1b_1'$ peak stays constant since the tetrahedrally coordinated water is stabilized only by enthalpy gain and just decrease the population with temperature.⁴ Intriguingly, the results observed for Nafion water are different from the trends expected for bulk water in terms of both the intensity ratio ($1b_1''/1b_1'$) and the peak separation energy; both have a minimum at around 18 °C, albeit the values are still larger than those of bulk water at 27 °C. The unique temperature-dependent behaviour of this water should be related to the temperature dependent local configuration figured by Nafion. In the near future, the determinants of the structure of water in Nafion will be clarified by comparison with simulations, which is expected to lead to the fine control of proton conductivity.

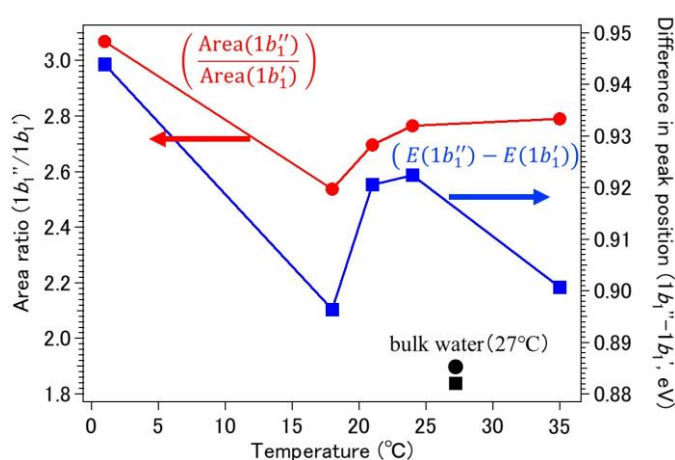


Fig. 2 Area intensity ratio of the $1b_1'$ and $1b_1''$ peaks (circle, left axis) and the peak energy difference (square, right axis) of water in Nafion evaluated from peak separation of the XES spectra. The black circle and square are the results of bulk water.

REFERENCES

- [1] M. Rikukawa, J. Synth. Org. Chem. Jpn. **66**, 488 (2008).
- [2] M. Yoshida-Hirahara *et al.*, RSC Adv. **10**, 12810 (2020).
- [3] L. G. de A. Melo *et al.*, Microsc. Microanal. **21**, 2443 (2015).
- [4] P. Gallo *et al.*, Chem. Rev. **116**, 7463 (2016).

METHANE CONVERSION REACTION ON PT AND PD MODEL CATALYSTS STUDIED BY OPERANDO AMBIENT-PRESSURE XPS

Takanori Koitaya

Department of Materials Molecular Science, Institute for Molecular Science

INTRODUCTION

Activation of methane on metal surfaces has been widely studied. For example, symmetry of methane adsorbed on Pt surfaces is reduced to C_{3v} [1], and electronic interaction between methane molecules and Pt substrate is detected by X-ray absorption spectroscopy (XAS) [2]. Recently, we have investigated the interaction of methane with the Pd(110) surface by means of X-ray photoelectron spectroscopy (XPS), XAS and first-principle calculations, and revealed that one of the C-H bonds in adsorbed methane is softened through the electronic interaction with the Pd surface [3]. The previous studies indicate that transition metals are good catalysts for methane activation, but they are conducted under ultra-high vacuum (UHV), which is a quite different condition compared with real catalytic reaction conditions.

In this study, the methane oxidation reaction on Pt surfaces was studied by ambient-pressure (AP-XPS). AP-XPS is a powerful tool for *Operando* observation of catalytic reaction. The surface chemical states are detected by measurements of chemical shift of substrate and adsorbate core-levels. In addition, reaction products desorbed from a catalytic surface are also monitored by photoionization of gas-phase molecules.

EXPERIMENTAL

The experiments were performed using the AP-XPS apparatus equipped at BL07LSU [4]. The AP-XPS measurements were carried out using a differentially pumped electron analyzer (SPECS, PHOIBOS 150 NAP) with an ambient-pressure gas cell. The gas cell was equipped in an UHV analysis chamber (base pressure = 3×10^{-10} mbar), which makes it possible to perform the AP-XPS measurements under well-defined conditions. XPS measurements can be performed in near-ambient pressure up to 20 mbar by using a small aperture ($\phi 0.3$ mm).

The Pt surfaces were cleaned by cycles of Ar^+ sputtering and annealing at 1000 K in a preparation chamber (base pressure = 3×10^{-10} mbar). All the XPS spectra were obtained with a photon energy of 715 eV.

RESULTS AND DISCUSSION

The methane oxidation reaction was investigated at a sample temperature of 650 K. The reaction products are monitored C 1s, O1s XPS and quadrupole mass spectrometer (QMS) equipped in a differentially pumped lens chamber. The main products under this reaction condition are CO_2 , CO and water. Fig. 1 shows QMS signals of produced CO_2 on Pt(111) as a function of oxygen flow rate. At lower flow rate less than $0.4 \text{ cm}^3/\text{min}$, the amount of CO_2 increased linearly, indicating that collision frequency of oxygen molecules onto the Pt surface is a key factor determining reaction rate for the methane oxidation. In contrast, the higher oxygen flow rates lead to a steep decrease in the reactivity.

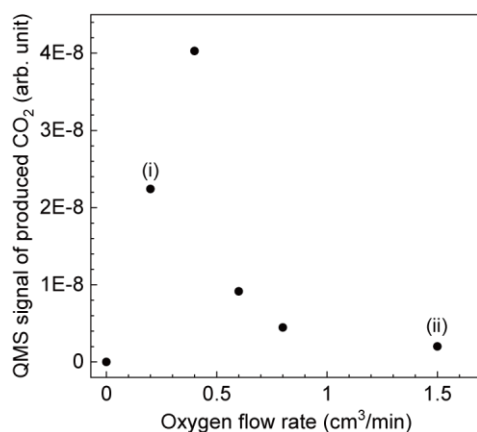


Fig. 1. The amount of produced CO₂ as a function of oxygen flow rate (sample temperature = 650 K, methane flow rate = 7.0 cm³/min)

The flow-rate dependent reactivity was further investigated by AP-XPS. Fig. 2 shows Pt 4f core-levels spectra of Pt(111) at oxygen flow rates of (i) 0.2 cm³/min (reactive condition), and 1.5 cm³/min (inert condition). The spectrum of the reactive Pt surface shows a peak at 70.5 eV, which is assigned to bare Pt atoms at the surface. This results clearly shows that the Pt(111) surface is clean even in the near-ambient condition. On the other hand, the bare surface Pt peak was completely disappeared and a new peak was appeared at higher binding energy in the case of the inert reaction condition. The new peak is attributed to be Pt atoms binding with surface oxygen atoms. Therefore, the active site for the methane oxidation is a bare metallic surface, and surface oxygen significantly suppress the methane activation.

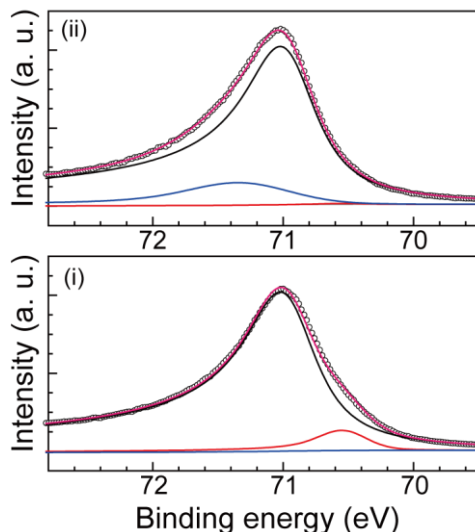


Fig. 2. AP-XPS spectra of the Pt(111) surface in the reaction condition (i) and (ii) indicated in Fig. 1.

REFERENCES

- [1] J. Yoshinobu, H. Ogasawara, and M. Kawai, *Phys. Rev. Lett.* **75**, 2176 (1995).
- [2] H. Öström, H. Ogasawara, L. Å. Näslund, K. Andersson, L. G. M. Pettersson, and A. Nilsson, *J. Chem. Phys.* **127**, 144702 (2007).
- [3] T. Koitaya, A. Ishikawa, S. Yoshimoto, and J. Yoshinobu, *J. Phys. Chem. C* **125**, 1368 (2021).
- [4] T. Koitaya *et al.*, *Top. Catal.* **59**, 526 (2016).

DIRECT OBSERVATION OF METHANE OXIDATIVE COUPLING REACTION ON PALLADIUM BASED ALLOYS BY AMBIENT-PRESSURE XPS

Takanori Koitaya

Department of Materials Molecular Science, Institute for Molecular Science

INTRODUCTION

It is indispensable to develop a highly functional catalyst for efficient use of methane as a chemical feedstock. Alloying is one of the promising methods for controlling catalytic activity of transition-metal catalysts. Palladium is a good catalyst for oxidation of methane. A previous our study has shown that the active site for the methane oxidation is a PdO film that is formed on the surface in the presence of the feed gases. Therefore, in-situ observation of surface chemical states is important for understanding the reaction mechanism.

In this study, methane conversion reaction on the Pd-Au alloy foil was investigated by means of the *operando* AP-XPS to reveal the effect of the alloying.

EXPERIMENTAL

The experiments were performed using the AP-XPS apparatus equipped at BL07LSU [1]. The AP-XPS measurements were carried out using a differentially pumped electron analyzer (SPECS, PHOIBOS 150 NAP) with an ambient-pressure gas cell. The gas cell was equipped in an UHV analysis chamber (base pressure = 3×10^{-10} mbar), which makes it possible to perform the AP-XPS measurements under well-defined conditions. The AP-XPS measurements can be performed in near-ambient pressure up to 100 mbar by using a small aperture (ϕ 0.05 mm).

The Pd-Au alloy samples (Au: 18 at%) were cleaned by cycles of Ar⁺ sputtering and annealing at 723 K in a preparation chamber (base pressure = 3×10^{-10} mbar). All the XPS spectra were obtained with a photon energy of 1096 eV.

RESULTS AND DISCUSSION

The methane oxidation reaction was investigated using a quadrupole mass spectrometer (QMS). Fig. 1 shows sample temperature and QMS spectra of produced CO₂, CO and water. In this experiment, 16 mbar O₂ and 17 mbar methane was introduced into the gas-cell, and then the sample was heated at a rate of 0.05 K/s. When the sample was heated to 615 K ((i) in Fig. 1), the amount of the products was very small, indicating that the sample surface was inert. The Pd 3d spectrum in Fig. 2(a) shows two peaks: bulk Pd and surface oxide.

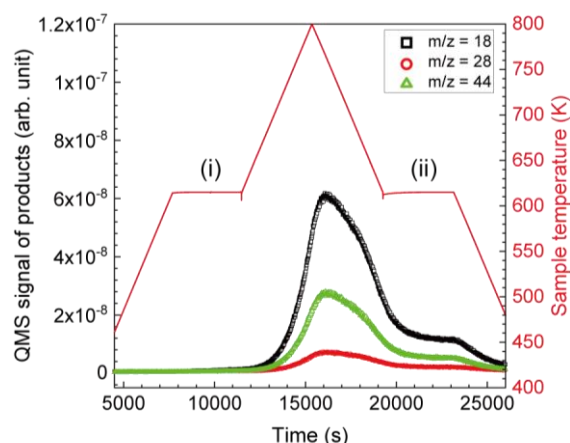


Fig. 1. Sample temperature and QMS signal of reaction products as a function of reaction time.

During heating to 800 K, the QMS signals of the reaction products increased in intensity as a function of the sample temperature. The sample was then cooled to 615 K again (ii). It should be noted that the reactivity on this surface is significantly higher compared to the condition (i). The Pd 3d AP-XPS spectra show oxidation of Pd to PdO. In addition, the intensity of Au 4f spectra is decreased. These spectral changes indicate that the Pd atoms in the alloy sample are segregated on the surface, and active PdO sites are formed. Surface adsorbate and reaction products are monitored C 1s (Fig. 2c). The surface coverage of reaction intermediates is very small, and only the peaks of the gas-phase molecules (methane and CO₂) were observed. This result suggests that reaction and desorption of reaction intermediates and products are fast, and that rate controlling step in the methane oxidation is a dissociative adsorption of methane.

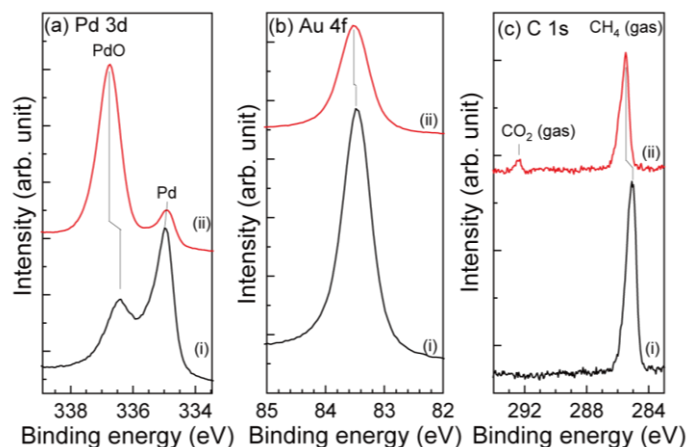


Fig. 2. (a) Pd 3d, (b) Au 4f, and (c) C 1s AP-XPS spectra measured in the reaction conditions (i) and (ii) indicated in Fig. 1.

REFERENCES

- [1] T. Koitaya *et al.*, *Top. Catal.* **59**, 526 (2016).

Broad Spectral Feature due to p - d Hybridization in p -Type Ferromagnetic Semiconductor (In,Mn)As

Masaki Kobayashi^{1,2}, Kohsei Araki¹, Takahito Takeda¹, Le Duc Anh¹, Atsushi Fujimori^{3,4}, Jun Miyawaki^{5,6}, Yoshihisa Harada⁵, Shinobu Ohya^{1,2}, and Masaaki Tanaka^{1,2}

¹*Department of Electrical Engineering and Information Systems, The University of Tokyo*

²*Center for Spintronics Research Network, The University of Tokyo*

³*Department of Physics, The University of Tokyo*

⁴*Department of Applied Physics, Waseda University*

⁵*Synchrotron Radiation Laboratory, The Institute for Solid State Physics, The University of Tokyo*

⁶*Institute for Advanced Synchrotron Light Source, National Institutes for Quantum and Radiological Science and Technology*

Ferromagnetic semiconductors (FMSs) are alloy semiconductors doped with a sizable amount of magnetic impurities (typically a few percent or more). The ferromagnetism in FMS is considered to be induced by charge carriers, thus called *carrier-induced ferromagnetism*. Since this property enables us to control the magnetic properties by carriers through electrical and optical means, FMSs have attracted much attention in the research field of spintronics [1,2]. From the fundamental science point of view, the origin of the carrier-induced ferromagnetism in FMS is still under debate. (In,Mn)As is a conventional p -type III-V-based FMS showing carrier-induced ferromagnetism [3,4]. Previously, it has been found that post-growth annealing on (In,Mn)As thin films leads to the increase of hole-carrier concentration and raises the Curie temperature (T_C) [5,6]. Thus, (In,Mn)As provides an ideal platform to elucidate the carrier-concentration dependence of the physical properties of (In,Mn)As. The knowledge of the electronic structure of FMS is indispensable for understanding the mechanism of ferromagnetism [7-10]. In this study, we have performed X-ray absorption spectroscopy (XAS) and resonant inelastic X-ray scattering (RIXS) measurements on (In,Mn)As thin films with varying hole-carrier concentrations to reveal the origin of the ferromagnetism in (In,Mn)As.

(In_{0.93}Mn_{0.07})As thin films were grown on conductive n^+ -InAs(100) substrates by the molecular beam epitaxy (MBE) method. The sample structure was In_{0.93}Mn_{0.07}As (50 nm)/InAs (50 nm)/ n^+ -InAs(100) substrate from top to bottom. The samples were covered by an amorphous As layer to protect the surface from oxidization. Post-growth annealing at 250 °C was performed on the as-grown samples for 10 min or 30 min to increase the hole-carrier concentration. The Curie temperature (T_C) increases with increasing the annealing time, while the as-grown (In,Mn)As film show paramagnetism due to its low carrier concentration. The T_C values of the samples annealed for 10 min and 30 min were 35 K and 55 K, respectively, as determined by the Arrott plot of the magnetic circular dichroism intensity. The hole concentrations estimated from T_C were below 3×10^{19} , $\sim 4 \times 10^{19}$, and $\sim 3 \times 10^{20}$ cm⁻³ for the as-grown, 10-min annealed, and 30-min annealed samples, respectively. The RIXS and XAS experiments were conducted using the high-resolution soft X-ray emission spectrometer HORNET [12] at beamline BL07LSU of SPring-8 [13]. The total energy resolution for the RIXS measurements was ~ 170 meV at the Mn L_3 edge. The RIXS spectra were measured with linear horizontal polarization at room temperature. The

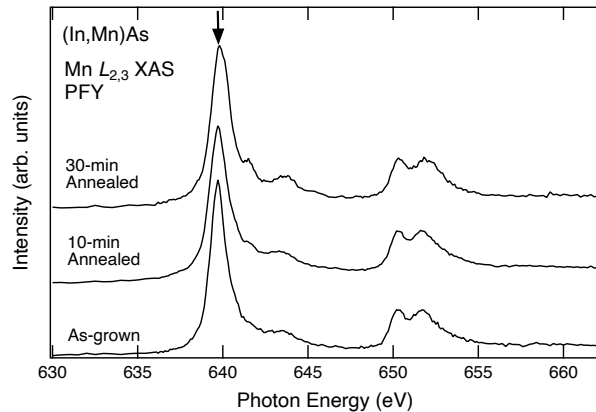


FIG. 1: Fe $L_{2,3}$ XAS spectra of (In_{0.93}Mn_{0.07})As thin films. The signals were collected in the TFY mode. The arrow denotes the excitation energy for RIXS measurements.

XAS signals were collected in the total-fluorescence yield (TFY) mode. Here, the probing depths of RIXS and TFY-XAS are expected to be several hundreds nm due to the long penetration depth of X-rays.

Figure 1 shows the Fe $L_{2,3}$ XAS spectra of the $(\text{In}_{0.93}\text{Mn}_{0.07})\text{As}$ thin films. All the three samples show a similar spectral feature having a single peak at the L_3 edge and double peaks at the L_2 edge. Note here that there are finite changes in the spectra, i.e., a shoulder structure and small peaks appear with annealing. Interstitial Mn defects acting as double-donors in $(\text{In},\text{Mn})\text{As}$ are supposed to be thermally diffused out to the surface by the post-growth annealing, thus increasing the hole concentration. The small spectral changes may come from the modification of the electronic structure of the Mn ion with increasing the hole concentration as well as from the out-diffused Mn atoms that were oxidized on the surface.

Figure 2 shows the Mn L_3 RIXS spectra of the $(\text{In},\text{Mn})\text{As}$ thin films measured at 639.7 eV. The spectra are normalized to the areas and plotted as a function of energy loss. In general, a RIXS spectrum is sensitive to the local electronic structure of the Mn $3d$ orbitals [14]. Although the energy resolution is high enough to resolve each $d-d$ excitation peak [12], the RIXS spectra of the doped Mn ions show a broad spectral feature irrespective of the hole concentration. Since the $d-d$ excitation energy of localized $3d$ orbitals like MnO are discrete, RIXS spectra

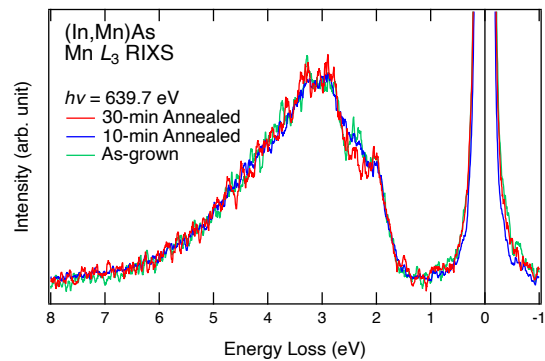


FIG. 2: Mn L_3 RIXS spectra of $(\text{In}_{0.93}\text{Mn}_{0.07})\text{As}$ thin films. The excitation photon energy is 639.7 eV.

of such localized $3d$ orbital show a spectral feature with multiple peaks [12]. Thus, the broadened spectral line shape observed in $(\text{In},\text{Mn})\text{As}$ suggests the $d-d$ excitation involving a localized bound hole state due to strong hybridization between the Mn $3d$ orbitals and ligand As $4p$ bands.

For a further analysis, comparison of the RIXS spectra with configuration-interaction cluster-model calculation is desirable [8]. This analysis will enable us to estimate the electronic structure parameters. The calculations will reveal the difference in the electronic structure between $(\text{In},\text{Mn})\text{As}$ and $(\text{Ga},\text{Mn})\text{As}$ [8].

In conclusion, we have performed XAS and RIXS measurements at the Mn L edge of $(\text{In},\text{Mn})\text{As}$ thin films with varying the hole concentration. The RIXS spectra show a broad spectral feature irrespective of the hole concentration, indicating that the Mn $3d$ orbitals well hybridizes with the ligand band in $(\text{In},\text{Mn})\text{As}$ as well as $(\text{Ga},\text{Mn})\text{As}$.

REFERENCES

- [1] T. Dietl, *Nature Mater.* **9**, 965 (2010).
- [2] M. Tanaka, *Jpn. J. Appl. Phys.* **60**, 010101 (2021).
- [3] H. Munekata *et al.*, *Phys. Rev. Lett.* **63**, 1849 (1989).
- [4] H. Ohno *et al.*, *Nature* **408**, 944 (2000).
- [5] Y. Hashimoto *et al.*, *J. Cryst. Growth* **237-239**, 1334 (2002).
- [6] Y. Iye *et al.*, *Mater. Sci. Eng. B* **63**, 88 (1999).
- [7] M. Kobayashi *et al.*, *Phys. Rev. B* **89**, 205204 (2014).
- [8] M. Kobayashi *et al.*, *Phys. Rev. Lett.* **112**, 107203 (2014).
- [9] S. Sakamoto *et al.*, *Phys. Rev. B* **95**, 075203 (2017).
- [10] T. Takeda *et al.*, *Phys. Rev. B* **101**, 155142 (2020).
- [11] M. Kobayashi *et al.*, *Phys. Rev. B* **103**, 115111 (2021).
- [12] Y. Harada *et al.*, *Rev. Sci. Instrum.* **83**, 013116 (2012).
- [13] Y. Senba *et al.*, *Nucl. Instrum. Methods Phys. Res., Sect. A* **649**, 58 (2011).
- [14] L. J. P. Ament *et al.*, *Rev. Mod. Phys.* **83**, 705 (2011).

LI INSERTION MECHANISM OF OCTAHEDRAL $\text{Li}_4\text{Ti}_5\text{O}_{12}$ SINGLE CRYSTALLINE PARTICLE BY MAPPING MEASUREMENT OF 3DNANOESCA

Wenxiong Zhang^a, Eiji Hosono^{b,c,d}, Daisuke Asakura^{c,d}, Naoka Nagamura^e,
Masaharu Oshima^f, Yoshihisa Harada^{a,d,f}

^a *Institute for Solid State Physics (ISSP), The University of Tokyo,
5-1-5 Kashiwanoha, Kashiwa, Chiba 277-8581, Japan*

^b *National Institute of Advanced Industrial Science and Technology (AIST), Global Zero Emission
Research Center, 1-1-1 Umezono, Tsukuba, Ibaraki 305-8568, Japan*

^c *National Institute of Advanced Industrial Science and Technology (AIST), Research Institute for
Energy Conservation, 1-1-1 Umezono, Tsukuba, Ibaraki 305-8568, Japan*

^d *AIST-UTokyo Advanced Operando-Measurement Technology Open Innovation Laboratory, 5-1-5
Kashiwanoha, Kashiwa, Chiba 277-8565, Japan*

^e *National Institute for Materials Science, Research Center for Advanced Measurement and
Characterization, 1-2-1 Sengen, Tsukuba, Ibaraki 305-0047, Japan*

^f *Synchrotron Radiation Research Organization, The University of Tokyo, 7-3-1
Hongo, Bunkyo-ku, Tokyo, 113-8656, Japan*

$\text{Li}_4\text{Ti}_5\text{O}_{12}$ (LTO) has drawn considerable attention as lithium-ion battery anode materials owing to its cycling stability and high-rate performance, as well as its improved safety over graphite. It features that: relatively safe operational potential (1.55V vs. Li^+/Li), zero volume change during the discharge/charge process and excellent Li ions insertion/extraction reversibility, which makes it one of the most promising anode materials. Recently, microspectroscopic photoelectron images of the LTO electrode with a spatial resolution of 100 to 200 nm have been obtained by using 3DnanoESCA. The change in the valence of Ti due to Li insertion was observed on LTO active material during the charge/discharge process.¹ However, the Li insertion mechanism is not yet clear for LTO octahedron single crystalline particle, which is essential for material optimization. To elucidate the mechanism, the *ex-situ* LTO samples with octahedral morphology after the discharge treatment have been prepared (Figure 1a). By the mapping of the particles via 3DnanoESCA at BL07LSU of SPring-8,² it is anticipated to see the Li-rich and Li-poor phases from the mapping image of triangular facet of LTO octahedron particle (Figure 1a).

During the 3DnanoESCA measurement, after focusing on the LTO particle (adjustment of the place of the holder, Fresnel zone plate and order-sorting pinhole aperture), a rough image of a wide area would be scanned. Subsequently, the resolution would be improved to about 100 nm to obtain a local image of the octahedral particle by further adjusting the focus. Then, the mapping process would appropriately be employed to elucidate the Li distribution on the LTO particle surface.

As shown in Figure 1c, O 1s mapping image of the LTO particles obtained by 3DnanoESCA measurement shows the resolution comparable to the optical image (Figure 1b). SEM images obtained after the measurement showed clear octahedral LTO particle with triangular facet (Figure 1d). Correspondingly, the triangular facet from the mapping image showed relatively inferior resolution (Figure 1c). Taken into consideration of low conductivity of LTO, the charging-up happened during the mapping process of the LTO particle when smaller scanning step was used for mapping (100 nm/spot). Therefore, the larger scanning step (200 nm/spot) was conducted with sacrificing the resolution of the mapping image. As a result, it was not possible to observe the movement of the domain wall of the two phases depending on the amount of Li insertion. In the near future, increasing the

conductivity by coating the carbon on the LTO surface will be conducted to directly observe the domain wall movement with better resolution.

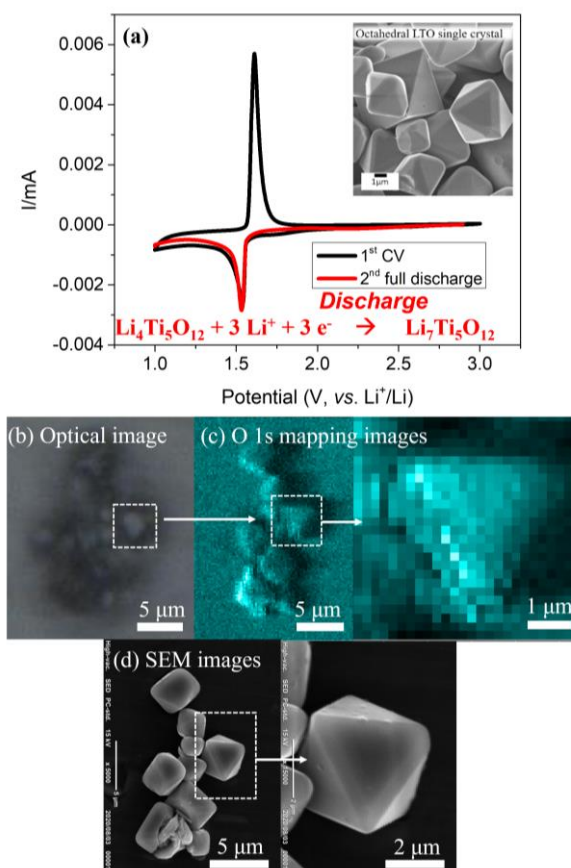


Figure 1 (a) CV (cycling voltammetry) and LSV (linear sweep voltammetry) characteristic of LTO battery cell to 1 V and SEM image of LTO particles. (b) Optical image of LTO particles. (c) O 1s intensity mappings by 3D nanoESCA of LTO. (d) SEM images of LTO after measurement.

ACKNOWLEDGEMENT

This work is partially conducted on the basis of the International joint research program for innovative energy technology by Ministry of Economy, Trade and Industry, Japan.

REFERENCES

- [1] K. Akada, T. Sudayama, D. Asakura, H. Kitaura, N. Nagamura, K. Horiba, M. Oshima, E. Hosono, Y. Harada, Operando measurement of single crystalline $\text{Li}_4\text{Ti}_5\text{O}_{12}$ with octahedral-like morphology by microscopic X-ray photoelectron spectroscopy, *J. Electron Spectrosc. Relat. Phenom.*, 233, 64 (2019).
- [2] K. Horiba, Y. Nakamura, N. Nagamura, S. Toyoda, H. Kumigashira, M. Oshima, K. Amemiya, Y. Senba, H. Ohashi, Scanning photoelectron microscope for nanoscale three-dimensional spatial-resolved electron spectroscopy for chemical analysis, *Rev. Sci. Instrum.* 82, 113701 (2011).

AMBIENT-PRESSURE X-RAY PHOTOELECTRON SPECTROSCOPY STUDIES OF CO₂ HYDROGENATION ON PD-BASED ALLOY

Jiayi Tang

Department of Engineering, University of Hyogo

Introduction

CO₂ hydrogenation to methanol and formic acid has received many attentions because it can efficiently reduce the greenhouse-gas emission as well as synthesize chemicals. In order to further improve the activity, selectivity and stability of catalyst, the origins of catalytic properties, transition metal Pd is an excellent candidate to activate hydrogen molecules, leading to a catalyst surface with highly reduced state, which can facilitate the hydrogenation process. Alloy sites have been considered as the active sites in the CO₂ hydrogenation, such as Pd-based bimetallic catalyst [1]. The study of bimetallic surfaces has gained considerable interest because it is difficult to know the correlations between electronic and chemical properties of the intermixed bimetallic surfaces and the catalytic reaction. In recent, Pd-based alloys were reported as highly reactive catalysts for CO₂ hydrogenation reactions, where ethanol ($2\text{CO}_2 + 6\text{H}_2 \rightarrow \text{C}_2\text{H}_5\text{OH} + 3\text{H}_2\text{O}$) and methanol ($\text{CO}_2 + 3\text{H}_2 \rightarrow \text{CH}_3\text{OH} + \text{H}_2\text{O}$) were produced on the PdCu bimetallic catalysts under different catalytic conditions [2-4]. The formation of formic acid was observed on PdAg alloy nanoparticles through the reaction of CO₂ and H₂ ($\text{CO}_2 + \text{H}_2 \rightarrow \text{HCOOH}$) [5]. In order to clarify the kinetics of CO₂ hydrogenation, the reaction paths were studied on the PdCu(111) single crystal surface using DFT calculations [3]. Since the influences of the surface compositions, structure properties, and gas conditions on the catalytic behavior were required to be studied to improve the efficiency, selectivity and stability of the catalysts, the precise understanding of this reaction is still incomplete with regard to the reaction mechanism under ambient pressure and temperature.

Experimental

In the present study, the CO₂ hydrogenation process over PdCu(fcc), PdCu(B2) and PdAg alloys were studied by *in-situ* ambient-pressure X-ray photoelectron spectroscopy (AP-XPS) to clarify the relationship between the surface electronic properties and the catalytic mechanism. All the high-resolution AP-XPS measurements were performed using the synchrotron radiation at BL07LSU, SPring-8, Japan [6,7]. We carried out the temperature and gas pressure dependent measurements to clearly observe the surface catalytic reactions. The temperature dependence was conducted under H₂ pressure P_{H_2} at 0.4 mbar and CO₂ pressure P_{CO_2} at 1.6 mbar at 300 K, 310 K and 320 K. During the gas pressure dependent measurements, the $P_{\text{H}_2}:P_{\text{CO}_2}$ were performed at 0.4:0.8, 0.4:1.6 and 0.4:2.4, at temperature of 300 K. The time evolutions of C 1s spectra and Pd 3d, Cu 2p, Ag 3d core-level spectra were taken during the CO₂ hydrogenation.

Results and Discussion

C 1s spectra measured before and during the gas exposure at P_{H_2} of 0.4 mbar and P_{CO_2} of 1.6 mbar at 300 K on PdCu(fcc) and PdCu(B2) are shown in Fig.1. C 1s spectrum measured at 8 min after gas exposure (blue solid) obviously shows that three components located at the binding energies of 284.4 eV, 286.1 eV, 287.5 eV are initially formed on the surface, which are assigned to the C⁰, CO species, and intermediate species formate (HCOO), respectively. We found that the amount of the formate gradually increased with the exposure time on both PdCu(fcc) and PdCu(B2). It is newly found that the formate is formed under the relatively low gas pressure at 300 K on the PdCu alloy, which indicates a relatively high reactivity and a low energy barrier for the formate formation compared to the monometallic catalyst surface. Figure 2 shows the time evolutions of C 1s components during the CO₂ hydrogenation at 300

K on PdCu(fcc) and PdCu(B2). We found that the formation of formate on PdCu(fcc) is more active than PdCu(B2), which indicates the surface structure may influence the activity of H₂ dissociation and HCOO formation. Moreover, we observed that the formate was also formed on the PdAg surface and the reaction was strongly influenced by the gas pressure and the temperature. The detailed reaction mechanism and the relationship between the surface electric properties and the reactivity will be further discussed.

REFERENCES

- [1] X. Jiang *et al.*, Appl. Catal. B 170 (2015) 173.
- [2] X. Jang *et al.* Catalysis Communications 118 (2019) 10-14.
- [3] X. Nie *et al.* ACS Catal. 2018, 8, 4873-4892.
- [4] S. Bai *et al.* J. Am. Chem. Soc. 2017, 139, 20.
- [5] K. Mori *et al.* J. Am. Chem. Soc. 2018, 140, 8902.
- [6] S. Yamamoto, *et al.*, J. Synchrotron Rad. 21 (2014) 352.
- [7] T. Koitaya, S. Yamamoto, *et al.*, Topics in Catalysis 59 (2016) 526.

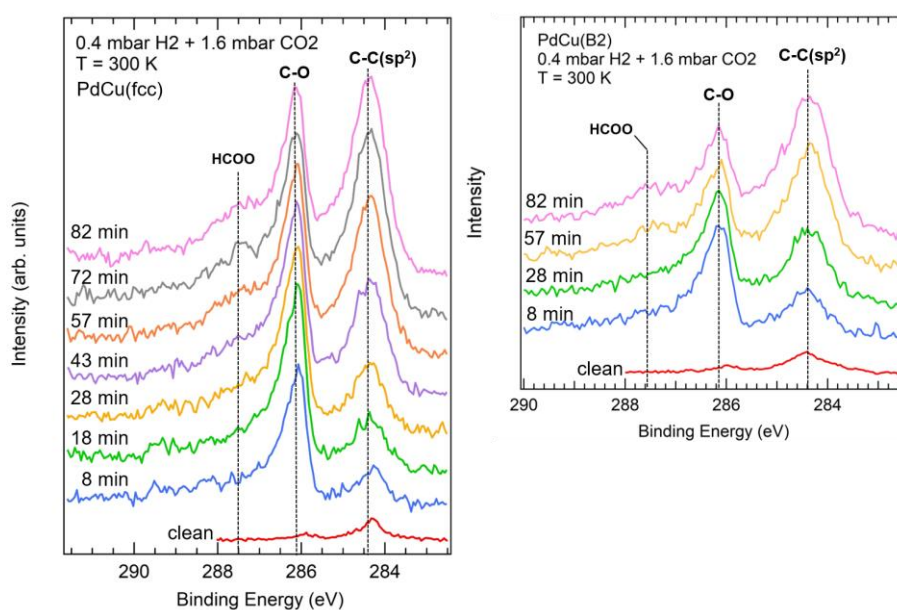


Fig.1 C 1s spectra measured before and during CO₂ hydrogenation on PdCu(fcc) and PdCu(B2) surfaces under H₂ gas pressure of 0.4 mbar and CO₂ gas pressure of 1.6 mbar at 300 K.

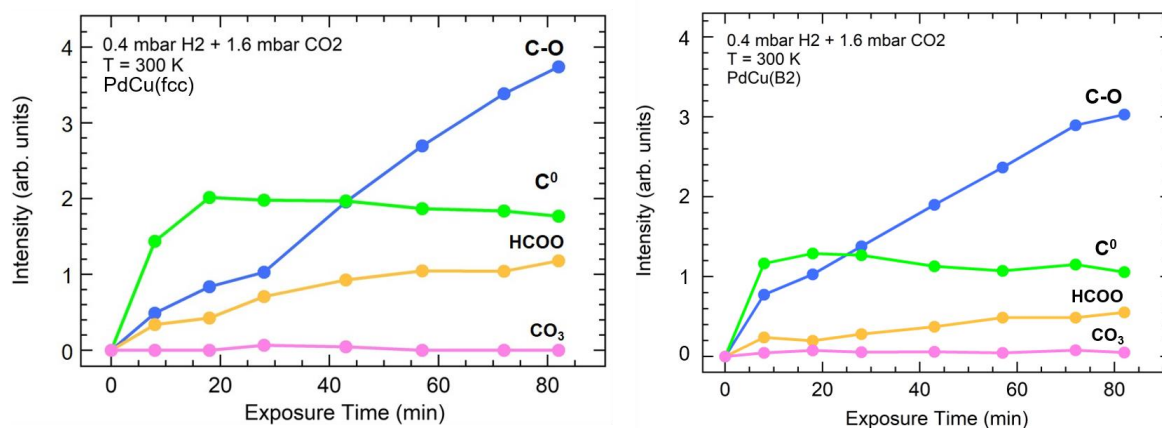


Fig.2 Time evolutions of the components obtained from C 1s spectra on PdCu(fcc) and PdCu(B2) surfaces under 0.4 mbar H₂ and 1.6 mbar CO₂ at 300 K.

INVESTIGATION OF LPSO-STRUCTURE FORMATION MECHANISM BY SMALL ANGLE INELASTIC X-RAY SCATTERING

¹Kakeru Ninomiya, ³Yoshihisa Harada, ^{1,2}Maiko Nishibori

¹Interdisciplinary Graduate School of Engineering Sciences, Kyushu University

²International Center for Synchrotron Radiation Innovation Smart, Tohoku University

³Synchrotron Radiation Laboratory, The Institute for Solid State Physics, The University of Tokyo

INTRODUCTION

Magnesium based ternary alloys which containing a long-period stacking ordered structure (LPSO) has attracted attention because of their excellent mechanical properties and flame retardance[1]. The LPSO phase has a lamellar-like structure consisting of stacked hcp Mg layers with transition metal (TM) and rare-earth (RE) elements rich stacking fault layers[2]. Recent studies have reported that solute-rich layers regularly arrange $TM_6RE_8 L_{12}$ -type clusters[3]. The details of the LPSO structure have been investigated by electron microscopy, but the mechanism of LPSO phase formation is still controversial.

Various types of LPSO structures are reported, which are expressed as 12R-, 10H-, 18R-, 14H- and 24R-types. There are assumed to be constructed of stacking structural blocks with 4-,5-,6-,7- and 8-close packed atomic layers, respectively[4]. However, the mechanism for the appearance of these polytypes and the introduction of periodic stacking faults are not understood. Recently, the appearance of solute nanoclusters before the L_{12} cluster in $Mg_{85}Zn_6Y_9$ alloy was investigated by *in-situ* small-angle X-ray scattering (SAXS) measurement with aging[5]. This suggests that the chemical interaction between solute atoms is essentially important for forming the L_{12} clusters. However, the interaction between TM and RE, in other words, the driving force for cluster formation has not been clarified.

In this study, for the purpose of the formation mechanism of L_{12} cluster, we investigated the relationship between the electronic state of solute atoms and the cluster arrangement by observing the electronic state change of LPSO-Mg alloys with different LPSO structures by X-ray emission spectroscopy (XES).

EXPERIMENTAL METHOD

$Mg_{79}Ni_9Y_{12}$ (at.%) and $Mg_{82}Ni_7Y_{11}$ alloys by high-frequency induction melting of Mg, Ni, and Y pure metals have been prepared. These alloys were kept at 1023 K and cast in an argon atmosphere, and then annealed at 793 K for 100 h.

Small-angle X-ray scattering (SAXS) measurements were conducted to examine the nanoscopic heterogeneous structure (Fig. 1). In $Mg_{82}Ni_7Y_{11}$, a sharp peak and a diffuse peak have appeared at 4.8 nm^{-1} (12.9 \AA) and 6.1 nm^{-1} (10.3 \AA) respectively. These peaks are regarded as a 10H-type LPSO structure. On the other hand, sharp peaks are confirmed at 4.8 nm^{-1} and 5.9 nm^{-1} in $Mg_{79}Ni_9Y_{12}$. These peaks are considered as the scatter corresponding to the interplane distance of 10H and 12R-type LPSO structures. Therefore, $Mg_{82}Ni_7Y_{11}$ consists of the single 10H-type LPSO structure, and $Mg_{79}Ni_9Y_{12}$ contains the 10H- and 12R-type LPSO structure.

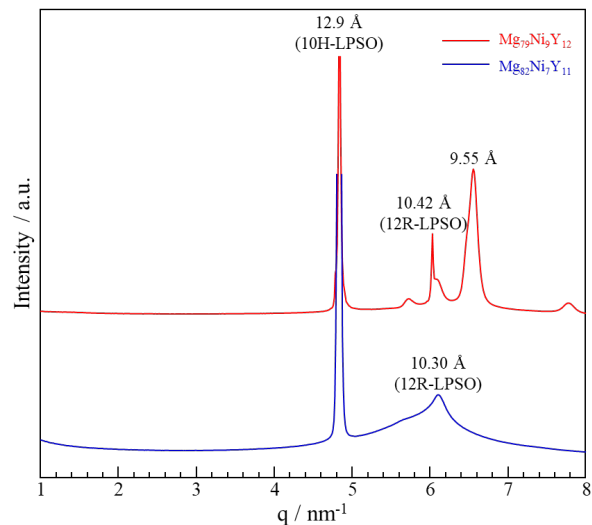


Fig. 1 SAXS profiles of $Mg_{79}Ni_9Y_{12}$ (red line) and $Mg_{82}Ni_7Y_{11}$ (blue line) alloys ($\lambda = 0.92 \text{ \AA}$, camera length = 1129.57 mm)

X-ray absorption/emission spectroscopy (XAS/XES) measurement was performed at BL07LSU in SPring-8. Ni $L_{2,3}$ XAS spectra were obtained by the fluorescence yield method (Fig. 2). We confirmed that the strongest peak of Ni L_3 absorption edge was located at 854 eV and Ni L_2 absorption edge was at 870 eV. Therefore, we used the incident X-ray energy from 854 to 866 eV in 2 eV steps for XES measurement. The total energy resolution for XES was set to $E/\Delta E = 3000$ at the Ni L_3 edge. The diffraction angle was set to 90° and the polarization of incident X-ray energy was vertical.

RESULTS AND DISCUSSION

XES measurement was performed to consider the electronic state changes due to LPSO polytype structures (Fig. 3). XES spectra were the same spectral shapes when the incident X-ray energy was set to 854 eV. On the other hand, the XES spectrum was sharper in $\text{Mg}_{79}\text{Ni}_9\text{Y}_{12}$ than in $\text{Mg}_{82}\text{Ni}_7\text{Y}_{11}$ measured at 866 eV. This result suggests that the electronic state with a deeper energy level changes depending on the LPSO polytype structure, although the electronic state near the Fermi level does not change.

From these results, it was suggested that the electronic state of Ni changes depending on the LPSO structure, that is, the interlayer distance of $L1_2$ cluster. However, the relationship between the cluster ordering and the electronic state of solute atoms has not yet been clarified, and it is necessary to consider structural information and electronic state information at the same time.

Mg-Ni-Y alloy was provided by Prof. M. Yamazaki, Kumamoto University. This work was supported by MEXT/JSPS KAKENHI, Grant-in-Aid for Scientific Research on Innovative Areas, MFS Materials, Grant Numbers JP19H05130.

REFERENCES

- [1] Y. Kawamura, K. Hayashi, A. Inoue, *Mater. Trans.*, **42** (2001) 1172.
- [2] M. Yamasaki, M. Sasaki, M. Nishijima, K. Hiraga, Y. Kawamura, *Acta Mater.*, **55** (2007) 6798.
- [3] D. Egusa, E. Abe, *Acta Mater.*, **60** (2012) 166.
- [4] E. Abe, A. Ono, T. Itoi, M. Yamasaki, Y. Kawamura, *Philos. Mag. Lett.*, **91** (2011) 690.
- [5] H. Okuda, M. Yamasaki, Y. Kawamura, M. Tabuchi, H. Kimizuka, *Sci. Rep.* **5** (2015) 14186.

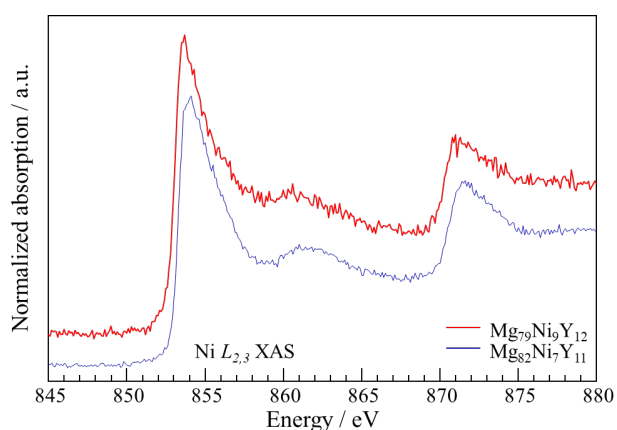


Fig. 2 Ni L_3 XAS spectra of $\text{Mg}_{79}\text{Ni}_9\text{Y}_{12}$ and $\text{Mg}_{82}\text{Ni}_7\text{Y}_{11}$ alloys.

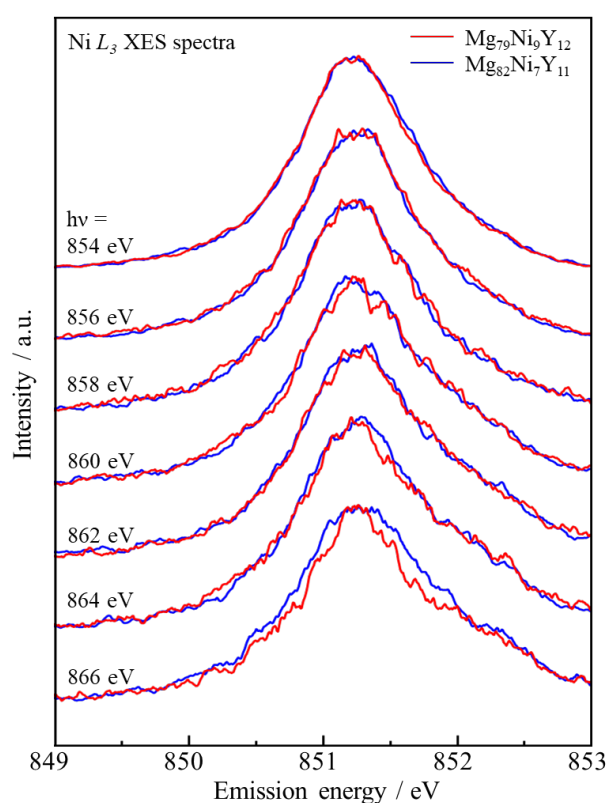


Fig. 3 Ni L_3 XES spectra of $\text{Mg}_{79}\text{Ni}_9\text{Y}_{12}$ and $\text{Mg}_{82}\text{Ni}_7\text{Y}_{11}$ alloys.

EVALUATION OF INTERFACIAL WATER ON ARTIFICIAL POLYMERS BY SOFT X-RAY EMISSION SPECTROSCOPY

Shin-nosuke Nishimura¹, Daiki Murakami^{1,2}, Kosuke Yamazoe³, Naoya Kurahashi³, Tomoya Ueda², Yoshihisa Harada³, Masaru Tanaka^{1,2}

¹*Institute of Materials Chemistry and Engineering, Kyushu University,*

²*Graduate School of Engineering, Kyushu University,*

³*Institute for Solid State Physics, The University of Tokyo*

INTRODUCTION

Recently, significant efforts have been applied toward the design of polymer biomaterials which have central roles in regenerative medicine and tissue engineering application. Water definitely exists on an interface between material and biotissue, of which hydration state essentially affects for biocompatibility. Hydrated water around polymer, as represented by poly(2-methoxyethyl acrylate) (PMEA), is classified into three types, non-freezing water (*NFW*), intermediate water (*IW*), free water (*FW*) in ascending order of the intensity of interaction with polymer chain [1]. Among them, the *IW* has a key role on the affinity of polymer with an organism. However, it has not been clarified what it is in a chemical structure of polymer that works on formation of the *IW*. As the first step to systematize relationship between the *IW* and polymer structure, we evaluated a hydration process on the PMEA brush depending on humidity and succeeded to detect the *IW* by soft x-ray absorption/emission spectroscopy (XAS/XES), whereas origin of the *IW* is still unclear [2, 3]. In this study, we designed and prepared the linear PMEA and linear poly(*n*-butyl acrylate) (*PnBA*) brushes to examine effect of oxygen atom on the side chain for the intermediate water formation (Figure 1). The hydration process on these polymer brushes was evaluated by XES measurement using the same method as our previous reports.

EXPERIMENTAL

We prepared the linear PMEA and *PnBA* brushes on gold-coated SiC substrate by grafting-onto method utilizing sulfur-gold interaction (Figure 1). Thiol-terminated PMEA and *PnBA* at both end was synthesized *via* reversible addition-fragmentation chain transfer (RAFT) polymerization and subsequent aminolysis.

XAS/XES measurement was performed at BL07LSU HORNET station in SPring-8. The humid air with controlled humidity was flowed on the samples to change the water contents in the brush samples

RESULTS AND DISCUSSION

The measured value of the molecular weight for PMEA, $M_{n, SEC}$, agreed closely with the calculated value based on the monomer conversion ($M_{n, theor} = 37,900 \text{ g mol}^{-1}$, $M_{n, SEC} = 40,000 \text{ g mol}^{-1}$), and the dispersity was remarkably narrow ($D = 1.17$). These results suggest that the controlled polymerization of MEA was successful, with the resultant PMEA exhibiting a well-defined structure with narrow dispersity. The thiol-terminated *PnBA* was prepared in a similar fashion using RAFT polymerization. The obtained *PnBA* was characterized following the same procedure as PMEA ($M_{n, theor} = 39,000 \text{ g mol}^{-1}$, $M_{n, SEC} = 38,000 \text{ g mol}^{-1}$, $M_{n, NMR} = 38,000 \text{ g mol}^{-1}$, $D = 1.07$).

Figure 2 plots the O 1s XES profiles of PMEA and *PnBA* at each relative humidity interval. In Figure 2, the 1b₁' and 1b₁'' peaks are the energy positions of bulk water, which was measured

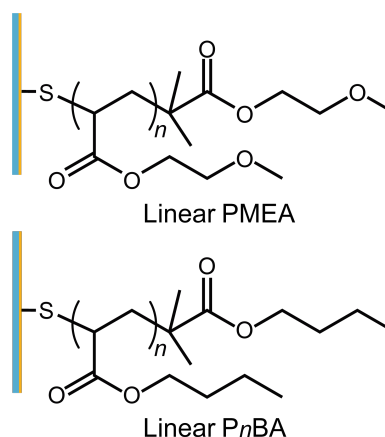


Figure 1. Chemical structure of linear PMEA and *PnBA* brushes used in this study. These polymer brushes were prepared by grafting-onto method.

as a reference. The XES results show that *PnBA* is composed almost exclusively of $1b_1'$ for each of the humidity intervals except 30% RH, indicating that the hydrogen-bonded configuration in *PnBA* is consistent at humidity levels above 30% RH. The profiles are similar in shape to the XES profile reported for water in a charged polymer brush. The hydrogen-bonded structure of water in charged polymer brushes is enhanced by the effect of electric charge or confinement. However, in this study, the hydrogen-bonded structure of water in *PnBA* was enhanced by hydrophobic interactions in the nonionic polymer brushes. Alternatively, *PMEA* consisted of a $1b_1'$ peak and another peak at approximately 527 eV, suggesting that the water in *PMEA* has a different hydrogen-bonded symmetry than the water in *PnBA*. The peak observed at approximately 527 eV corresponds to the peak at approximately 3600 cm^{-1} observed in the infrared (IR) measurements reported by Morita *et al.* [4], who interpreted this component as non-freezing water adsorbed on C=O groups. This is consistent with the interpretation that the component appearing at 527 eV in the XES profile is close to bound water at the material interface.

In this study, we successfully carried out to trace hydration process of the interfacial water onto the linear *PMEA* and *PnBA* brushes by XES measurement with humidity control. State of polymer chain on the outermost of surface might has a great effect on structure of the interfacial water. Although this challenging experiment make it increasingly clear that the origin of *IW* and the relationship of chemical structure with *IW* formation, the knowledge still is not enough to accomplish the ultimate design of biomaterial. Further investigation will be performed in our future work in order to clarify the essential feature of *IW* and the role on biocompatibility.

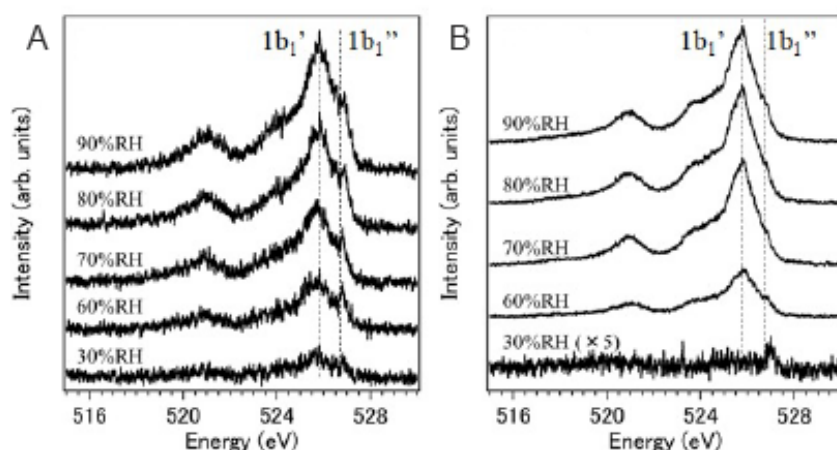


Figure 2. XES spectra of (A) linear *PMEA* and (B) *PnBA* for different humidity conditions. The spectra were normalized by the intensity of the incident soft X-rays and the accumulation time. The spectrum of linear *PnBA* at 30% RH was multiplied by a factor of five.

REFERENCES

- [1] M. Tanaka *et al.*, *Polym. Int.*, **2000**, *49*, 1709-1713.
- [2] D. Murakami *et al.*, *Activity Report of Synchrotron Radiation Laboratory 2018*, **2019**, 68-69.
- [3] D. Murakami *et al.*, *Activity Report of Synchrotron Radiation Laboratory 2018*, **2019**, 70-71.
- [4] S. Morita *et al.*, *Langmuir*, **2007**, *23*, 3750-3761.

MAPPING ANALYSIS OF ACTIVE MATERIALS FOR LITHIUM ION BATTERIES BY 3D NANOESCA

Eiji Hosono^{a,b,c}, Wenxiong Zhang^d, Daisuke Asakura^{b,c}, Naoka Nagamura^e,
Masaharu Oshima^f, Yoshihisa Harada^{c,d,f}

- ^a National Institute of Advanced Industrial Science and Technology (AIST), Global Zero Emission Research Center, 1-1-1 Umezono, Tsukuba, Ibaraki 305-8568, Japan
- ^b National Institute of Advanced Industrial Science and Technology (AIST), Research Institute for Energy Conservation, 1-1-1 Umezono, Tsukuba, Ibaraki 305-8568, Japan
- ^c AIST-UTokyo Advanced Operando-Measurement Technology Open Innovation Laboratory, 5-1-5 Kashiwanoha, Kashiwa, Chiba 277-8565, Japan
- ^d Institute for Solid State Physics (ISSP), The University of Tokyo, 5-1-5 Kashiwanoha, Kashiwa, Chiba 277-8581, Japan
- ^e National Institute for Materials Science, Research Center for Advanced Measurement and Characterization, 1-2-1 Sengen, Tsukuba, Ibaraki 305-0047, Japan
- ^f Synchrotron Radiation Research Organization, The University of Tokyo, 7-3-1 Hongo, Bunkyo-ku, Tokyo, 113-8656, Japan

In order to improve the performance of active electrode materials and to develop innovative electrode materials for lithium-ion batteries (LIBs), we have been investigating the electronic structure change due to redox reaction in various electrode materials during charge-discharge process using soft X-ray absorption spectroscopy (XAS) and soft X-ray emission spectroscopy (XES). The electronic state change by redox reaction is one of the determinants of the energy density, i.e. charge/discharge capacity and operating voltage of the electrode materials. Thus, detailed analysis for understanding of the electronic state under charge-discharge operation is important. In the past few years, position-sensitive electronic structure analysis on the electrode materials has been strongly desired in order to obtain strategies for improving the performance such as surface modification to improve charge-discharge cycle characteristics, controlling the thermophysical stability of active electrode materials, and controlling the crystal axis for the Li diffusion direction.

Soft X-ray microspectroscopy is considered to be one of the suitable methods for spatial analysis of the electrode materials for LIBs because local electronic structures can be analyzed in detail. Soft X-ray microspectroscopy includes photoelectron emission microscopy (PEEM) using electron lenses, scanning transmission soft X-ray microscopy (STXM) using a Fresnel zone plate, and scanning photoelectron spectroscopy (3DnanoESCA)¹. The highest spatial resolution of these techniques is better than 100 nm, which is sufficient to investigate the distribution of electronic and chemical states in electrode materials.

We have developed a microspectroscopic system using synchrotron radiation soft X-rays to obtain soft X-ray photoemission spectroscopy of electrode active materials during operation of all-solid-state LIBs with a spatial resolution of 100-200 nm (“Operando measurement of single crystalline $\text{Li}_4\text{Ti}_5\text{O}_{12}$ with octahedral-like morphology by microscopic X-ray photoelectron spectroscopy”, J. Electron Spectrosc. Relat. Phenom., 233, 64 (2019)², “Microscopic photoelectron analysis for single crystalline LiCoO_2 particles during the charge-discharge in an all solid-state lithium ion battery”, Sci. Rep. 9, 12452 (2019)³).

In this study, we focus on the analysis of each facet in single crystalline active materials for LIBs. Figure 1 shows a SEM image of LiCoO_2 particles and O 1s intensity map on one of the particles. The O 1s XPS map successfully corresponds to the SEM image; the same shape and the same facets are observed. The next step is to analyze the XPS data of each facet of the single crystalline particle. In the near future, we will develop the *operando* measurement

system and conduct the XPS mapping measurement.

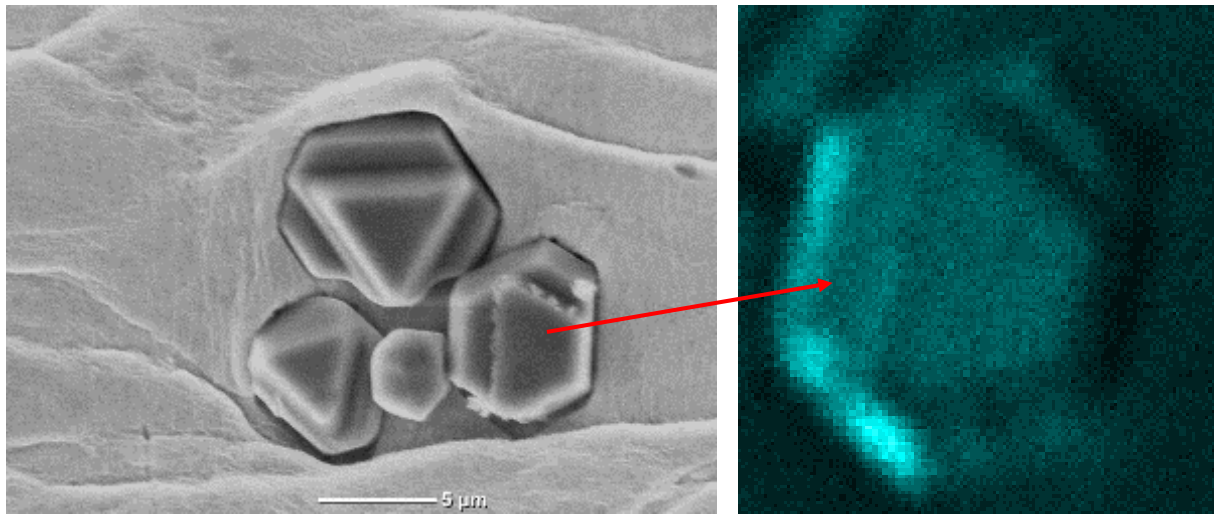


Figure 1. (left) SEM image and (right) O 1s intensity map by 3D nanoESCA of LiCoO₂.

ACKNOWLEDGEMENT

This work is partially conducted on the basis of the International joint research program for innovative energy technology by Ministry of Economy, Trade and Industry, Japan.

REFERENCES

- [1] K. Horiba, Y. Nakamura, N. Nagamura, S. Toyoda, H. Kumigashira, M. Oshima, K. Amemiya, Y. Senba, H. Ohashi, Scanning photoelectron microscope for nanoscale three-dimensional spatial-resolved electron spectroscopy for chemical analysis. *Rev. Sci. Instrum.* 82, 113701 (2011).
- [2] K. Akada, T. Sudayama, D. Asakura, H. Kitaura, N. Nagamura, K. Horiba, M. Oshima, E. Hosono, Y. Harada, “Operando measurement of single crystalline Li₄Ti₅O₁₂ with octahedral-like morphology by microscopic X-ray photoelectron spectroscopy”, *J. Electron Spectrosc. Relat. Phenom.*, 233, 64 (2019).
- [3] K. Akada, T. Sudayama, D. Asakura, H. Kitaura, N. Nagamura, K. Horiba, M. Oshima, E. Hosono, Y. Harada, “Microscopic photoelectron analysis of single crystalline LiCoO₂ particles during the charge-discharge in an all solid-state lithium ion battery”, *Scientific Reports*, 9, 12452 (2019).

Structure-Selective Electronic Structure Analysis by Resonant Inelastic Soft X-ray Diffraction

J. Miyawaki^{1,3}, T. Yachi², S. Maki², K. Kanie² and Y. Harada³

¹*Institute for Advanced Synchrotron Light Source,
National Institutes for Quantum and Radiological Science and Technology*
²*Institute of Multidisciplinary Research for Advanced Materials, Tohoku University*
³*Institute for Solid State Physics, The University of Tokyo*

The fundamental determinants of the physical properties of materials (external field response) are elementary excitations such as phonons, magnons, and crystal field excitations. These elementary excitations are very sensitive to structural changes in materials, suggesting the importance to identify both the structure and these excitations simultaneously. Resonant inelastic X-ray scattering (RIXS) is the most direct method to observe these elementary excitations. Since elastic scattering contains information related to diffraction, RIXS also contains diffraction-derived structural information. Therefore, RIXS originally has the potential to correlate the structural information with the electronic state, i.e., to observe the electronic state in a structure-selective manner.

The fact that elementary excitations can be measured by RIXS can be explained by the energy conservation law, $h\nu_{in} = h\nu_{out} + E_h - E_e$ and the momentum conservation law, $\mathbf{q}_{in} = \mathbf{q}_{out} + \mathbf{k}_h - \mathbf{k}_e + \mathbf{G}$ for the inelastic scattering. Here, $h\nu_{in}(\mathbf{q}_{in})$ and $h\nu_{out}(\mathbf{q}_{out})$ are the energies (momenta) of incident and scattered X-rays, $E_h(\mathbf{k}_h)$ and $E_e(\mathbf{k}_e)$ are the energies (momenta) of holes in the valence band and electrons in the conduction band generated in the final state, and \mathbf{G} is the reciprocal lattice vector of the crystal. In the case of the so-called X-ray diffraction, the elastic scattering is considered, and thus $E_h = E_e$, $\mathbf{k}_h = \mathbf{k}_e$, and $\mathbf{q}_{in} = \mathbf{q}_{out} + \mathbf{G}$, which is the well-known Bragg's law.

When inelastic scattering and diffraction occur simultaneously, both $\mathbf{q}_{in} = \mathbf{q}_{out_inelastic} + \mathbf{k}_h - \mathbf{k}_e + \mathbf{G}$ and $\mathbf{q}_{in} = \mathbf{q}_{out_elastic} + \mathbf{G}$ must be satisfied, leading $\mathbf{q}_{out_inelastic} + \mathbf{k}_h - \mathbf{k}_e = \mathbf{q}_{out_elastic}$ (Fig. 1), and the intensity of the inelastic scattering is expected to be enhanced in a diffractive manner. In the case of nanoparticles, the energy-momentum dispersion of elementary excitations is small and flat, and the momentum conservation law can be satisfied with any combination of \mathbf{k}_h and \mathbf{k}_e . The diffraction from nanoparticles in the soft X-ray region will also show a profile that reflects structural information similar to that of small-angle X-ray scattering (SAXS) in hard X-ray region (although peaks appear in the wide-angle region due to the longer wavelength of soft X-rays). Thus, the diffraction from nanoparticles is expected to enhance the inelastic scattering intensity from nanoparticles of a specific size. This enhancement of the inelastic scattering intensity is an inelastic version of diffraction, and can be called resonant inelastic X-ray diffraction (RIXD). RIXD could be a completely new technique to reveal the electronic state of specific sizes and structures by choosing specific \mathbf{q} , which corresponds selecting the structure by diffraction, and measuring the enhanced intensity of RIXS.

In order to demonstrate the feasibility of RIXD, we have developed the experimental setup of SAXS and RIXD measurement for nanoparticle. As a result, we have succeeded in obtaining SAXS profiles in the soft X-ray region for FePt and Fe₃O₄ nanoparticles for the first time, and have also succeeded in observing the enhancement of inelastic scattering intensity by RIXD in FePt nanoparticles. Figure 2 shows the measured SAXS intensities of FePt and Fe₃O₄ nanoparticles. The incident X-ray energy of 708.1 eV was used in both cases,

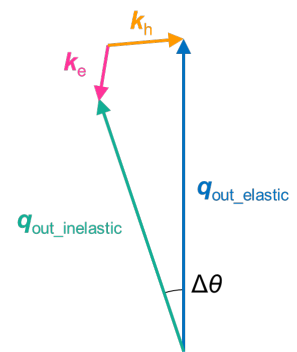


Fig. 1 Schematic of the momentum conservation law in RIXD.

corresponding to the peak top of the L_3 edge, which are assigned to metallic Fe in FePt and mainly to the Fe^{2+} peak in Fe_3O_4 . The obtained profiles are in good agreement with the simulation for the nanoparticles of the particle sizes evaluated by transmission electron microscopy, confirming that the profiles are SAXS from nanoparticles.

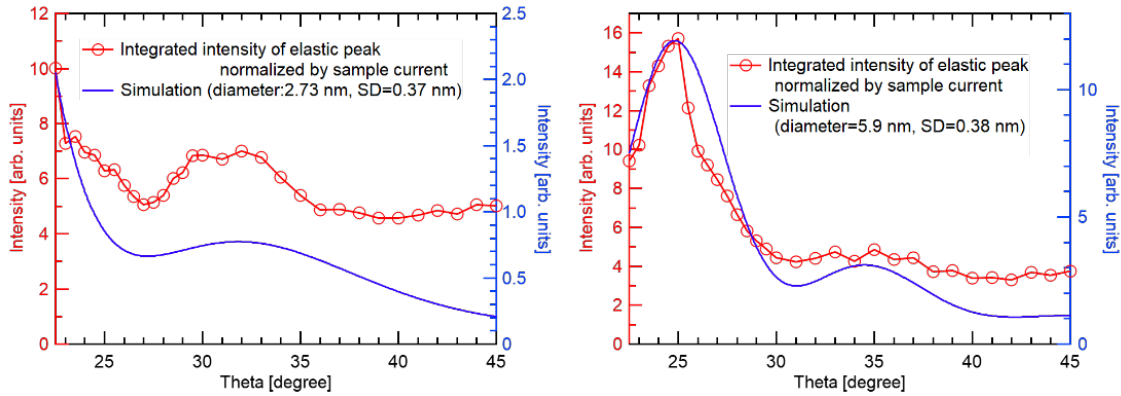


Fig. 2 Experimental (red) and simulated (blue) SAXS profiles of FePt (left) and Fe_3O_4 (right) nanoparticles.

Figure 3 shows the results of RIXD for FePt nanoparticles. In response to the diffraction peak (purple), the intensity of the inelastic scattering, especially in the area of a3, is clearly enhanced (green): RIXD, the diffraction-assisted inelastic scattering, was observed. The absence of the enhancement in the scattering channel closer to the elastic line (the area of a1 or a2) proves that the a3 enhancement does not pick up the enhancement of the elastic tail. On the other hand, in the case of the Fe_3O_4 nanoparticles, although SAXS was clearly observed, RIXD could not be observed. This may be due to the difference in the coherence of the intermediate state of RIXS [1]. Since the intermediate state for insulating Fe_3O_4 is more localized than that for metallic FePt, the diffraction assisted mechanism required for RIXD probably did not work. Although there is still much to be considered, such as the effect of the localized or itinerant intermediate state, the clear intensity enhancement by RIXD was observed in FePt, and we believe that we have succeeded in demonstrating RIXD.

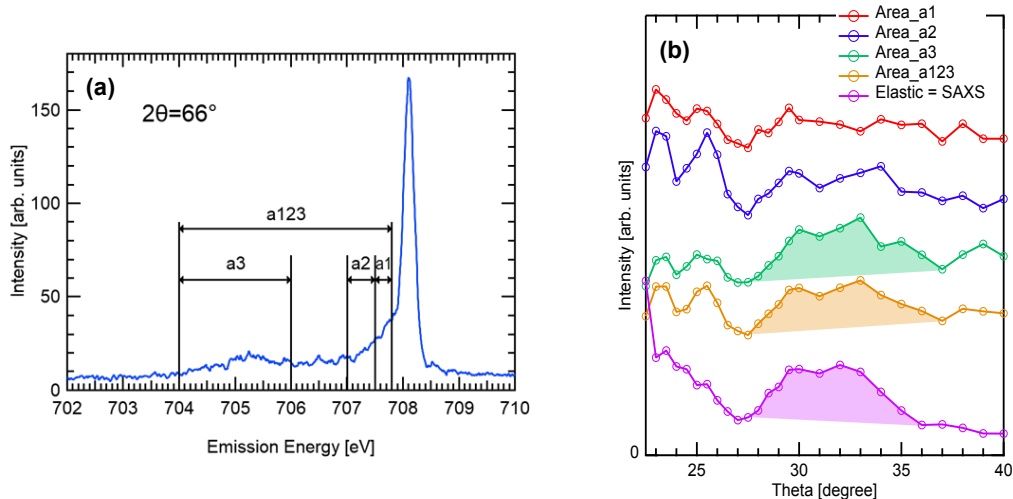


Fig. 3 (a) RIXS spectra of FePt nanoparticle measured at 708.1 eV and $2\theta=66^\circ$. (b) Experimental results of RIXD for FePt nanoparticles. The integration areas are indicated in (a).

REFERENCES

- [1] Y. Ma, Phys. Rev. B **49**, 5799 (1994).

OBSERVATION OF DEHYDRATION PROCESS OF THERMOSENSITIVE POLYMERS BY SOFT X-RAY ABSORPTION AND EMISSION SPECTROSCOPY

Kosuke Yamazoe,^a Ralph John Ugalino,^b Jun Miyawaki,^{a,b,c} Yoshihisa Harada,^{a,b,c}

^a*Institute for Solid State Physics, The University of Tokyo, Kashiwa, Chiba 277-8581, Japan*

^b*Department of Advanced Materials Science, Graduate School of Frontier Sciences, The University of Tokyo, 5-1-5 Kashiwanoha, Kashiwa, Chiba 277-8561, Japan.*

^c*Synchrotron Radiation Research Organization, The University of Tokyo, 7-3-1 Hongo, Bunkyo-ku, Tokyo 113-8656, Japan*

Poly(N-isopropylacrylamide) (PNIPAM) is important for applications in soft functional materials with stimuli-responsive properties. PNIPAM is soluble in cold water but precipitates above the lower critical solution temperature (LCST). LCST is observed at around 32°C [1]. Phase separation beyond LCST is accompanied by a coil-globule transition of the polymer in water, and in many cases the polymer forms aggregates. Water plays an important role in the coil-globule transition of polymers, but it is unclear how dehydration relates to the coil-globule transition and the subsequent formation of mesoscopic polymer-rich aggregates. Studies of PNIPAM have reported on the relationship between cooperative dehydration processes and phase separation [1], estimates of the number of water molecules dehydrated during the coil-globule transition [2], and investigation on the order of which changes first in the phase transition process of PNIPAM, the structural change of water or the structural change of polymer. [3]. Furthermore, the observed structural transformation of water is related to the ripening of aggregates composed of long-chain polymers [3].

Here, we aimed to use soft X-ray absorption spectroscopy (XAS) and soft X-ray emission spectroscopy (XES) to reveal how PNIPAMs dehydrate in the process of collapse to form mesoscopic polymer-rich aggregates. The concentration of the PNIPAM solution used in the experiment is 2.5 wt%. The temperature of the aqueous solution samples was controlled using a variable temperature liquid cell. This is a system using a chiller, where the working fluid is supplied to the liquid cell body. Figure 1 shows the chemical formula of PNIPAM and the schematic illustration of phase transition and dehydration of PNIPAM in water. PNIPAM solution is transparent at lower temperatures than LCST but becomes cloudy at higher temperatures than LCST.

Figure 2(a) shows the temperature dependence of the

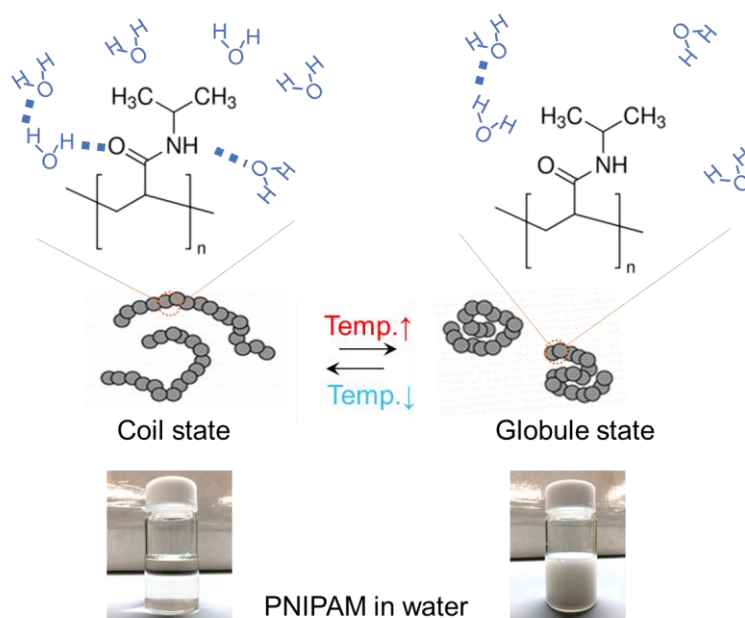


Figure 1. Chemical formula of PNIPAM and schematic diagram of the phase transition and dehydration of the polymer in water. PNIPAM solution is transparent at low temperatures than LCST but becomes cloudy at high temperatures.

the oxygen K-edge XAS spectra of PNIPAM aqueous solution. the peak near 532 eV is the absorption of oxygen at the C=O double bond. For comparison, the XAS spectrum of bulk water measured at room temperature is also plotted. The concentration of the PNIPAM solution used in the experiment is 2.5 wt%. Figure 2(a) shows the temperature dependence of the soft X-ray absorption spectrum of the oxygen K-edge of the PNIPAM aqueous solution. the peak near 532 eV is the absorption of oxygen at the C=O double bond. For comparison, the XAS spectrum of bulk water measured at room temperature is also plotted. As the temperature increases, a peak at 531.5 eV appears, which is in a different position from the peak at 532.4 eV. To assign the C=O double bond, resonant soft X-ray emission spectroscopy was performed. Figure 2(b) shows the temperature dependence of the resonant soft X-ray emission spectra when the excitation X-ray energy is set to 531.5 eV. On the other hand, in the resonant soft X-ray emission spectrum measured at an excitation energy of 532.4 eV, another peak was observed in addition to the above two peaks (Fig. 2(c)). This new peak may be related to hydrogen bonding between water molecules and PNIPAM, suggesting the existence of at least two water-PNIPAM hydrogen-bonded states at temperatures above 32°C LCST. The excitation energy dependence near 532eV at 36°C was also investigated. This result supports that there are mainly two types of hydrogen-bonded states of water and PNIPAM. This result indicates that the process of dehydration was directly observed with increasing temperature. It is expected that theoretical calculations will reveal the detailed hydrogen-bonding states in the future.

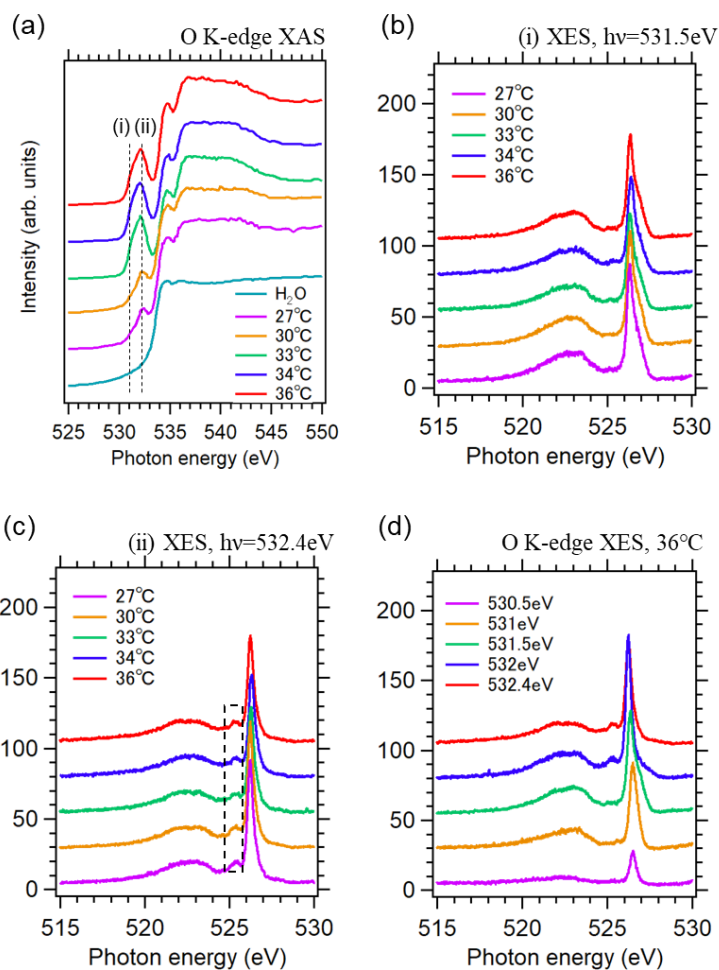


Figure 2. (a) Temperature dependence of XAS spectra of PNIPAM aqueous solution. (b) Temperature dependence of the resonant XES spectra at $h\nu=531.5\text{eV}$. (c) Temperature dependence of the resonant XES spectra at $h\nu=532.4\text{eV}$. (d) The excitation energy dependence of XES near 532eV at 36°C.

REFERENCES

- [1] M. Philipp *et al.* *J. Phys. Chem. B* **118** 4253 (2014).
- [2] Y. Ono and T. Shikata. *J. Am. Chem. Soc.* **128** 10030 (2006).
- [3] K. Mochizuki and D. Ben-Amotz. *J. Phys. Chem. Lett.* **8** 1360 (2017).

Upgrade of ambient pressure X-ray photoelectron spectroscopy system at SPring-8 BL07LSU

Susumu Yamamoto^{1,2}, Takanori Koitaya^{3,4}, Iwao Matsuda⁵, and Jun Yoshinobu⁵

¹ *International Center for Synchrotron Radiation Innovation Smart (SRIS), Tohoku University*

² *Institute of Multidisciplinary Research for Advanced Materials (IMRAM),
Tohoku University*

³ *Department of Materials Molecular Science, Institute for Molecular Science*

⁴ *Precursory Research for Embryonic Science and Technology (PRESTO), Japan Science and
Technology Agency (JST)*

⁵ *The Institute for Solid State Physics, The University of Tokyo*

Introduction

Operando spectroscopy is an experimental technique that directly observes materials and devices under actual operation conditions to find a correlation between structure and function in materials. This experimental approach is especially important in energy conversion materials such as catalysts, photocatalysts, fuel cells, and lithium-ion batteries, because the surface structure and composition of these materials is often changed under reaction conditions.

Operando X-ray spectroscopy has been limited to the hard X-ray region, but *Operando* spectroscopy in the soft X-ray region has rapidly developed in recent years with use of high-brilliance synchrotron radiation light source and the development of new instruments. We have developed ambient pressure X-ray photoelectron spectroscopy (AP-XPS) system [1] at the high-brilliance soft X-ray beamline BL07LSU of SPring-8, and have been promoting research on *operando* observation of catalytic reactions [2-9] over the last seven years. The limitations of the AP-XPS system were revealed by the past experiments: (i) low maximum gas pressure, and ii) low temporal resolution. As for i) low maximum gas pressure, the maximum gas pressure in the AP-XPS measurements is limited to about 20 mbar for bulk samples. The low maximum gas pressure leads to low reactivity and selectivity in catalytic reactions and small amount of water on the surface of polymers and semiconductor photoelectrodes. Regarding ii) low temporal resolution, the temporal resolution of the present AP-XPS system is limited to sec~min.

Therefore, in our long-term project, we set two goals to upgrade the AP-XPS system at SPring-8 BL07LSU: (i) the increase of the maximum gas pressure, and (ii) the development of picosecond time-resolved AP-XPS system. In this report, we describe our recent efforts to achieve (i) the increase of the maximum gas pressure.

Results and discussion

The XPS signal attenuation in a gas phase is proportional to $\exp(-z\sigma p)$, where z is the distance between the sample and the entrance nozzle of an electron spectrometer, σ scattering cross section of photoelectrons, p gas pressure. In order to mitigate the XPS signal attenuation, one effective approach is to keep z small. When the distance z is small, however, the local gas pressure on the sample surface is decreased due to the differential pumping through the entrance nozzle. To avoid the decrease of local gas pressure, the opening of the entrance nozzle needs to be decreased.

In the present AP-XPS system, the diameter of the nozzle opening was 300 μm , and the distance z was set at ~ 300 μm . We developed a new nozzle with the opening diameter of 50 μm (**Figure 1**). The nozzle body was manufactured by an electroforming technique at Institute for Molecular Science. The opening hole was made by a focused ion beam. The distance z was set at ~ 100 μm . Using the new 50 μm nozzle, we have succeeded in measuring Au4f XPS spectra in the presence of 100 mbar N_2 gas. Therefore, the maximum gas pressure of the AP-XPS system was improved from 20 mbar to 100 mbar. Now we start to measure various systems which require high gas pressures; H_2 absorption process in Pd alloys and CO_2 hydrogenation reactions on catalyst surfaces.

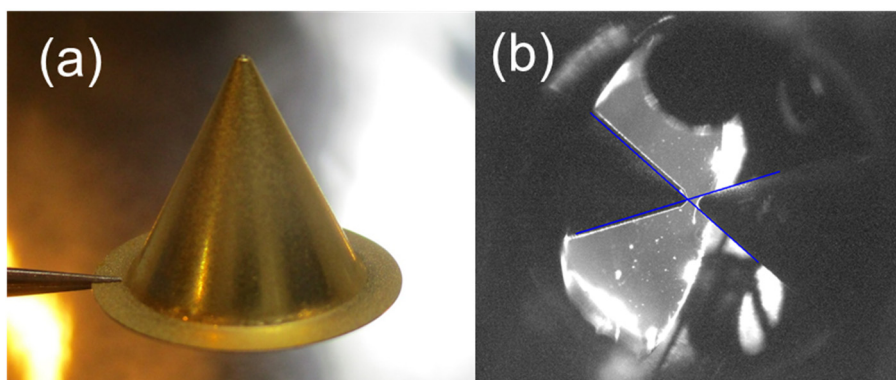


Figure 1. New entrance nozzle of an electron spectrometer for AP-XPS system at SPring-8 BL07LSU. (a) Overview picture of the nozzle (50 μm opening at the apex of nozzle), (b) a sample approaches to the nozzle and the distance between the sample and the nozzle was about 100 μm .

REFERENCES

- [1] S. Yamamoto *et al.*, *J. Phys.: Condens. Matter* **20**, 184025 (2008).
- [2] T. Koitaya, S. Yamamoto *et al.*, *Topics in Catalysis* **59**, 526-531 (2016).
- [3] S. Yamamoto *et al.*, *Phys. Chem. Chem. Phys.* **20**, 19532-19538 (2018).
- [4] J. Tang, S. Yamamoto *et al.*, *Appl. Surf. Sci.* **463**, 1161-1167 (2019).
- [5] J. Tang, S. Yamamoto *et al.*, *Appl. Surf. Sci.* **480**, 419-426 (2019).
- [6] T. Koitaya, S. Yamamoto *et al.*, *ACS Catalysis* **9**, 4539-4550 (2019).
- [7] T. Koitaya, S. Yamamoto *et al.*, *e-J. Surf. Sci. Nanotechnol.* **17**, 169-178 (2019).
- [8] M. Sato, S. Yamamoto *et al.*, *J. Phys. Chem. C* **124**, 12466-12475 (2020).
- [9] Y. Imazeki *et al.*, *J. Phys. Chem. C* **125**, 9011-9019 (2021).

Electronic structure of van der Waals magnetic semimetal GdGaI

Kohei Yamagami, Ryotaro Okuma, Yoshinari Okada

Okinawa Institute of Science and Technology Graduate University, Tancha, Onna-son, Kunigami-gun
Okinawa, 904-0495, Japan.

Recently, we have succeeded to grow relatively large size van der Waals (vdW) magnetic semimetal GdGaI (GGI). The crystal structure and picture of GdGaI is shown in **Fig. 1a**. The density functional theory (DFT) based band calculation for GGI suggests semi-metallic electronic structure. The DFT band structure is analogous to that of TiSe₂, which is known as a 2D material hosting charge density wave (CDW) and/or exciton formation [1]. Compared to non-magnetic TiSe₂, emergence of weak ferromagnetism at low temperature is an interesting unique characteristic in GGI. While rich deformation of band structure is naturally expected, experimental report on electronic structure in GGI has been lacking so far.

Here, we report angle resolved photoemission spectroscopy (ARPES) on GGI. **Fig. 1b** shows ARPES dispersion around Γ point, using 7 eV laser with p-polarization [2]. For comparison, ARPES dispersion using He discharge lamp is also shown in **Fig. 1c**. Below $E-E_F=-0.4$ (eV), two bands are clearly visualized in laser ARPES data (**Fig. 1b**). Above $E-E_F=-0.4$ (eV), the hole bands around the Γ point were similarly observed in both cases. The band top of the hole band is around $E-E_F\sim-0.18$ (eV), which reflects band gap opening by $2a \times 2a$ ordering. The clear difference between two ARPES dispersion (**Fig. 1b and c**) is near E_F intensity distribution in k space. This presumably suggests the importance of understanding characteristic spin and orbital nature in near E_F hole band, together with prominent spin-orbital coupling effect in this system.

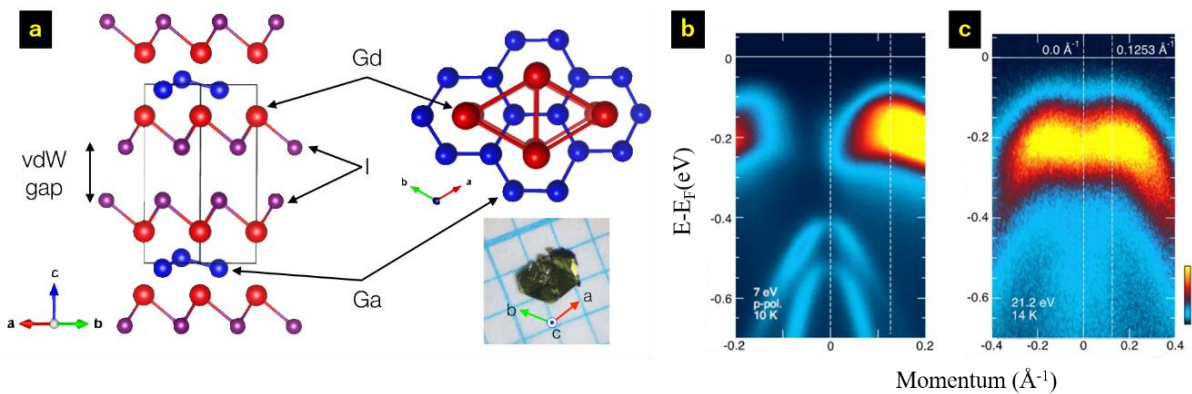


Figure 1. (a) The crystal structure and picture of GdGaI. (b)(c) The angle resolved photoemission spectroscopy (ARPES) data around Γ point, using (b) He discharge lamp and (c) 7 eV laser. The measured temperature for (b) and (c) are 10K and 14K, respectively. In (b), p-polarization is used.

References

- [1] H. Cercellier, *et al.* Phys. Rev. Lett. **99**, 146403 (2007).
- [2] K. Yaji *et al.*, Rev. Sci. Instrum. **87**, 053111 (2016).

ENHANCEMENT OF RASHBA SPLITTING IN SNPC/AU(111)

Kaname Kanai

Department of Physics, Faculty of Science and Technology, Tokyo University of Science

The growth of sub-monolayers of tin phthalocyanine (SnPc) molecules on Au(111) has been confirmed by angle-resolved photoemission spectroscopy (ARPES) to enhance the energy band splitting due to the Rashba spin-orbit interaction appearing in the Shockley state (SS). This result provides knowledge for understanding the electronic structure of Rashba-type SS at the interface between organic molecules and metal substrates.

The electronic structure of the interface between a metal surface and molecules adsorbed on that surface has been a long-standing issue in surface science. Recently, this issue has attracted more attention due to its importance in organic semiconductor devices. The electronic structure of an interface at an electrode metal surface covered with organic semiconductor molecules (organic/metal interface) is directly responsible for the electronic properties of the device because the relationship between the molecular orbital energies and the Fermi level of the metal at the interface determines the carrier injection barrier from the electrodes into the semiconducting layers. Thus, in order to realize a device with high carrier injection efficiency, it is vital to understand the formation of the electronic structure at the organic/metal interface.

SS is a characteristic electronic state peculiar to the crystal surface. By breaking the spatial inversion symmetry of the crystal in the normal direction to the surface, a free electron-like parabolic dispersion appears near the surface. In particular, it is known that in noble metal crystals such as copper, silver, and gold, large spin-orbit coupling can cause Rashba effects of practically observable magnitude to appear. The Rashba effect lifts the spin degeneracy of the SS band dispersion and splits it into two parabolas that are completely spin-polarized except at the Γ point. Recently, it has been reported that this Rashba effect is enhanced at metal interfaces such as Bi/Ag(111) [1], TTC/Au(111) [2], and rare gas atoms/Au(111) interfaces. Attempts have also been made to create devices that can convert spin currents to spin currents by generating the Edelstein effect at the molecule/metal interface using the giant Rashba effect [3,4]. Therefore, understanding the mechanism by which molecular adsorption significantly affects the Rashba effect is not only of interest in surface science, but should provide fundamental information for future spintronics. In this study, we aimed to directly observe in detail the influence of tin-phthalocyanine (SnPc) molecules, a typical organic semiconductor molecule, on the Rashba effect that appears in SS of Au(111).

The single crystal of Au(111) sample was used for the substrate. Before vapor deposition of SnPc on it, the surface of this Au(111) substrate was cleaned in UHV by sputter-anneal cycles. Anneal temperature was 773 K. This clean surface was evaluated by low energy electron diffraction (LEED) measurement. After outgassing, SnPc was deposited on Au(111) at normal incidence from resistively heated Knudsen cell. The deposition rate of 0.0005 ~ 0.002 nm/s was measured with a quartz crystal microbalance oscillator. The deposition of SnPc on Au(111) was carried out in a stepwise manner: the SnPc film thickness were 0.06, 0.13, 0.19, and 0.26 ML. The electronic structure of SnPc/Au(111) was measured by ARPES at 28 K.

When SnPc thin film is grown on Au(111), the SS rapidly disappears as the coverage increases. This is probably due to the loss of translational symmetry in the direction parallel to the surface, caused by the random orientation of the molecules on the surface. This hypothesis can be easily inferred from the three-dimensional molecular structure of SnPc, which is called “shuttlecock” as shown in Fig. 1. However, when the coverage of the grown SnPc thin film is very low, SnPc appears to grow epitaxially on Au(111), and

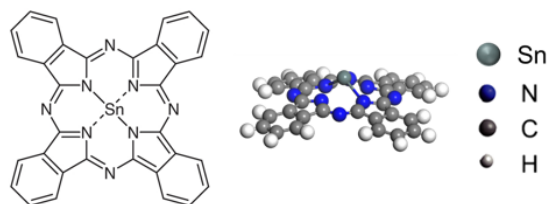


Fig. 1. Molecular structure of SnPc (left). Three-dimensional structure of SnPc (right).

the Au(111) SS does not disappear. Furthermore, it was observed that the Au(111) SS was greatly affected by molecular adsorption.

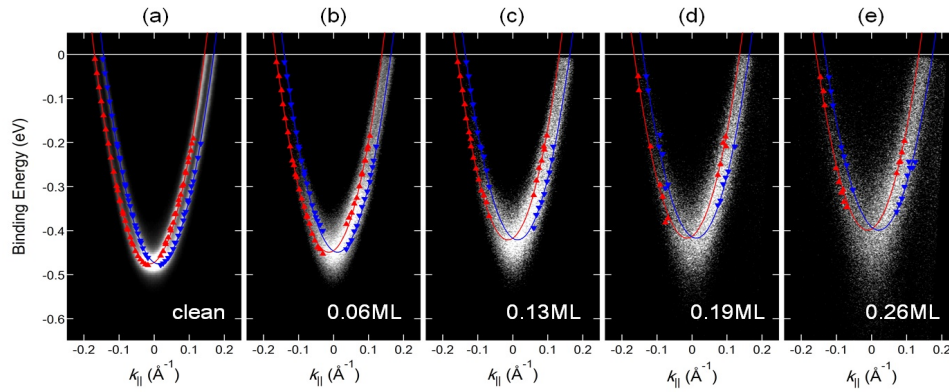


Fig. 2. The thickness dependence of SnPc/Au(111) Rashba-type SS measured at 28 K using ARPES. The results of (a) Au(111) clean surface, (b) SnPc 0.06ML/Au(111), (c) SnPc 0.13ML/Au(111), (d) SnPc 0.26ML/Au(111), and (e) SnPc 0.32ML/Au(111). The red or blue plots on the data are the results of peak fitting analysis at EDC (Energy Distribution Curve) and MDC (Momentum Distribution Curve) maps.

Fig. 2 shows the ARPES spectra ($h\nu = 6.998$ eV) of SnPc/Au(111). It can be seen that SS in Au(111) is modified as the coverage of SnPc increases. Energy of SS in Au(111) was significantly lowered with increasing the PbPc thickness. However, SS was observable only in the case of very low coverage of SnPc, and SS disappeared before the coverage of one molecular layer was reached.

Fig. 3 shows thickness dependence of Rashba parameter α_R and Rashba splitting Δk_{\parallel} calculated by EDC and MDC analysis of the ARPES results in Fig. 2. As the value of Δk_{\parallel} increased, the value of α_R also tended to increase as the film thickness increased.

In conclusion, we observed the enhancement of Rashba effect by adsorption SnPc thin film on Au(111). One possible factor that enhances the Rashba effect at the SnPc/Au (111) interface is due to the potential gradient caused by the adsorption of molecules with evenly aligned dipole directions, which is needed to be further verified in the future. The results presented here allowed us to discuss the interfacial electronic states formed by adsorbed metallic phthalocyanines, in relation to their effect on the Rashba effect.

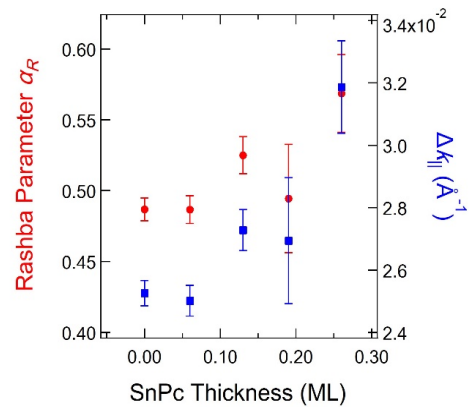


Fig. 3. Thickness dependence of Rashba parameter α_R and Δk_{\parallel} calculated from SnPc/Au(111) Rashba-type SS observed by ARPES.

REFERENCES

- [1] C. R. Ast, J. Henk, A. Ernst, L. Moreschini, M. C. Falub, D. Pacilé, P. Bruno, K. Kern and M. Grioni, *Phys. Rev. Lett.* **98**, 186807 (2007).
- [2] H. Mizushima, H. Koike, K. Kuroda, Y. Ishida, M. Nakayama, K. Mase, T. Kondo, S. Shin and K. Kanai, *Phys. Chem. Chem. Phys.*, **19**, 18646 (2017).
- [3] S. Takizawa, K. Kondou, H. Isshiki, K. Shimose, T. Kawabe, S. Miwa and Y. Otani, *IEEE Trans. Magn.*, **54**, 11 (2018).
- [4] H. Isshiki, K. Kondou, S. Takizawa, K. Shimose, T. Kawabe, E. Minamitani, N. Yamaguchi, F. Ishii, A. Shiotari, Y. Sugimoto, S. Miwa and Y. Otani, *Nano Lett.*, **19**, 7119 (2019).

SARPES STUDY OF A NEW WEYL SEMIMETAL OF THE CDW COMPOUNDS

Chun Lin¹, Kenta Kuroda¹, Ryo Noguchi¹, Kaishu Kawaguchi¹, Ayumi Harasawa¹, Shik Shin², Masanobu Miyata³, Koyano Mikio³, and Takeshi Kondo^{1,4}

¹*The Institute for Solid State Physics, The University of Tokyo*

²*Office of University Professor, The University of Tokyo*

³*School of Materials Science, Japan Advanced Institute of Science and Technology*

⁴*Trans-scale Quantum Science Institute, The University of Tokyo*

The emergent quantum phenomena in low dimensional materials have attracted increasingly more attention in the realm of not only fundamental science but also practical applications. These compounds typically host multiple broken symmetry orders such as charge density wave (CDW), superconductivity, and other magnetism- and spin-related exotic quantum phenomena [1], providing a multifunctional platform for investigations of basic physics and real-world applications owing to their low dimensionality suitable for engineering. On the other hand, topological semimetal is a new class of quantum matters with characteristic topological surface states originated from the topology of their bulk band structure [2]. In particular, the Weyl semimetal is a condensed-matter realization of Weyl fermions manifested as low-energy excitations, in which band dispersions exhibit linear crossings at pairs of Weyl points, with either broken spatial inversion or time-reversal symmetry.

Ta₂Se₈I is well known as a prototypical quasi-one-dimension (quasi-1D) CDW system stacked by TaSe₄ chains along the *c* axis with body center tetragonal lattice (Figs. 1a,b). The CDW sets in at a temperature around 260 K revealed by resistivity [3] as shown in Fig. 1d [4]. The CDW wave vector was confirmed by X-ray diffraction to be (± 0.045 $2\pi/a$, ± 0.045 $2\pi/b$, ± 0.085 $2\pi/c$) [5]. Nevertheless, a long-standing puzzle remains in that the energy gap is much larger than the mean-field value and it refrains from closing at temperatures far above the CDW onset, as confirmed by, e.g., optical spectra [6] and angle-resolved photoemission spectroscopy (ARPES) [7,8]. Such an anomalous behavior was attributed either to a fluctuating CDW in an extreme 1D manifestation [6] or the formation of small polarons dressing mobile electrons owing to strong electron-phonon coupling [7,8]. Recently, first principle calculations indicate that the high-temperature phase of this compound is actually a Weyl semimetal [9], from which the transport signals of chiral anomaly have been successfully captured in the CDW state [4]. Ta₂Se₈I, therefore, offers a very rare realization of strong correlation driven topological phase transition [9].

Here, we present laser-based spin-resolved ARPES (at Institute for Solid State Physics, the University of Tokyo) results in the distorted phase of this newly predicted Weyl semimetal and provide evidence of spin-polarized Weyl cone whose experimental observation remains challenging in the literature.

Figure 1g shows the constant-energy contour map at a binding energy of 0.6 eV acquired at 100 K with 7 eV laser and on the (110) surface of conventional cell which is easily cleaved due to the weak van der Waals interactions among quasi-1D chains. The bulk Brillouin zone and its surface projection (reddish shaded) are shown in Fig. 1c. One can see that the band structure features a wiggle perpendicular to the chain direction indicative of a finite interchain interaction, which is consistent with synchrotron-ARPES [7,8]. In Figs. 1h,i, we present the dispersions along two momentum cuts crossing the Weyl points, as indicated in Fig. 1g with corresponding colored arrows. A spectral suppression manifested as a 0.2 eV energy gap agrees with the polaron scenario [7]. Below this polaron gap, the band disperses in a linear Dirac-like manner as indicated by the red lines in Figs. 1h,i, consistent with the proposed

electronic structure of a Weyl semimetal (Fig. 1e [9]). Taking advantage of spin resolution, we obtained the energy distribution curves of spin-up and spin-down states at a momentum point of the (purple arrow in Fig. 1i), as shown in Fig. 1j. The resulting spin polarization (green curve in Fig. 1j) suggests a spin-polarized Weyl cone in the CDW state.

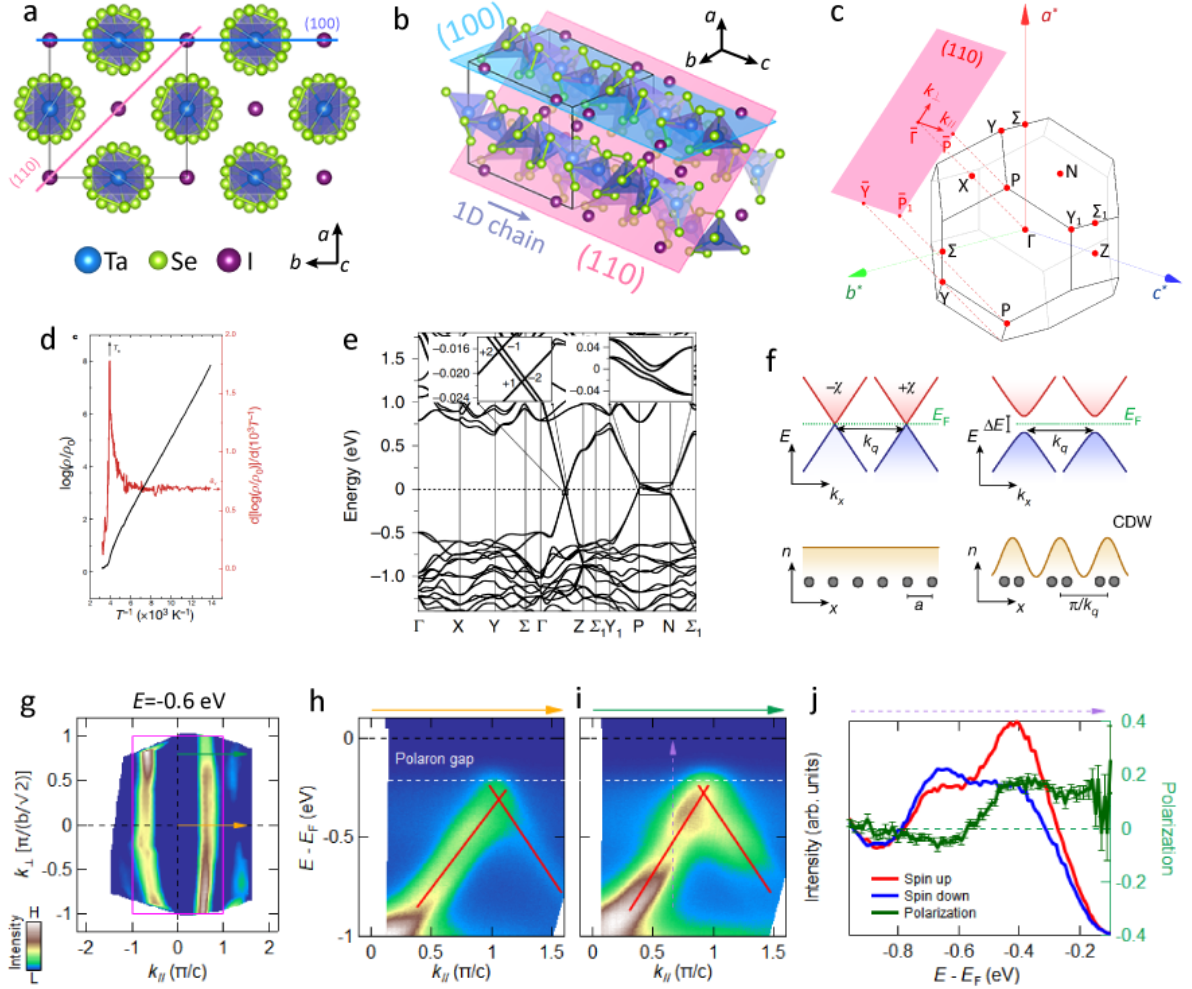


Fig. 1 **a,b**, Crystal structure of $\text{Ta}_2\text{Se}_3\text{I}$. **c**, Bulk Brillouin zone and its projection onto conventional (110) surface. **d**, Characteristic resistivity showing a CDW transition around 260 K [4]. **e**, Band structure along high-symmetry lines calculated from density functional theory with spin-orbit coupling [9]. **f**, Schematic of a CDW gapped Weyl semimetal [4]. **g-i**, Our preliminary data of constant-energy contour ($E_B = 0.6$ eV) and band dispersions along two momentum cuts indicated by the corresponding colors. Small polarons dress photoelectrons featured by a polaron gap as indicated. Red lines in **h,i** are guides for the eyes. **j**, Our preliminary data of spin-resolved energy distribution curves and spin polarization along the dashed purple arrow indicated in **i**.

REFERENCES

- [1] P. Monceau, *Advances in Physics* **61**, 325 (2012)
- [2] N. P. Armitage *et al.*, *Rev. Mod. Phys.* **90**, 015001 (2018)
- [3] Z. Z. Wang *et al.*, *Solid State Commun.* **46**, 325–328 (1983)
- [4] J. Gooth *et al.*, *Nature* **575**, 315–319 (2019)
- [5] H. Fujishita *et al.*, *Solid State Commun.* **49**, 313–316 (1984)
- [6] H. P. Geserich *et al.*, *Physica B+C* **143**, 198–200 (1986)
- [7] L. Perfetti *et al.*, *Phys. Rev. Lett.* **87**, 216404 (2001)
- [8] C. Tournier-Colletta *et al.*, *Phys. Rev. Lett.* **110**, 236401 (2013)
- [9] W. Shi *et al.*, *Nature Physics* **17**, 381–387 (2021)

OBSERVATION AND CONTROL OF THE WEAK TOPOLOGICAL INSULATOR STATE IN ZRTE₅

Peng Zhang¹, Ryo Noguchi¹, Kenta Kuroda¹, Chun Lin¹, Kaishu Kawaguchi¹, Koichiro Yaji², Ayumi Harasawa¹, Mikk Lippmaa¹, Simin Nie³, Hongming Weng⁴, V. Kandyba⁵, A. Giampietri⁵, A. Barinov⁵, Qiang Li⁶, G. D. Gu⁶, Shik Shin¹, Takeshi Kondo¹

¹*Institute for Solid State Physics, University of Tokyo*

²*Research Center for Advanced Measurement and Characterization, NIMS*

³*Department of Materials Science and Engineering, Stanford University*

⁴*Institute of Physics, Chinese Academy of Sciences*

⁵*Elettra - Sincrotrone Trieste*

⁶*Condensed Matter Physics and Materials Science Department, Brookhaven National Laboratory*

A quantum spin Hall insulator hosts topologically protected edge states, in which backscattering by nonmagnetic impurities is prohibited and dissipationless current is possible. Its 3D analogue, a weak topological insulator (WTI), possesses surface states at the ‘side’ surface that are not weak, but as robust as the wide-studied strong topological insulators, and there may be even less scattering channels due to the highly directional surface electrons [1]. However, since the topological states only appear on side surfaces, it is difficult to prepare such a clean surface and to study the WTI states. Here, we report for the first time the visualization of the topological surface states of the WTI candidate ZrTe₅. A quasi-1D spin-momentum locked band on the side surface was distinguished. Furthermore, control of the band gap by external strain was confirmed directly by ARPES: a WTI state with a larger gap and a topological phase transition to an ideal Dirac semimetal state are realized.

Topological surface states observed on the side surface

ZrTe₅ was predicted to be a WTI candidate at the early stage of exploring WTIs [2], in which there is no surface state on the top surface, while on the side surface there is topological surface state, as shown in Fig. 1(a). It has a quasi-1D crystal structure. Along the lattice *b* direction, the layers are stacked by van der Waals forces, and a clean surface can be easily obtained by cleavage. Instead, Te–Te bonding exists between adjacent layers along the lattice *c* direction, causing much more difficulty in cleaving the side *a*-*b* surface. Due to the difficulty to cleave the side surface, all the previous surface-sensitive studies were carried out

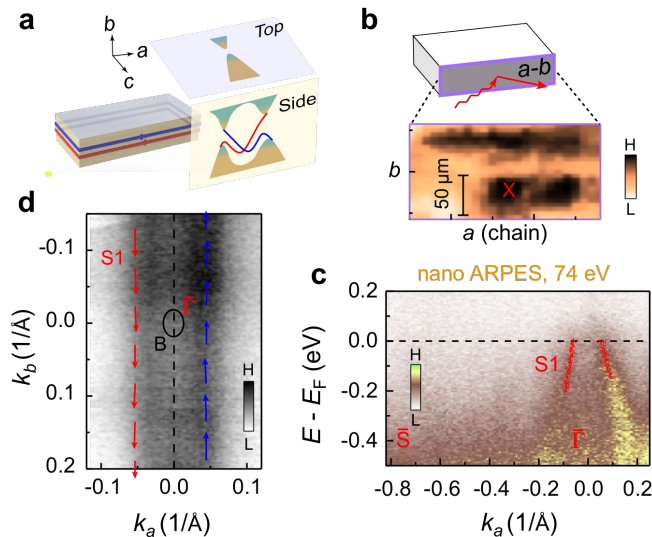


Figure 1 ARPES measurement on the side surface of ZrTe₅. (a) Band structure of a WTI on the top surface and side surface. (b) Intensity mapping in the real space for the cleaved area of the side surface from a nano-ARPES. (c) Band structure measured at the position indicated by red cross in (b). (d) Fermi surface measured with laser ARPES. The red and blue arrows indicated the spin direction measured with a spin-resolved ARPES.

on the top surface. Whether or not this material is topological, which relies on the measurement from side surface, has not been determined beyond speculation. We successfully prepared the side surface of this sample [3]. With a synchrotron-based nano-ARPES (spot size $< 1 \mu\text{m}$), we took real space maps of photoemission intensity on several samples, as sketched in Fig. 1(b). It is found that the typical dimension of cleaved areas is around or smaller than $50 \mu\text{m}$. Along lattice a direction, the band shows a hole-like dispersion (Fig. 1(c)). In k -space, a quasi-1D Fermi surface is exhibited by plotting ARPES intensities about the Fermi level, which shows no dispersion along lattice b direction (Fig. 1(d)). We further observed a clear spin polarization along lattice b direction. In contrast, the spin polarization is almost zero along the lattice a and c directions, as sketched by red and blue arrows in Fig. 1(d). Therefore, the band is spin-polarized along the b -direction with spin-momentum locking, consistent with the spin-texture of WTIs with a quasi-1D dispersion.

Strain-tuned topological phase transition observed on the top surface

First-principles calculations predict that ZrTe_5 is close to a topological phase transition, which may be tuned by external strain. We used a strain device shown in Fig. 2(a) to apply both compressive and tensile strain. On the top surface, without strain we observed a small bulk gap ($\sim 28 \text{ meV}$), as shown in the middle panel of Fig. 2(b). The small bulk gap indicates that the WTI state in ZrTe_5 is protected only marginally from external perturbations. With tensile strain, the band gap is enlarged to $\sim 51 \text{ meV}$. In contrast, we could reduce the band gap by compressive strain, even realizing a Dirac semimetal state with no band gap. The corresponding first-principles calculations are displayed in Fig. 2(c), which is consistent with the experimental results. In Fig. 2(d), we summarized the topological phase diagram of ZrTe_5 .

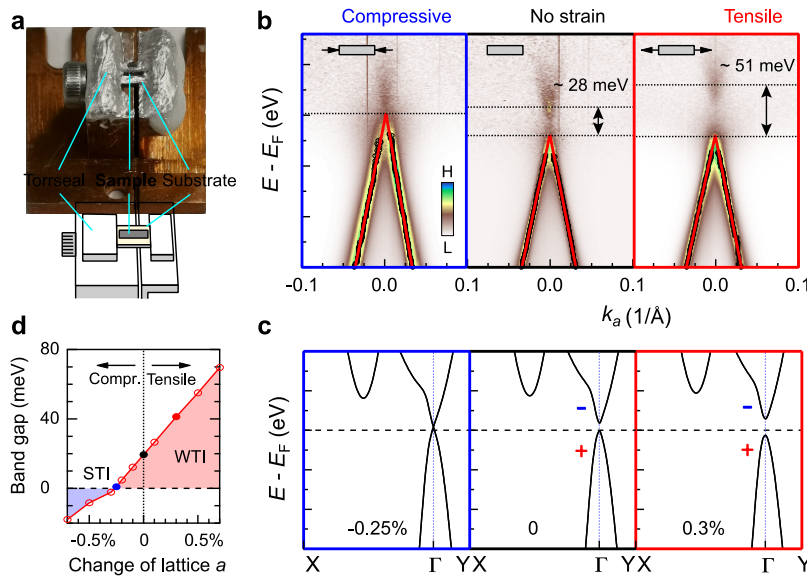


Figure 2 Strain-tuned topological phase transition in ZrTe_5 . (a) Strain device we used to apply both compressive and tensile strain. (b) Band structure measured from top surface with both compressive and tensile strain. (c) Corresponding band structures from first-principles calculations. (d) Phase diagram of ZrTe_5 with different strain.

References:

- [1] R. Noguchi et al., Nature, 566, 518 (2019).
- [2] H. Weng, X. Dai & Z. Fang, Phys. Rev. X 4, 011002 (2014).
- [3] P. Zhang et al., Nature Commun. 12, 406 (2021).

ANGLE-RESOLVED PHOTOEMISSION SPECTROSCOPY OF GALLIUM SINGLE CRYSTAL SURFACE

Koichiro Yaji¹, Kenta Kuroda², Fumio Komori²

¹Research Center for Advanced Measurement and Characterization,
National Institute for Material Science

²Institute for Solid State Physics, The University of Tokyo

Topological insulators have been intensively studied in last decade, where the spin-polarized surface states on the topological insulators can be understood with the topology of the wavefunctions of an electron. A concept common to the topological insulator is applicable to the superconductor, so-called a topological superconductor. The topological superconductor is predicted that the surface states host the emergence of Majorana bound states. Recently, we revealed that an iron-based superconductor FeSe_{0.55}Te_{0.45} is the topological superconductor [1]. Here, it is important to clarify the Fermi surface and the energy band dispersion to identify if the material is the topological superconductor.

An elemental gallium is a pure metal. The bulk gallium crystals have a rich phase diagram. Among them, only the orthorhombic phase, so-called α -gallium (α -Ga), is stable at atmospheric pressure. The α -Ga exhibits giant magnetoresistance though that is a non-magnetic material, which can be originating from topological property [2]. Moreover, the superconductivity was confirmed by both specific heat and resistivity measurements [2]. Therefore, the α -Ga would offer an interesting platform for understanding coexistence of non-trivial electronic states and superconductivity in the pure metal. In our previous study using synchrotron radiation, we have clearly observed the surface state of α -Ga. The aim of the present study is the investigation of the spin structure of the surface states with spin-resolved ARPES.

The α -Ga single crystal was prepared from super-cooled Ga [2]. Due to the low melting temperature, the special care was needed when we treated the crystal during polishing and *in situ* cleaning procedures. The α -Ga(010) surface was mechanically polished using diamond paste. Subsequently, the surface was then cleaned by repeated cycles of 0.7 keV Ne⁺ sputtering at 273 K and annealing up to 273 K in the ultra-high vacuum chamber. The clean surface was checked by low energy electron diffraction (LEED).

Figure 1 shows a LEED pattern from α -Ga(010) at 0 °C. We find sharp LEED spots, indicating that a high-quality single crystal surface has been obtained. Here, the α -Ga(010) surface has a glide plane in [100] direction. Thus, the odd-number spots in the [100] direction disappear, which is in good agreement with former study [4].

The ARPES measurements were performed at E-building in ISSP. Photoelectrons were excited by a 7-eV laser light. The sample temperature was kept at 35 K during the measurements. However, unfortunately, photoelectron intensity with 7-eV photons was not enough to observe the band of α -Ga(010) due to the low photoionization cross section.

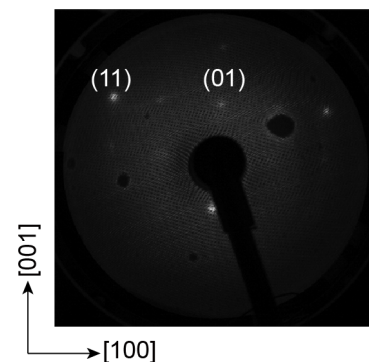


Fig. 1. LEED pattern of α -Ga(010) with the primary energy of 31 eV at 273 K.

REFERENCES

- [1] P. Zhang *et al.*, Science **360**, 182 (2018).
- [2] B. Chen *et al.*, npj Quantum Materials **3**, 40 (2018).
- [3] K. Yaji *et al.*, Rev. Sci. Instrum. **87**, 053111 (2016).
- [4] Ch. Søndergaard *et al.*, Phys. Rev. B **67**, 205105 (2003).

STUDY ON THE SPIN TEXTURE OF THE TOPOLOGICAL STATES IN QUASI-ONE-DIMENSIONAL MATERIAL

Deyang Wang¹, Mao Ye¹, Kenta Kuroda², Koichiro Yaji², Ayumi Harasawa², Takeshi Kondo²
¹*State Key Laboratory of Functional Materials for Informatics, Shanghai Institute of Microsystem and Information Technology, Chinese Academy of Science, Shanghai 200050, People's Republic of China*

²*Institute for Solid State Physics, The University of Tokyo, Kashiwa, Chiba 277-8581, Japan.*

The reducing of dimensionality in materials significantly increases electrons' anisotropy. This is especially important for topological materials, where the backscattering is prohibited due to the protection of time-reversal-symmetry. For quasi-one-dimensional (quasi-1D) materials, the occurrence of scattering is even more strictly prohibited than that in materials with higher dimensionality, because quasi-1D materials only possess one dimensional conductive channel. Therefore, the topological states in quasi-1D materials are considered to be a promising platform for the development and application of spintronics devices with low energy consumption.

TaNiTe₅ is predicted to be a candidate for quasi-1D topological materials, in which the highly anisotropic transport properties and nontrivial Berry phases have been confirmed^[1]. However, the direct experimental observation of the topological surface states in TaNiTe₅ are still missing. Thus, the band topology in this quasi-1D materials remains unclear. In this study, we unambiguously reveal the topological surface states in TaNiTe₅ by means of high resolution laser spin- and angle-resolved photoemission spectroscopy (laser-SARPES) combined with DFT calculations.

High quality single crystalline TaNiTe₅ samples were grown by self-flux method, and then characterized by the X-ray Diffraction and Energy Dispersive Spectroscopy. The high-resolution laser- SARPES experiments were conducted at the Institute for Solid State Physics, University of Tokyo, equipped with 6.994 eV photons laser and ScientaOmicron DA30L analyzer^[2]. The density functional theory (DFT) calculations were performed via *Vienna ab initio Simulation Package*^[3] for bulk bands and WannierTools^[4] for surface states.

The crystal structure of TaNiTe₅ is shown in Figure 1(a), where the NiTe₂ quasi-1D atomic chains extend along *a* direction. The Van der Waals layers stack along *b* direction, where the crystal can be easily cleaved. Figure 1(b) shows the corresponding bulk Brillouin zone (BZ) and surface projected BZ for the cleaved plane. The Fermi surface measured by laser-ARPES is shown in Figure 1(c), showing strong anisotropic properties, which shows good agreement with the calculated Fermi surface obtained by DFT method as shown in Figure 1 (d). Figure 1 (e) shows the spin-resolved band structure along $\bar{Z}-\bar{\Gamma}-\bar{Z}$ direction. Two sets of Dirac-type surface bands (denoted as α and β) near the Fermi energy, and one set of Rashba-type bands (denoted as γ) located at binding energy around 0.4 eV are clearly resolved. The spin-resolved results reveal that both α and β bands possess spin-momentum-locking spin texture, and are well reproduced by our DFT calculations [Figure 1(f)], indicating the existence of topologically non-trivial surface states.

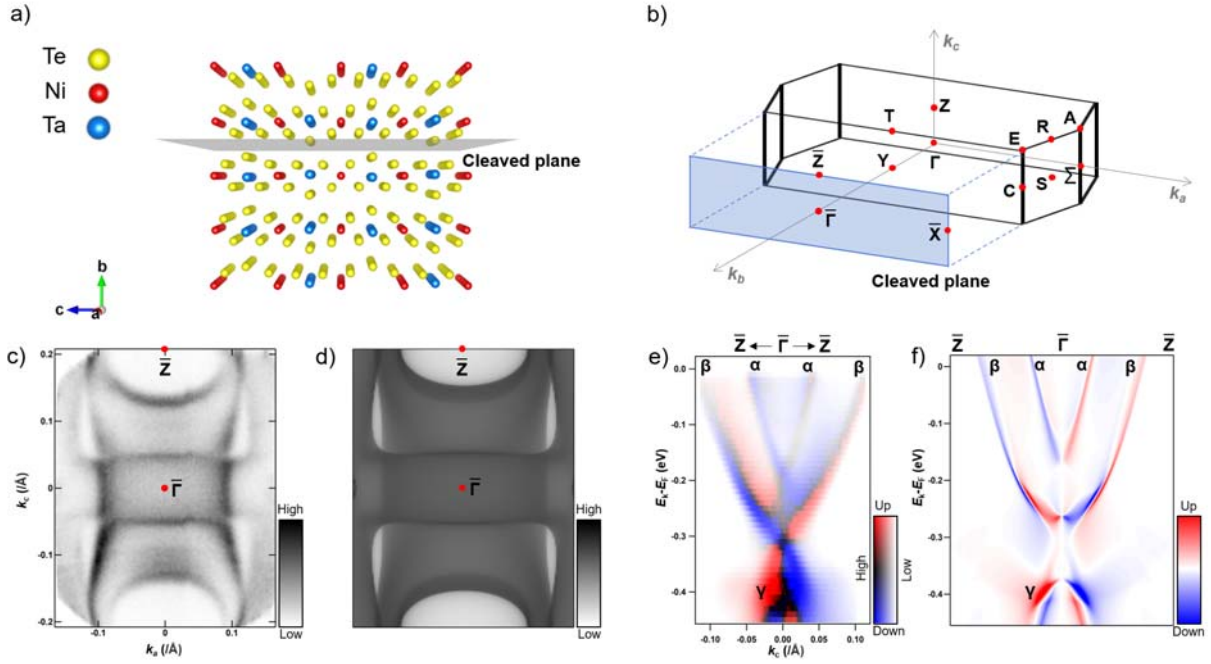


Figure 1 (a) Crystal structure and cleaved plane of TaNiTe₅. (b) Three-dimensional (3D) bulk Brillouin zone (BZ) and the projected surface BZ for cleaved plane. (c) Spin-integrated Fermi surface intensity measured by 7-eV laser-ARPES. (d) Fermi surface obtained by DFT calculations. (e) Spin-resolved band structure along $\bar{Z}-\bar{\Gamma}-\bar{Z}$ direction measured by spin-ARPES, while red and blue stands for spin-up and spin-down in k_a direction, black and white represents the intensity distribution. (f) Spin-resolved band structure along $\bar{Z}-\bar{\Gamma}-\bar{Z}$ direction obtained by DFT calculations.

In summary, we observed the surface states and its spin-texture of the quasi-1D material TaNiTe₅ through high-resolution laser-ARPES experiments, and further confirmed by the comparison with DFT calculations. Further examination of the band topology, as well as the experimental measurements on other cleaved planes would benefit the determination of the topological properties in the quasi-1D TaNiTe₅ materials.

REFERENCES

- [1] Xu, Chunqiang, et al. "Anisotropic transport and quantum oscillations in the quasi-one-dimensional TaNiTe₅: Evidence for the nontrivial band topology." *The Journal of Physical Chemistry Letters* 11.18 (2020): 7782-7789.
- [2] Yaji, Koichiro, et al. "High-resolution three-dimensional spin-and angle-resolved photoelectron spectrometer using vacuum ultraviolet laser light." *Review of Scientific Instruments* 87.5 (2016): 053111.
- [3] Kresse, Georg, and Jürgen Furthmüller. "Efficiency of ab-initio total energy calculations for metals and semiconductors using a plane-wave basis set." *Computational materials science* 6.1 (1996): 15-50.
- [4] Wu, QuanSheng, et al. "WannierTools: An open-source software package for novel topological materials." *Computer Physics Communications* 224 (2018): 405-416.

6. Staff

Director: HARADA Yoshihisa, Professor

KOMORI Fumio, Professor

MATSUDA Iwao, Associate Professor

KONDO Takeshi, Associate Professor

KIMURA Takashi, Associate Professor (2020.7~)

MIYAWAKI Jun, Research Associate (~2020.7)

KURODA Kenta, Research Associate

HORIO Masafumi, Research Associate (2020.9~)

HARASAWA Ayumi, Technical Associate

SHIBUYA Takashi, Technical Associate

KUDO Hirofumi, Technical Associate

FUKUSHIMA Akiko, Technical Associate

Technical Assistant: KOSEGAWA Yuka

ARAKI Mihoko

Secretary: AIHARA Yumiko

HARADA Misa (~2020.8)

YOSHIZAWA Motoko

TSUTSUMI Yumiko

IKEDA Kuniko

KAMEI Yuri (2020.10~)

Graduate Student: UGALINO Ralph John

SATO Yusuke

ZHAO Yuhao

YANG Tianqi

KUDO Yoshiki

SUMI Toshihide

WADA Tetsuya

KAMEDA Ayako

ZHANG Xiaoni (2020.9~)

ZHAO Haochong (2020.9~)

LI Hao (2020.9~)

Contract Researcher: OSHIMA Masaharu

AKADA Keishi (~2020.7)

YAMAZOE Kosuke

OHDAIRA Takeshi

EL Moussaoui Souliman (~2020.8)

ZHANG Wenxiong

KURAHASHI Naoya

KITAKATA Emi (2020.8~)

Harima Paper 2020

No	Title	Authors	Journal	Vol.	No.	Page	Year
1	Influence of Stacking Order of the Phthalocyanine and Fullerene Layers on the Photoexcited Carrier Dynamics in Model Organic Solar Cell	8.Kenichi Ozawa, Susumu Yamamoto, Tetsuya Miyazawa, Keita Yano, Koji Okudaira, Kazuhiko Mase, and Iwao Matsuda	J. Phys. Chem. C	accepted			2021
2	放射光オペランド計測の近未来: 軟 X 線吸収・発光分光の発展と機能材料分析	原田 慈久	精密工学会誌	87		34-38	2021
3	Band Bending of n-GaN under Ambient H ₂ O Vapor Studied by X-ray Photoelectron Spectroscopy	Yuki Imazeki, Masahiro Sato, Takahito Takeda, Masaki Kobayashi, Susumu Yamamoto, Iwao Matsuda, Jun Yoshinobu, Masakazu Sugiyama, Yoshiaki Nakano	J. Phys. Chem. C	125	17	9011–9019	2021
4	Persistence of the Topological Surface States in Bi ₂ Se ₃ against Ag Intercalation at Room Temperature	Mao Ye, Kenta Kuroda, Mikhail M. Otrokov, Anastasia G. Ryabishchenkova, Qi Jiang, Arthur Ernst, Evgueni V. Chulkov, Masashi Nakatake, Masashi Arita, Taichi Okuda, Tomohiro Matsushita, Laszlo Toth, Hiroshi Daimon, Kenya Shimada, Yoshifumi Ueda, and Akio Kimura	J. Phys. Chem. C	125	3	1784–1792	2021
5	Soft X-ray emission spectroscopy for the electronic state of water molecules influenced by plasma-treated multi-walled carbon nanotubes	Noritaka Sakakibara, Kenichi Inoue, Shion Takahashi, Taku Goto, Tsuyohito Ito, Keishi Akada, Jun Miyawaki, Yukiya Hakuta, Kazuo Terashima, Yoshihisa Harada	Phys. Chem. Chem. Phys	23		10468-10474	2021
6	Study on the Structure and Formation Mechanism of Nanoclusters in Metals by Synchrotron Radiation X-ray Spectroscopy and Spectral Simulation	Ninomiya Kakeru	Doctoral Thesis (Kyushu University)				2021
7	Femtosecond Charge Density Modulations in Photoexcited CuWO ₄	Yohei Uemura, Ahmed Ismail, Sang Han Park, Soonnam Kwon, Minseok Kim, Yasuhiro Niwa, Hiroki Wadati, Hebatalla Elnaggar, Federica Frati, Ties Haarman, Niko Höppel, Nils Huse, Yasuyuki Hirata, Yujun Zhang, Kohei Yamagami, Susumu Yamamoto, Iwao Matsuda, Tetsuo Katayama, Tadashi Togashi, Shigeki Owada, Makina Yabashi, Ufuk Halisdemir, Gertjan Koster, Toshihiko Yokoyama, Bert Weckhuysen, Frank de Groot	J. Phys. Chem. C	125	13	7329	2021
8	Valence Fluctuations in Yb(Al,Fe)B ₄ Studied by Nanosecond-time-resolved Photoemission Spectroscopy Using Synchrotron Radiation	M. Okawa, K. Akikubo, S. Yamamoto, I. Matsuda, T. Saitoh	e-Journal of Surface Science and Nanotechnology	19		20-23	2020
9	放射光軟X線分光法によるリチウムイオン電池の電子状態オペランド計測	細野 英司, 原田 慈久, 朝倉 大輔	計測と制御	60	3	207-212	2021
10	All 2D Heterostructure Tunnel Field-Effect Transistors: Impact of Band Alignment and Heterointerface Quality	Keigo Nakamura, Naoka Nagamura, Keiji Ueno, Takashi Taniguchi, Kenji Watanabe, and Kosuke Nagashio	Appl. Mater. Interfaces	12	46	51598-51606	2020
11	Micrometer-scale monolayer SnS growth by physical vapor deposition	H. Kawamoto, N. Higashitarumizu, N. Nagamura, M. Nakamura, K. Shimamura, N. Ohashi and K. Nagashio	Nanoscale,	12		23274-23281	2020
12	Localized character of charge excitations for La _{2-x} Sr _x NiO _{4+δ} revealed by oxygen K-edge resonant inelastic X-ray scattering	Kohei Yamagami, Kenji Ishii, Yasuyuki Hirata, Keisuke Ikeda, Jun Miyawaki, Yoshihisa Harada, Masanori Miyazaki, Shun Asano, Masaki Fujita, Hiroki Wadati	Phys. Rev. B	102		165145	2020
13	Time-resolved X-ray photoelectron diffraction using an angle-resolved time-of-flight electron analyzer	Artoni Kevin R. Ang, Yuichiro Fukatsu, Koji Kimura, Yuta Yamamoto, Takahiro Yonezawa, Hirokazu Nitta, Antoine Fleurence, Susumu Yamamoto, Iwao Matsuda, Yukiko Yamada-Takamura	Jpn. J. Appl. Phys.	59		100902	2020
14	New Soft X-ray Magneto-Optical Method with the Segmented Undulator and its Future Perspectives for New Light Source"	Yuya KUBOTA and Iwao MATSUDA	放射光	33	3	206-212	2020
15	Annealing Effects on Electronic States in 214-type Cuprate Superconductors by Quantum Beam Spectroscopy	Asano Shun	Doctoral Thesis (Tohoku University),				2020
16	Revisiting the Phase Diagram of T*-type La _{1-x/2} Eu _{1-x/2} Sr _x CuO ₄ Using Oxygen K-edge X-ray Absorption Spectroscopy	Shun Asano, Kenji Ishii, Kohei Yamagami, Jun Miyawaki, Yoshihisa Harada, and Masaki Fujita	J. Phys. Soc. Jpn.	89		075002	2020
17	Scanning magneto-optical Kerr effect (MOKE) measurement with element-selectivity by using a soft X-ray free electron laser and an ellipsoidal mirror	Yuya Kubota, Hiroto Motoyama, Gota Yamaguchi, Satoru Egawa, Yoko Takeo, Masaki Mizuguchi, Himanshu Sharma, Shigeki Owada, Kensuke Tono, Hidekazu Mimura, Iwao Matsuda, and Makina Yabashi	Appl. Phys. Lett.	117	4	042405	2020

E-labo. Paper 2020

No.	Title	Authors	Journal	Vol.	No.	Page	Year
1	Fully spin-polarized bulk states in ferroelectric GeTe	uraj Krempaský, Mauro Fanciulli, Laurent Nicolaï, Jan Minár, Henrieta Volfová, Ondřej Čaha, Valentine V. Volobuev, Jaime Sánchez-Barriga, Martin Gmitra, Koichiro Yaji, Kenta Kuroda, Shik Shin, Fumio Komori, Gunther Springholz, and J. Hugo Dil	Phys. Rev. Research	2		13107	2020
2	Orbital Angular Momentum Induced Spin Polarization of 2D Metallic Bands	Takahiro Kobayashi, Yoshitaka Nakata, Koichiro Yaji, Tatsuya Shishidou, Daniel Agterberg, Shunsuke Yoshizawa, Fumio Komori, Shik Shin, Michael Weinert, Takashi Uchihashi, and Kazuyuki Sakamoto	Phys. Rev. Lett.	125		176401	2020

3	Nature of the Dirac gap modulation and surface magnetic interaction in axion antiferromagnetic topological insulator MnBi ₂ Te ₄	A. M. Shikin, D. A. Estyunin, I. I. Klimovskikh, S. O. Filnov, E. F. Schwier, S. Kumar, K. Miyamoto, T. Okuda, A. Kimura, K. Kuroda, K. Yaji, S. Shin, Y. Takeda, Y. Saitoh, Z. S. Aliev, N. T. Mamedov, I. R. Amiraslanov, M. B. Babanly, M. M. Otrokov, S. V. Eremeev & E. V. Chulkov	Scientific Reports	10		13226	2020
4	Topological surface state of Bi ₂ Se ₃ modified by adsorption of organic donor molecule tetrathianaphthacene	T. Kitazawa, K. Yaji, K. Shimozaawa, H. Kondo, T. Yamanaka, H. Yaguchi, Y. Ishida, K. Kuroda, A. Harasawa, T. Iwahashi, Y. Ouchi, F. Komori, S. Shin, K. Kanai	Adv. Mater. Interfaces 7, 2000524	7		2000524	2020